

**Localization, Calibration, Control, and Design of
Magnetically Actuated Soft Capsule Endoscopes**

Submitted in partial fulfillment of the requirements for
the degree of
Doctor of Philosophy
in
Mechanical Engineering

Donghoon Son

B.S., Mechanical Engineering, Seoul National University
M.S., Mechanical Engineering, Seoul National University

Carnegie Mellon University
Pittsburgh, PA

December, 2018

© Donghoon Son, 2018
All Rights Reserved

Acknowledgments

I thank my parents, Jongrak Son and Younghee Kim, and my brother, Dongwoo Son, for their love and support. They provided me a great education and solid mental support through the years of my study.

I thank my advisor Metin Sitti for his support and advice. He introduced me to the field of magnetic robotics, gave me opportunities to develop my research skills, and provided me resources for my PhD study. I also thank my thesis committee members Carmel Majidi, Koushil Sreenath and Eric Diller for their time and intellectual guidance.

I thank Sehyuk Yim for guidance and mentorship. He taught me how to conduct research during my early stage of PhD. I would like to thank Guo Zhan Lum for giving me honest and critical advice on research. We had quite a lot of scientific discussions. Xiaoguang Dong and David Colmenares, we went through the long journey of PhD together and became supports to each other. I thank Matthew Woodward, Lindsey Hines, Sukho Song, Joshua Giltinan, Rika Wright Carlsen, Eric Diller, Zhou Ye, Jiang Zhuang, Uyiosa Abusomwan, Daiki Ito for welcoming me into CMU Nanorobotics Lab. Warm culture in our group not only encouraged me to research but also build friendship with you. The later comer in our group, Hamid Marvi, Veikko Sariola, Sueun Chung, Randall Kania, and Yizhu Gu, also joined in our group and became great support during my study.

Mehmet Berk Yigit, Muhammad Yunusa, Ville Liimatainen, and Madu Batuwangala became my close friends. We had a lot of scientific and non-scientific discussions. I would like to thank all of the previous members and current members in Physical Intelligence department at Max-Planck-Institute for Intelligent Systems. I have been happy to be in this group with brilliant and diverse minds, where I could always learn and get inspired from them. These include Amirreza Aghakhani, Yunus Alapan, Cem Balda Dayan, Abdon Pena-Francesch, Gaurav Gardi, Xinghao Hu, Alp Can Karacakolm, Ugur Kilic, Vimal Kishore, Hasan Dad Ansari Mohammad, Guillermo Amador, Varun Sridhar, Hamed Shahsavan, Anna-Maria Wild, Yan Yu, Ceren Yasa,

Oncay Yasa, Dongha Tahk, Yoonwoo Lee, Byung-Wook Park, Hyun-Gyu Kim, Hunter Gilbert, Kirstin Petersen, Hakan Ceylan, Utku Culha, Zoey Davidson, Dirk Drotlef, Kristen Kozielski, Wenqi Hu, Ajay Vikram, Morgan Stanton, Wendong Wang, Morteza Amjadi, Anuj Agrawal, Onder Erin, Chantal Goettler, Thomas Endlein, Zeinab Hosseini, Massimo Mastrangeli, Babak Mostaghaci, Alex Sprowitz, Svetlana Zakharchenko, and Ahmet Tabak. I also thank summer interns who worked with me with their passion on studies. These include Mustafa Doga Dogan, Enes Tever, Ibrahim Atespare, Mehmet Sinan Yildirim, Melike Ozkan, and Mehmet Berk Bilgin.

This thesis work has been financially supported by National Institute of Health - National Robotics Initiative (NR-014083-01), Fulbright Scholarship, CIT dean's fellowship and Max Planck Fellowship.

Abstract

Current medical technologies are converging to minimally invasive diagnosis and therapy. The effort to reduce patient discomfort in gastrointestinal (GI) tract diagnoses resulted in the development of wireless capsule endoscopes (WCEs). In the form of a pill, a camera carrying WCE travels through the GI tract by natural peristalsis while it collects images of the internal wall of the GI tract. The operation might be entirely painless. However, their inability to have active locomotion and control limit detailed diagnoses, therapeutic functions, and minimization of the operation time. Actively controlled WCEs would resolve those challenges.

This thesis provides methods for the active control of WCEs using magnetic interactions, and applies those methods to a robotic biopsy capsule endoscope. First, a localization method for meso-scale magnetic robots is developed. The method utilizes a magnetic sensor array where a magnetically actuated capsule endoscope (MACE) does not require a special device for localization but a single magnet. The method is beneficial to reduce the size and the battery consumption of the MACE. The method focuses on decoupling the magnetic field of the MACE from the magnetic field of the actuator, and developing a real-time localization algorithm. Second, an automatic calibration method for magnetic actuation and sensing systems is presented. The method calibrates a number of nonlinear magnetic sensors and a number of electromagnets. The method is capable of calibrating 1.8k parameters in an exemplary system in a reasonable time without human labor. In this work, Bundle Adjustment framework from Computer Vision is modified and adapted to magnetic robot sensing and actuation systems. This work would be useful for a magnetic system which requires frequent reconfiguration or sensor/actuator gain updates. Third, control methods for a meso-scale magnetic robots on a surface with non-uniform magnetic field actuations are presented. The control methods utilize magnetic energy wells to cope with a low actuation bandwidth compared to the fast dynamics of the capsule endoscope. Additionally, we present a teleoperation system to mitigate the orientation coordination difficulty when a person uses the system. Fourth, all of the above three

methods are integrated and applied to a magnetically actuated soft capsule endoscope for the biopsy functionality (B-MASCE). We designed a biopsy capsule endoscope with a high diagnostic accuracy by adopting a clinically well established biopsy method called fine-needle capillary biopsy. *Ex vivo* experiments in a fresh porcine stomach show promising results. In summary, this thesis presents localization, calibration, control methods and their application in a biopsy capsule robot, which are useful for the automation of robotic capsule endoscopes. We envision that, in future, patients have painless GI tract endoscopy and treatment with highly functional robotic endoscopic capsules.

Contents

Acknowledgments	iii
Abstract	v
List of Tables	x
List of Figures	xi
Nomenclature	xiii
1 Introduction	1
1.1 Motivation	1
1.2 Related Studies	4
1.2.1 Medical Background for WCEs	4
1.2.2 Internally Actuated Capsule Endoscopes	5
1.2.3 Magnetically Actuated Capsule Endoscopes (MACEs)	7
1.3 Research Objectives	10
1.4 Thesis Organization	11
2 5-D Localization Method for a Magnetic Robot	13
2.1 Introduction	13
2.2 5-D Localization Method	18

2.2.1	Setup	18
2.2.2	Working Principle	18
2.2.3	Algorithm	24
2.3	Experiments	27
2.4	Discussion	32
2.5	Summary	37
3	A Simultaneous Calibration Method for Magnetic Robot Localization and Actuation Systems	39
3.1	Introduction	39
3.2	Simultaneous Calibration Method	43
3.2.1	System Description	43
3.2.2	Framework: Calibration as Bundle Adjustment	44
3.2.3	Parametrization	45
3.2.4	Calibration Model	47
3.2.5	Formulation of a Cost Function	50
3.2.6	Choosing a Numerical Solver	54
3.3	Simulation Results	54
3.4	Experimental Results	56
3.4.1	Experimental Setup and Procedure	56
3.4.2	Magnetic Sensor System Calibration Result	57
3.4.3	Actuation System Calibration Result	58
3.5	Discussion	60
3.5.1	Actuator Model's Complexity and Accuracy	60
3.5.2	Placement of the Sensor Array	61
3.5.3	Applications of the Method	63
3.5.4	Limitations	63

3.6	Conclusion and Future Work	64
4	Control of Magnetically Actuated Soft Capsule Endoscope	65
4.1	Introduction	65
4.2	Magnetic Actuation Background	66
4.2.1	Magnetic Field Models	66
4.2.2	System Dynamics	70
4.2.3	Local Coordinate Definition	71
4.3	Controls	73
4.3.1	Orientation Control and Rolling Locomotion	73
4.3.2	Anchored Orientation Control	77
4.3.3	Collapsing controller	78
4.4	Teleoperation	79
4.5	Conclusion	79
5	Application: Magnetically Actuated Soft Capsule Endoscope for Fine Needle Biopsy	81
5.1	Introduction	81
5.2	Application Scenario	83
5.2.1	Fine-Needle Biopsy Techniques	83
5.2.2	FNCB application on MASCE: B-MASCE	84
5.3	Design of B-MASCE	87
5.3.1	Design Features	87
5.3.2	Design Parameters	89
5.3.3	Fabrication	91
5.4	<i>Ex vivo</i> Experiments	92
5.5	Discussion	97
5.6	Conclusion	100

6	Summary	102
6.1	Thesis Contributions	102
6.2	Challenges and Future works	103
6.2.1	Size Minimization	103
6.2.2	Reconfigurable Actuation System	103
6.2.3	Visual Coordination and Registration	104
6.2.4	Multiple MASCE Control	104
6.2.5	In Vivo Experiments	105
A	Design, Fabrication, and Calibration of the Omni-directional Electromagnet	107
B	Design and Fabrication of the Nine-Coil Actuation System	112
C	Design and Fabrication of the Magnetic Sensor Array	117
D	Mechanical Drawing of B-MASCE	121
E	MatLab Codes for the Localization Method	123
F	MabLAB Codes for the Calibration Method	126
G	MabLAB Codes for the Control Methods	133
	Bibliography	143

List of Tables

2.1	Specification of the Localization Setup	20
2.2	Dynamic Motion Tracking Experiment Results	31
2.3	Comparison of Existing Magnetic Localization Methods with the Proposed Method	34
3.1	Parametrization	45
3.2	Specification of the Localization and Actuation Setup	56
3.3	Initial Parameters and Tolerances	57
5.1	Design Parameters	87
A.1	Specification of the Omnidirectional Electromagnet	108
B.1	Specification of the electromagnet	114
B.2	Actuation System Design Parameters	116

List of Figures

1.1	State of Art Wireless capsule endoscopes	3
1.2	Internally Actuated Capsule Endoscopes using different locomotions	6
1.3	Magnetically actuated capsule endoscopes (MACEs) using different locomotions	9
1.4	Two different magnetic actuation systems	10
2.1	Photographs of the five-dimensional magnetic localization setup.	16
2.2	Overall signal flow of the system. Measured sensory data from Hall-effect sensor array and current sensors are fed to the computer through the DAQ board.	17
2.3	Schematic drawing of the application scenario.	19
2.4	Experimental comparison of $SQR_{z,B}$ and $SQR_{z,L}$	25
2.5	Block diagram of the main localization algorithm.	27
2.6	Experimental setup and the dynamic motion of the MACE	29
2.7	Result of the dynamic motion tracking experiment (the worst case)	31
2.8	Simulated effective localization range (S_{eff}) as a function of the inherent sensor noise	33
2.9	Simulated effective localization range (S_{eff}) as a function of the size of a magnetic robot	38
3.1	Experimental setup of the proposed magnetic localization and actuation system	41
3.2	Geometric parameters of the sensor and actuation systems	46
3.3	Simulation results	55

3.4	Experimental calibration results	59
3.5	Comparison of model fitting accuracy using different actuation models	62
4.1	Simulated energy distributions for different controlled motions	67
4.2	System dynamics and a local coordinate definition	71
4.3	Teleoperation of the capsule robot	80
5.1	Prototype of B-MASCE	85
5.2	Application scenario	86
5.3	CAD model of B-MASCE	88
5.4	Restoration force estimation	91
5.5	<i>Ex vivo</i> model preparation	93
5.6	<i>Ex vivo</i> demonstration of B-MASCE	95
5.7	Fluorescent microscope images of the extracted biopsy samples	96
5.8	Active imaging test of B-MASCE	98
A.1	Omnidirectional eletromagnet fabrication	109
A.2	Omnidirectional eletromagnet calibration	110
B.1	Nine-coil system	113
C.1	Schematic drawing of the sensor array	119
C.2	Fabricated sensor arrays	120
D.1	Mechanical drawing of B-MASCE	122

Nomenclature

\mathbb{S}^2	2-sphere manifold
A	Ampere
\mathbf{w}	Angular velocity
BA	Bundle adjustment
G	cgs unit of magnetic flux density or magnetization, Gauss
R^2 values	Coefficient of determination
$\{\cdot\}$	Coordinate
\times	Cross product
dB	Decibel
dof	Degree(s) of freedom
\mathbb{J}	Electric current matrix in a stacked matrix form
I	Electric current reading
\mathbf{i}	Electric currents in coils
\preceq	Element-wise inequality
g	Gain value of the sensors in a specification sheet
$g(\cdot)$	Gauge freedom constraint function
∇	Gradient

g	Gravitational acceleration
H	Hessian matrix
I	Identity matrix
i, j, k	Index variables
\cdot	Inner product
u	Input command
IPA	Interior-point algorithm
b	Magnetic field vector
f	Magnetic force
m	Magnetic moment vector
M	Magnetic moments mapping in a diagonal matrix form
$E_{p,m}$	Magnetic scalar potential energy of a magnetic dipole
p_s	Magnetic sensor parameters
v	Magnetic sensor reading
τ	Magnetic torque
B	Mangetic dipole mapping matrix with only position components
$S\mathbb{R}^{n \times n}$	$n \times n$ symmetric matrix
NeFeB	Neodymium iron boron
h	Nodal distance between magnetic sensors
G	Non-orthogonal sensitivity matrix with rotation
1-D	One-dimensional
\hat{n}	Orientation unit vector
\otimes	Outer product

μ_0	Permeability of free space
ζ	Pose difference in axis-angle representation
\mathbf{r}	Position vector
H	Quadratic sensitivity matrix
\mathbb{R}	Real coordinate space
\mathbb{V}	Recovered B-field in a stacked matrix form
\mathbf{R}	Rotation matrix
A/m	SI unit of magnetic field strength or magnetization
T	SI unit of magnetic flux density, Tesla
A·m ²	SI unit of strength of a magnetic dipole
SQR	Signal quality ratio
SNR	Signal to noise ratio
SLAM	Simultaneous localization and mapping
STD	Standard deviation
SfM	Structure from Motion
\sum	Summation operator
∇^2	The Laplace operator
M	The number of actuators
N	The number of measurements
N	The number of sensors
3-D	Three-dimensional
TFE	Transverse field effect
2-D	Two-dimensional

H	Unit of inductance, Henry
K	z -directional derivative

Chapter 1

Introduction

1.1 Motivation

Through the last two centuries, endoscopic technology has improved dramatically [1]. From the original device, *Lichtleiter*, from Philipp Bozzini in 1806 to the current flexible endoscopes, the technological advances have not only made the diagnosis accurate, but also made the procedure less painful to patients. The imaging became more accurate using small cameras rather than using mirrors to reflect images. The endoscopic tube became more flexible using advanced materials rather than a thick metal tube. Modern endoscopes are equipped with advanced diagnostic and therapeutic tools, such as forceps or cauterization devices. Recent advances in the camera technology made even high definition (HD) image quality endoscopy combined with other imaging modalities, such as fluoroscopy or ultrasound imaging. However, in spite of the advances in the endoscopic device technology, it still causes significant discomfort and pain to patients. Often patients are put under anesthesia to avoid feeling the pain and trauma. For example, to avoid those shortcomings in colonoscopy, other diagnostic methods, such as guaiac faecal occult blood testing (gFOBT), immunohistochemical faecal occult blood testing (iFOBT), computed tomographic colonoscopy (CTC), colon capsule endoscopy (CCE), flexible sigmoidoscopy (FS), and double-contrast barium enema (DCBE), are proposed and compared

as alternatives [2].

The research effort to minimize the discomfort and pain created a new technology, Wireless Capsule Endoscopes (WCEs) [3]. In 2001, Israeli medical company, *Given Imaging Ltd.*¹, announced the development of the WCE, and had an approval from Food and Drug Administration (FDA), U.S. WCEs had not only minimized the pain from the endoscopy, but also allowed us to take a visual endoscopy of a small bowel, which was very challenging with flexible endoscopes. After the original Pillcam was introduced, Pillcam got further developed in series with for various target organs or performance improvements (Fig. 1.1(a-d)). Other medical companies also have developed different versions of WCEs which made the WCE technology matured (Fig. 1.1(e-h)). Currently, the WCEs even became a standard procedure for specific small bowel diseases, such as Crohn's disease [4]. Further development in imaging technologies, such as narrow band imaging (NBI) by Olympus, enhanced visual diagnostic quality for the latest WCEs.

However, the WCEs have a functional limitation: Lack of mobility. The most of current commercialized WCEs are not controllable directly from a doctor because WCEs are passively actuated by peristalses from GI tract. This fundamental limitation casts two possible drawbacks. First, suspicious lesions could not be thoroughly examined under a doctor's detailed control as like the flexible endoscopy. Second, advanced functions from the flexible endoscopes, such as biopsy or cauterization, are not available in WCEs. This motivation triggered a new research area, active capsule endoscopes. Study on active capsule endoscopes has been conducted progressively through the last decade [5]. This not only enabled the controlled locomotion of the capsule, but also facilitated the basic therapeutic procedures, such as biopsy or drug delivery using capsule robots. The development of active capsule endoscopes allows us to have a detailed diagnosis and therapeutic procedures. With the development of active capsule endoscopes, a patient would have detailed diagnoses and therapeutic operations with less pain and discomfort in near future.

¹Currently the company is owned by Medtronic plc.

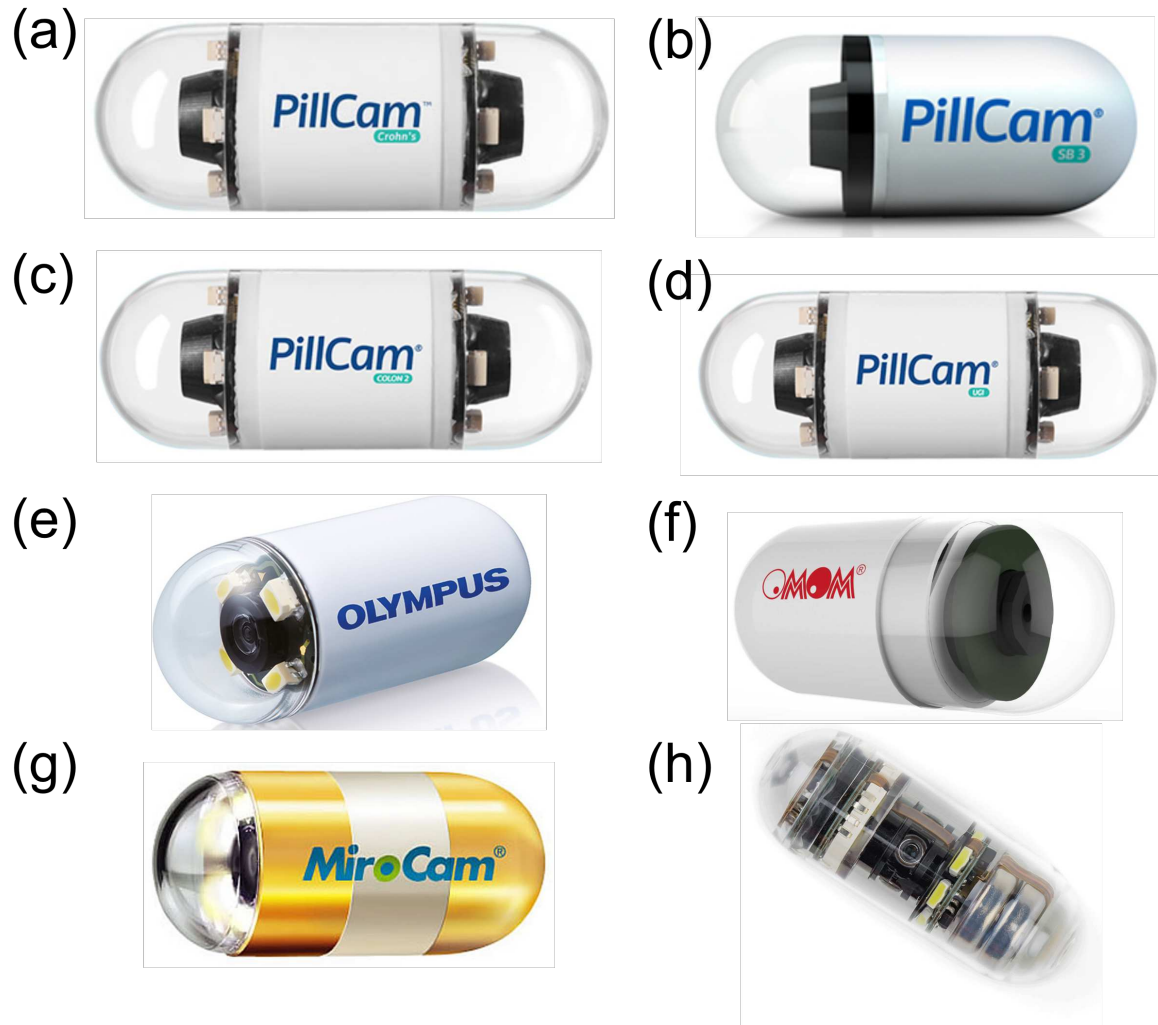


Figure 1.1: State-of-art wireless capsule endoscopes (WCEs). (a) PillCam™ Crohn's (Medtronic plc.) (b) PillCam™ SB3 (Medtronic plc.) (c) PillCam™ COLON2 (Medtronic plc.) (d) PillCam™ UGI (Medtronic plc.) (e) Endocapsule (Olympus Group) (f) OMOM Capsule (Chongqing Jinshan Science & Technology) (g) MiroCam® (Intromedic Co., Ltd.) (h) CapsoCam® Plus (Capsovision Inc.)

1.2 Related Studies

1.2.1 Medical Background for WCEs

WCEs are used to examine GI-tracts. Because WCEs can reach small intestines easily, the WCEs are mostly used in clinics to diagnose small bowel diseases, such as obscure gastrointestinal bleeding, Crohn's disease, celiac disease, hereditary polyposis syndromes, and small bowel tumors [6]. Capsule endoscopy (CE) is an easy procedure. Compared to the traditional colonoscopy and esophagogastroduodenoscopy (EGD), the procedure is almost painless, therefore, sedation or anesthesia is not required. Even during the procedure, a patient can leave the hospital and go about his/her day. Before the CE, the patient is required have an overnight fast for clear images of the GI tract. Before the procedure, small patches are attached to the abdomen of the patient. These small patches are with radio frequency (RF) antennas for the communication with an image recording device, which needs to be attached on the patient's belt. After this preparation, the patient swallows a WCE with a cup of water. The patient can drink water after 2 hours, and have a light lunch after 4 hours [7]. Once the WCE is activated, it continuously takes an image and sends it to the recording device. The activation point of the device might differ by the targeted tract. Currently, typical targeted areas are the duodenum, small bowel, and colon. The WCE travels the GI-tract like a pill. Once it is swallowed, the patient should not feel it. While the WCE travels the GI-tract, images of the GI-tract is taken and sent to the recording device. Usual time for the small bowel endoscopy is 8-12 hours, but it might differ from one person to another. The endoscopy is complete after the 8-12 hours and the patient would see the WCE in the toilet after a bowel movement. The WCE would be disposed. After the endoscopy is complete, the patient can remove the patches and the recording device, which would be returned to the hospital for the video examination [8]. An endoscopist will examine the video images to determine whether the patient needs further treatments. The reading time of the images of an endoscopist is 45-120 min [9]. The capsule retention in a body

is a main risk of the CE. In a retrospective study with 1000 CE procedures, 1.4% of the patients had capsule retentions. To prevent the capsule retention in a body, it is recommended to have a radiological examination of the targeted area to check if there is a passage which can cause the capsule retention. Once the capsule retention occurs, it requires an endoscopic or a surgical treatment to remove it [10].

Limitations of WCEs come from the passiveness of the device. A WCE is designed to travel the GI tract by peristalses, thus it does not have any means of actuation. Thus, the major drawback is the operator's inability to control its locomotion. This excludes revisualization of a suspicious lesion, which could enhance the visual diagnostic accuracy. Especially, a region where the WCE travels fast, such as duodenum or proximal jejunum, the rate of missed lesions is high [11]. Also, WCEs cannot perform flushing, suctioning, or air insufflation for better images. In addition, WCEs do not take a biopsy, which is a critical procedure to confirm a disease. If a suspicious lesion is found during CE, then additional biopsy procedure is required afterwards.

1.2.2 Internally Actuated Capsule Endoscopes

The active robotic capsule endoscopes would fall into one of two categories by means of actuation. In the first category, the WCEs are internally actuated, which would be discussed in this section. Those capsules use batteries or tethers to power the robots. In the other category, WCEs are externally actuated, and most of them are magnetically actuated, which would be discussed in the next section. In the case of the internally actuated capsule endoscopes, an actuation strategy of a robotic capsule endoscope strongly depends on the targeted GI-tract region. A one-dimensional (1-D) GI-tract, such as esophagus, small intestine, or large intestine, is tubular. Those GI-tracts do not require complex orientation manipulation of the robotic capsule endoscopes as the motion of the robot is restricted in 1-D motion. Rather, many studies have focused on forward movement mechanisms, which can overcome the peristalsis of the GI-tracts.

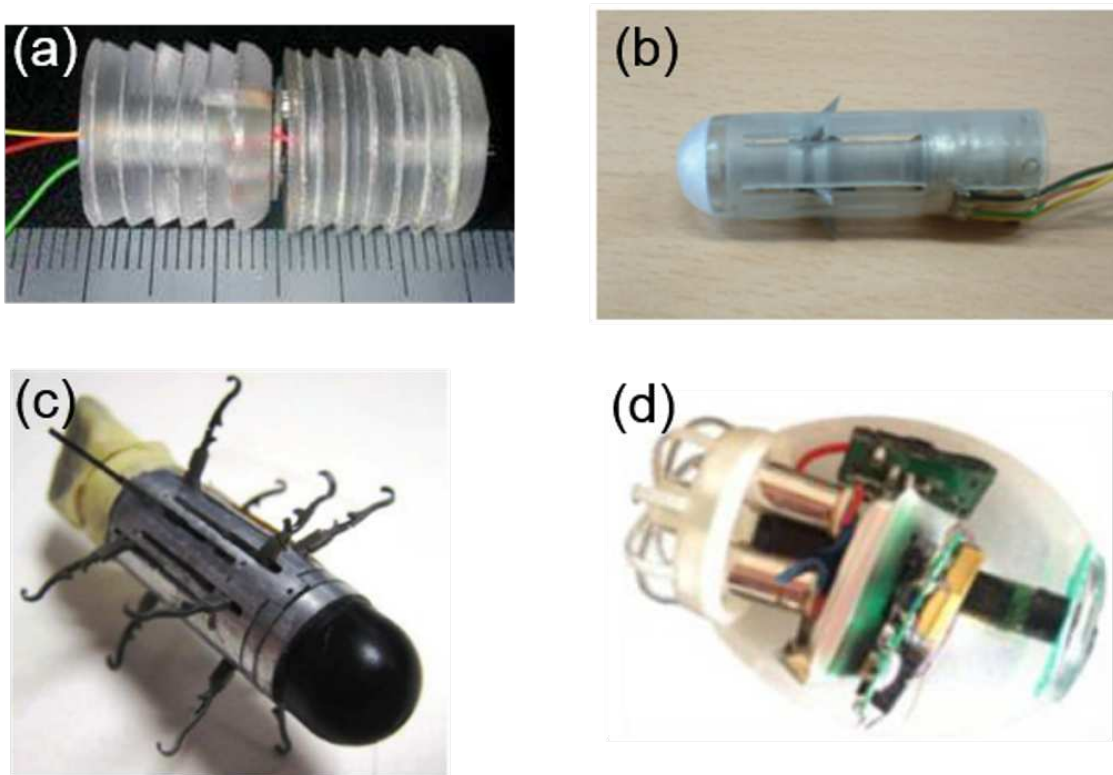


Figure 1.2: Internally Actuated Capsule Endoscopes using different locomotions. (a) Inch-worm locomotion [12]. (b) Paddling based locomotion [16]. (c) Sequential leg locomotion [13]. (d) Submarine-like locomotion [20].

Kim *et al.* developed a crawling mechanism for a capsule endoscope using shape memory alloy (SMA) [12]. Quirini *et al.* designed a robotic capsule endoscope with twelve legs, which can move forward by folding and deploying legs sequentially [13, 14, 15]. Park *et al.* proposed a robotic capsule endoscope that has paddling based locomotion, and showed successful *in-vivo* experiment results [16]. Many various robotic capsules were proposed using inchworm motions [17] [18] [19] as well.

The locomotion of the capsule in a stomach is different than in the 1-D GI-tract because of the geometry of the stomach. A stomach is a large cavity and present a large surface to be examined, whereas it does not give direct peristalsis to the robot. This is a challenge to the robots because the robot cannot examine all surfaces of the stomach without an active orien-

tation control and locomotion. To navigate freely in 3-D space of the stomach, Tortora *et al.* showed a robotic capsule endoscope that navigates inside the water-filled stomach using fluidic interactions like a sub-marine [21], and Falco *et al.* showed an advanced version of this capsule with an embedded camera [20]. The robot uses four propellers to move and orient inside a water-filled stomach. The robot demonstrated active navigations in an *ex-vivo* porcine stomach.

Main challenges of the internally actuated capsule endoscopes are limited by power sources and spaces to embed complex actuation mechanisms. Because the robot needs to be small enough to be swallowed, it is difficult to embed the actuating systems inside the capsule all together. The space for the actuation mechanism competes with the space for the battery, which might lead to a short operation time. These technical challenges make the magnetically actuated capsule endoscopes more attractive, because the remote actuation by the magnetism does not require additional device or energy consumption inside the capsule robot other than a single magnet.

1.2.3 Magnetically Actuated Capsule Endoscopes (MACEs)

Magnetically actuated capsule endoscopes (MACEs) provide a promising medical technology for minimally invasive diagnosis on gastrointestinal organs [22, 23, 24, 25, 26, 27, 28, 29]. Far ranging magnetic field can precisely actuate a targeted magnet without using any internal power source. A permanent magnet inside the capsule naturally works as an internal actuation source for the robot. This makes the robot to save energy and space for the actuation, which allows us to embed a large capacity battery for the wireless communication, and the other required tasks. Thanks to the precise control of the magnet, MACEs can be used not only for the 1-D GI tracts, but also for the stomach endoscopy.

Hong *et al.* showed the feasibility of a MACE in a pig's esophagus, a stomach and a large intestine using a multi degrees of freedom (dof) robotic manipulator [30]. Carpi *et al.* conducted animal experiments using a commercial permanent magnet-based actuation system (Niobe,

Stereotaxis, Inc, USA), which is mainly used for magnetic navigations of cardio-vascular active catheters (Fig. 1.3a) [31]. Further, Keller *et al.* used a hand-held external permanent magnet to maneuver PillcamTMColon capsule inside human subject abdomens. Simi *et al.* showed paddling locomotion assisted with magnetic gradient pulling (Fig. 1.3b) [32]. In our previous study, we proposed a new multi-functional endoscopic capsule robot (Fig. 1.3d) [33, 34, 35, 36]. Ciuti *et al.* showed MACE controls by an external permanent magnet attached to an end-effector of a six-dof robotic arm [37, 38, 39]. Further, using a robotic arm with a permanent magnet, Mahoney *et al.* demonstrated spiral locomotion of the robot in the air (Fig. 1.3c) [26] and demonstrated a precise levitation control of a neutrally buoyant MACE in water (Fig. 1.3e) [26]. Olympus Inc. and Siemens AG co. developed a novel MACE manipulation platform which controls the MACE in five-dof in a water-filled stomach. A blind study with this system and conventional gastroendoscopy yielded comparable results [40]. Petrusuka *et al.* introduced an electromagnet system for a MACE with a direct and rapid magnetic field control without moving any parts of the setup [41], and demonstrated a stable levitation control of a neutrally buoyant MACE in water using multiple omnidirectional electromagnets (OmniMag) (Fig. 1.3e) [42]. A Chinese company, Ankon co., has shown the levitation control of a MACE and clinical tests, and got an approval from Chinese Food and Drug Administrations in 2013. A MACE from Ankon, NaviCamTM, has been exported internationally since 2017.

The magnetic actuation methods could be categorized into two groups: permanent magnet based actuation systems and electromagnet based actuation systems (Fig. 1.4). Although a permanent magnetic system could provide a strong magnetic field than an electromagnetic system with less energy consumption, the safety is the major concern in medical environments. The electromagnetic based actuation is safer than the permanent magnet based actuation in two reasons. First, the electromagnet could be turned off immediately, whereas it is very hard to turn the permanent magnet off. If a MACE is accidentally attracted to the magnetic source, then the robot might exert very strong force towards the external magnet. Secondly, the robotic system for the permanent magnet has a potential risk to hit the other object or a person nearby. In clinic,

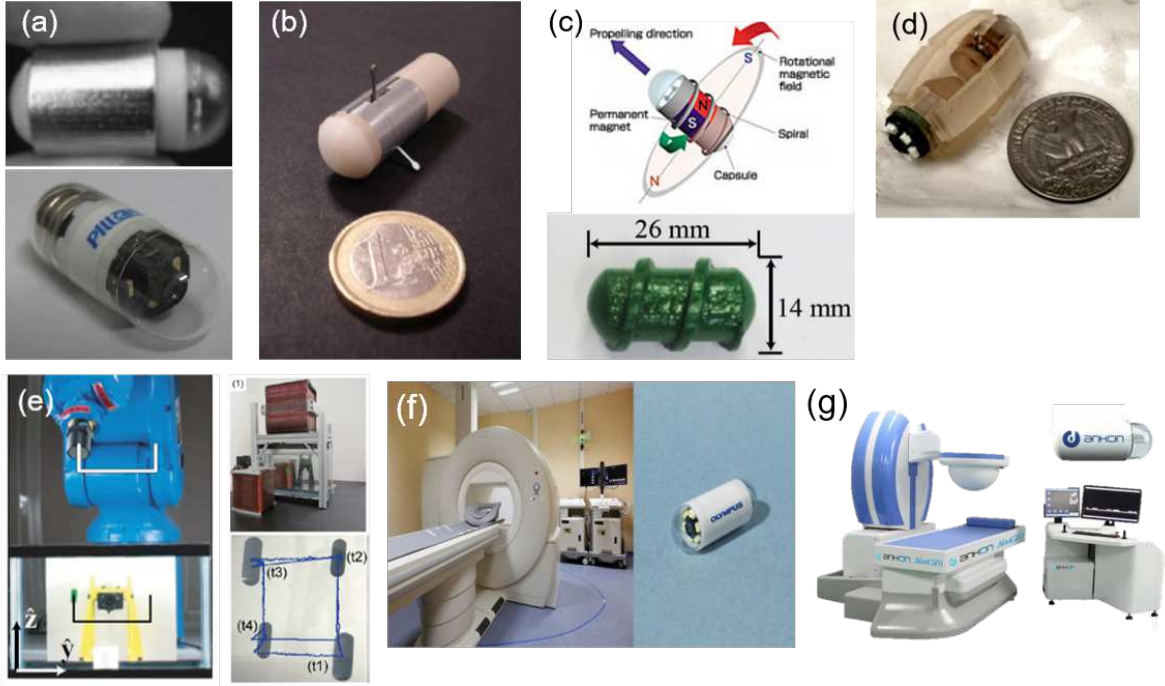


Figure 1.3: Magnetically actuated capsule endoscopes (MACEs) using different locomotions. (a) Magnetic gradient pulling based locomotion (top: Carpi *et al.* [31], bottom: Swain *et al.* [43]). (b) Hybrid locomotion of magnetic gradient pulling with paddling legs driven by an internal motor (Simi *et al.* [32]). (c) Spiral locomotion using a rotating magnetic field (orientation is not controlled) (top: Olympus co., bottom: Mahoney *et al.* [44]). (d) Rolling locomotion using a rotating magnetic field (orientation is controlled) (Yim *et al.* [33]). (e) Levitation control using neutrally buoyant MACEs. (Left) Levitation control with a robotic arm [26] (Right) Levitation control with Omnimagnets [42]. (f) Siemens AG magnetic endoscopy platform (left) with a magnetic Olympus endoscopic capsule (right) [40]. The capsule is controlled in five dof using the actuation system. (g) NaviCam™ from Ankon.

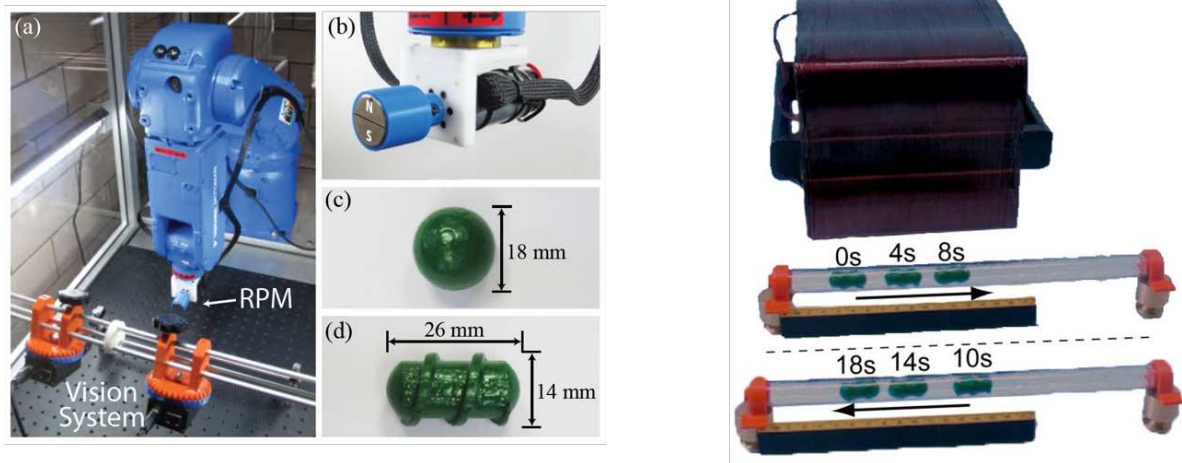


Figure 1.4: Two different magnetic actuation systems. (Left) Permanent magnetic actuation system is shown. Permanent magnetic system uses a robotic arm for the precise position and orientation control of the MACE [44]. (Right) Electromagnetic actuation system. An electromagnet can remotely control the magnetic field directly in a fixed position [41].

it would require challenging planning procedure to avoid the collision.

1.3 Research Objectives

The goal of this thesis is to improve diagnostic yield of an active capsule endoscope. To achieve that goal, manipulation methods using remote actuation must be improved. Because the manipulation is based on the localization information and control accuracy, development of the localization and control technique become basic requirements. Calibration of the manipulation system would improve the localization and control, which would lead to the improvement of the manipulation as well. On the other hand, the robot's design plays a significant role to improve the diagnostic accuracy, therefore, the design improvement must be taken into account. We choose magnetically actuated capsule endoscopes (MACEs) as our main research platform because it has advantages over the other types of active robotic capsules as we have discussed in the previous section. Specifically, we employ magnetically actuated soft capsule endoscopes (MASCEs) because of its potential usage in the advanced therapeutic functions [33, 34, 35, 36, 45]. For actuating MACEs or MASCEs, we choose electromagnetic actuation system in this

thesis due to the safety concern.

Specifically, we define tangible goals for improving MASCEs diagnostic performance using electromagnetic actuations. We believe that the final goal of the research on MASCEs would be a fully automated system that can perform a visual endoscopy and therapeutic functions under a supervision of a doctor. To move towards that goal, we start with basic automation techniques. This direction is described as:

- Improve the manipulation of the MASCE by developing automation techniques, such as localization, calibration, and control methods for meso-scale magnetic robots
- Integrate the robotic system and algorithms, and test in a realistic environment
- Improve the diagnostic accuracy with an improvement in the design of a MASCE

1.4 Thesis Organization

This thesis starts with magnetic localization method in Chapter 2. As the magnetic localization has a magnetic coupling of the actuating magnetic field, we resolve this problem and improve the quality of the localization. In Chapter 3, we present an automatic calibration method for the magnetic actuation and sensing systems. This is a very important task, as it involves about building the actuation and sensing model. Those models affect the localization and control quality directly. The systems for magnetic localization and actuation involve a huge number of the calibration parameters (1.8K parameters in the system used in this thesis), which makes the problem impossible to be solved manually. Computer visions already have dealt with a similar problem called Structure from Motion (SfM), and we adapt this framework into our magnetic settings. In Chapter 4, we present control methods for the MACE. The controlled motion includes an orientation control, position-anchored orientation control, and collapse control (in the case of MASCE). In these control methods, we utilize magnetic energy wells to achieve stable semi-open-loop controllers. Additionally, we propose a tele-operation system to mitigate

an orientation coordination difficulty for a user of the system. In Chapter 5, we present a novel design of a biopsy MASCE using a fine-needle biopsy technique. The fine-needle biopsy technique is employed to improve the diagnostic accuracy of submucosal tumors where the needle can penetrate into the deep tissue of a lesion. The methods proposed in the previous chapters are integrated and tested in *ex-vivo* experiments. In Chapter 6, we summarize the thesis and describe future works.

Chapter 2

5-D Localization Method for a Magnetic Robot

2.1 Introduction

Localization of MACEs is crucial for the examination of a GI-tract. First, the localization information serves as a tracking purpose. When a doctor examines the GI-tract, he or she should know where the inflammation happened and to mark the place for further treatment. Second, the localization information serves as a prior information for controlling MACEs. If the localization is not correct, then the estimated force and torque on the robot would not be accurate. This would lead to a poor control of a MACE, where the doctor might not be able control the camera angle to where the place to be examined.

One general localization method for magnetic capsules is to detect the magnetic field from a small permanent magnet inside the capsule using an external magnetic sensor array [46, 47, 48, 49]. However, these methods are not applicable to MACEs because the strong magnetic field from the magnetic actuation system interferes with sensor array(s), which results in decreased accuracy or failure. Recently, Hashi *et al.* proposed the idea of superimposing high frequency alternating magnetic field on a low frequency manipulating magnetic field. This

magnetic localization method is compatible with the external magnetic field, and shows sub-millimeter position accuracy. However, it is limited to three-dimensional (3-D) localization, and cannot determine the capsule's orientation [50, 51, 52].

A different strategy for localization is to use the onboard magnetic sensor(s) to calculate relative position and orientation to the external magnetic field source. By using onboard sensors, the magnetic field from the MACE's magnet is considered as a DC offset, which can be easily calibrated. Kim *et al.* proposed a localization method utilizing a rotating external magnetic field with onboard magnetic sensors, which gave 15 mm position error and 15° orientation error [53]. Similarly, Popek *et al.* utilized a rotating magnetic field with 11 mm position error and 11° orientation error by using onboard magnetic sensors [54]. However, these methods are only applicable for a rotating external magnetic field, which limits locomotion of the MACE to only rotation. Natali *et al.* introduced a localization method which compares the measured sensory data with pre-calculated data of the external magnetic field. The method requires multiple magnetic sensors and an inertial sensor inside the system. Their method gave 3.4 ± 3.2 mm position error and $19 \pm 50^\circ$ angular error within a 15 cm radius workspace [55]. However, the angular accuracy is not sufficient for disease diagnosis.

Previously, we proposed a 3-D localization method using an internal sensor [56], which consists of three steps: the coaxial alignment stage between the MACE and the external magnet, the MACE deformation stage, and the MACE shape recovery stage. The proposed method showed 2.1 mm resulting position error in the experiment. However, the coaxial alignment stage required careful adjusting of the external magnet. Even a small direction error could induce a large localization error as the MACE moves farther from the external magnet. Furthermore, this method required specific external magnet motion at a given time different than the capsule locomotion, which could not enable continuous real-time MACE localization. For continuous real-time localization, a different working principle is required.

Besides magnetic localization methods, other localization modalities, such as radio frequency (RF) based detection and inertial sensing, could be considered. However, RF based

localization and inertial sensing both take space inside the capsule. Additionally, RF methods consumes energy due to the significant signal attenuation through the human organs and skin. Also those methods do not give accurate localization accuracy in the current development stage [27]. On the other hand, imaging methods based on ionizing radiations, such as fluoroscopy using X-ray, risk patients getting the radiations. Magnetic resonance imaging (MRI) based tracking is slow (27 ms) and it limits the magnetic actuation only providing the force actuation on a magnetic bead [57].

Even though most of the methods utilize the on-board magnetic sensor system, employing an external sensor system has considerable benefits. If an external sensor system is used, the number of electrical components inside the MACE is reduced. Thus, its volume and energy consumption is minimized. Furthermore, the external sensor system allows us to utilize the abundant amount of sensors without much spatial and energy restriction, which leads to better accuracy with the increased number of the sensors than the onboard sensory system.

This chapter introduces a new real-time 5-D localization method for a MACE using an external Hall-effect sensor array and an external omnidirectional electromagnet [41]. The key point of the developed 5-D localization method is to separate the MACE's magnetic field from the actuator's magnetic field. By subtracting the electromagnet's field from the measured data, we can obtain the pure magnetic field of the MACE within the coupled magnetic field. Additionally, the error is reduced with a second order directional differentiation by taking the advantage of the Laplacian of the magnetic field. Note that a low pass filter was applied to the magnetic field before the differentiation to prevent a significant noise increase. The proposed method is compatible with any magnetic capsule robots or magnetic micro-robots which are actuated by an external magnetic field.

This chapter is organized as follows. Section 2.2 introduces the localization setup, the working principle, and the algorithms. In Section 2.3, the proposed method is verified in experiments. Section 2.4 discusses the effect of the inherent sensor noise on the accuracy of the method.

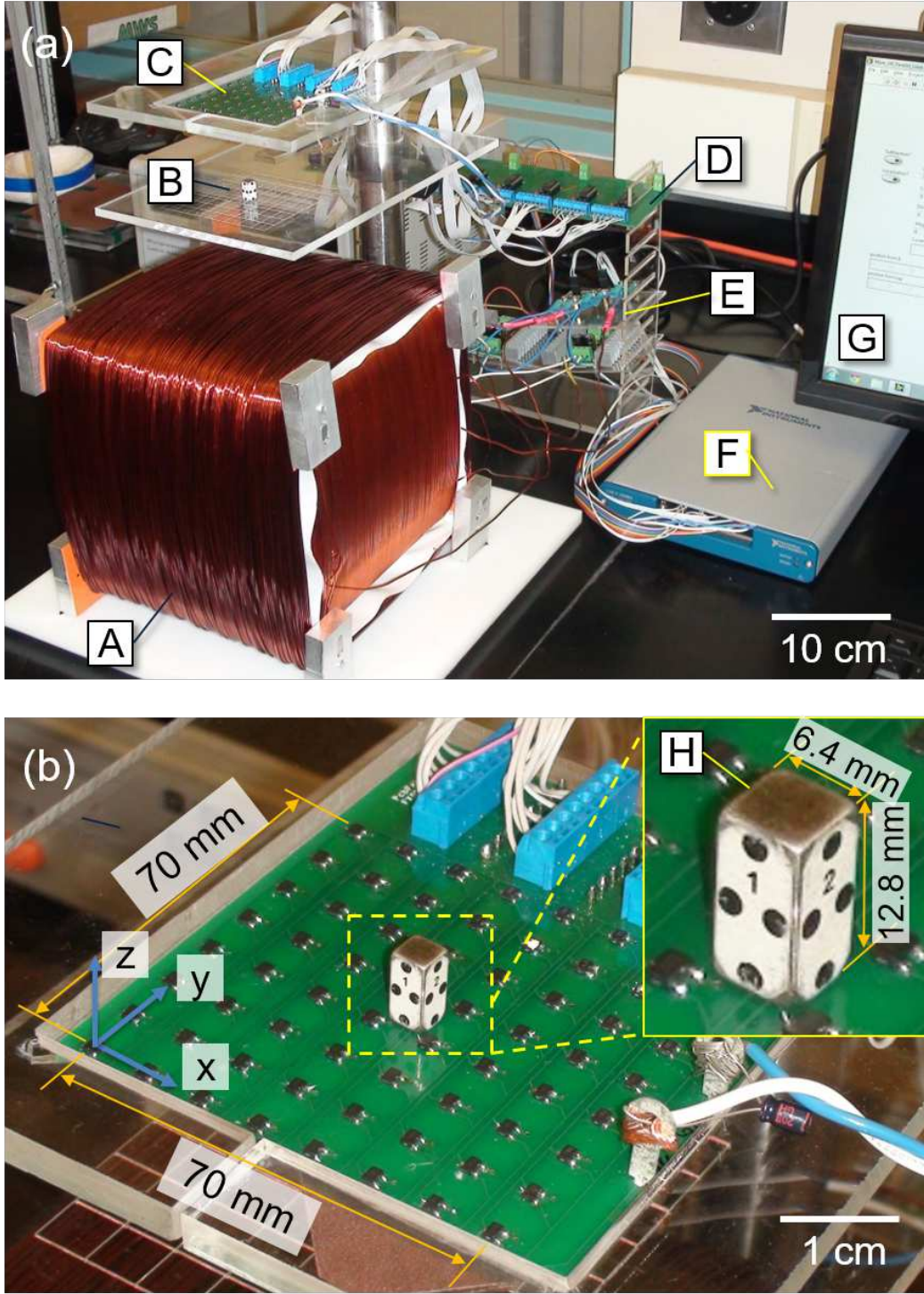


Figure 2.1: Photographs of the five-dimensional magnetic localization setup. (a) Overview; A: Omnidirectional electromagnet; B: Arena of the MACE; C: Two-dimensional mono-axial Hall-effect sensor array; D: Multiplexer board; E: Current sensors and current amplifier; F: Data-acquisition-board; G: Desktop computer, its monitor and Labview-based graphical user interface. (b) Close-up view of the Hall-effect sensor array. The z -directional Hall-effect sensors are located in the two-dimensional array with a nodal distance of 10 mm. H: MACE with visual markers on its surface. The size of the MACE is $6.4 \times 6.4 \times 12.8 \text{ mm}^3$, its material is NdFeB, and its magnetic moment is $0.45 \text{ A} \cdot \text{m}^2$.

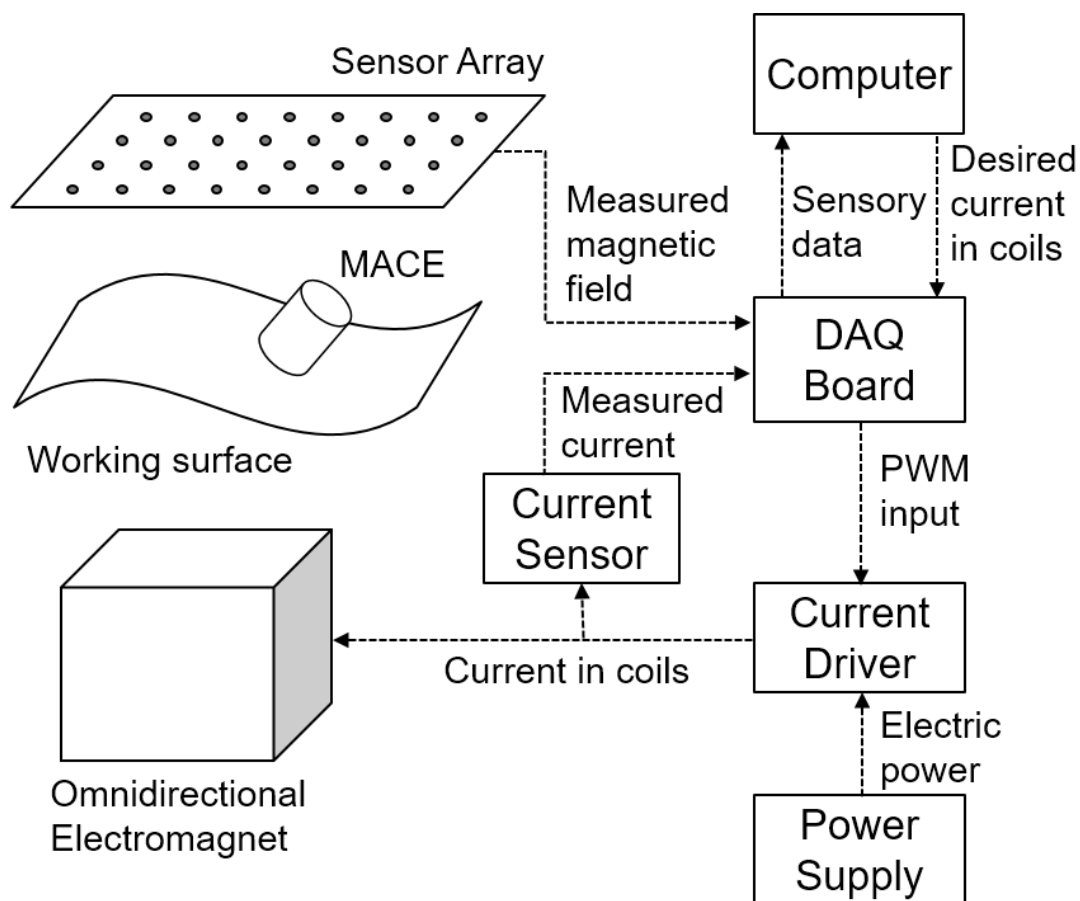


Figure 2.2: Overall signal flow of the system. Measured sensory data from Hall-effect sensor array and current sensors are fed to the computer through the DAQ board. Omnidirectional electromagnet is driven by current drivers. Multiplexer board is omitted in the diagram.

2.2 5-D Localization Method

2.2.1 Setup

Figure 2.1(a) shows the experimental setup, which consists of four main parts. The first part is the 2-D Hall-effect sensor array board. Sixty-four Hall-effect sensors on the board measure the magnetic field in the direction perpendicular to the array (z -direction in Fig. 2.1(b)) at each position. Increasing the number of sensors improves the accuracy of the localization results. In our setup, however, the number of analog input channels (8) of the DAQ board and the multiplexers (3 bit) limited the number of sensors that could be used. The second part is the omnidirectional electromagnet made of three box-shaped orthogonal coils and a soft iron core [41]. We fabricated our own version of the omnidirectional electromagnet for our study and the details are shown in Appendix A. The third part is the multiplexer board connecting the Hall-effect sensor outputs with the computer. Eight multiplexers on the board distribute the sensor signals to the data-acquisition-board. The last part is the desktop computer with a data-acquisition-board. The main algorithm and graphical user interface are implemented in Labview (National Instruments Co.) with an operation frequency of 200 Hz; the sampling rates of the data acquisition loop and the optimization algorithm loop are 1 kHz and 200 Hz, respectively. The specifications of the localization setup are presented in Table 2.1.

2.2.2 Working Principle

Figure 2.3 shows the application scenario of the developed 5-D localization method. Each dimension can be localized except the rotation axis of a magnetic moment of the robot. The goal is to estimate the position and orientation of the MACE while it is manipulated by the external magnet. We propose following two steps to decouple the effect of the external magnet at a point of interest (sensor position): 1) subtraction of a modeled magnetic field of the external magnet from measured data, and 2) second order directional differentiation to reduce the B-field error.

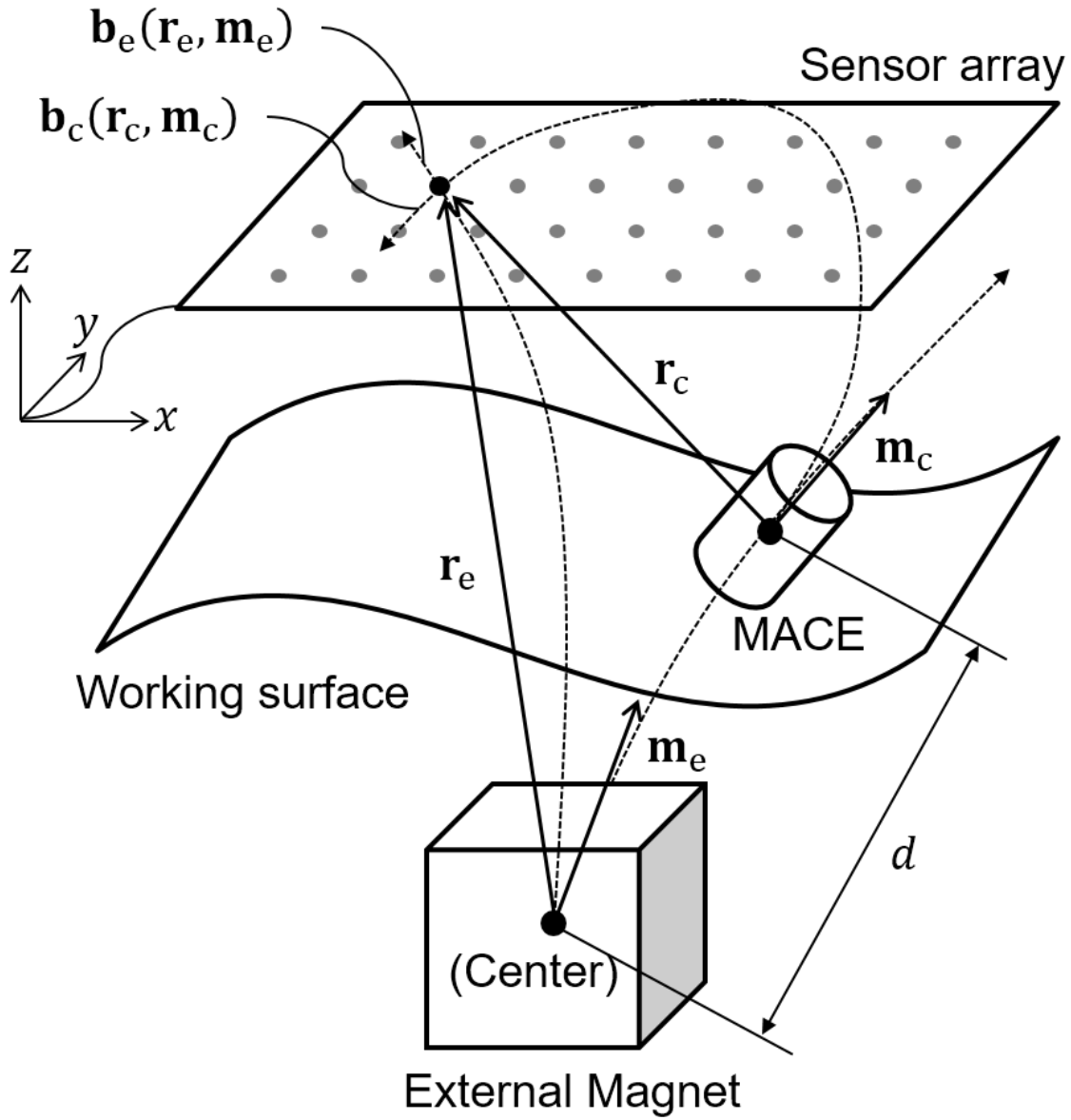


Figure 2.3: Schematic drawing of the application scenario. A MACE is manipulated by an external magnet in the 3-D space. The objective of this paper is to estimate the position (\mathbf{r}_c) and orientation (\mathbf{m}_c) of the MACE under the effect of the external magnetic field.

Table 2.1: Specification of the Localization Setup

	Value
Hall-effect sensors, A1389 (Allegro)	64 counts
- Nodal distance (x - and y -direction)	10 mm
- Sensitivity	9 mV/G
- Noise level	15 mV (=1.667 G)
- Measurement range	± 278 G
The omnidirectional electromagnet	
- Size	$193 \times 200 \times 200$ mm ³
- Magnetic moment (x -, y -, z -direction)	30.31, 30.22, 34.12 A·m ² /A
MACE	
- Dimensions	$6.4 \times 6.4 \times 12.8$ mm ³
- Magnetic moment	0.45 A·m ²
3-bit multiplexer (74HC/HCT4051, Phillips Semiconductors)	
Data-acquisition-board (NI USB 6343, National Instruments)	
Current driver (SyRen 25, Dimension Engineering)	
Current sensor (ACS714, Pololu Corporation)	

The magnetic sensors experience magnetic fields both from the MACE and the external magnet. Those magnetic fields are expressed as B-fields in (2.1):

$$\mathbf{b}_s = \mathbf{b}_c + \mathbf{b}_e \quad (2.1)$$

where \mathbf{b}_s is the measured B-field at a sensor, \mathbf{b}_c is the B-field of the MACE, and \mathbf{b}_e is the B-field of the external magnet. A simple way to estimate a pure \mathbf{b}_c is to subtract \mathbf{b}_e from \mathbf{b}_s . To subtract, we should model \mathbf{b}_e , and the general way to model a magnetic field is to use the magnetic dipole equation in a coordinate-free form,

$$\mathbf{b}_{\text{dpl}}(\mathbf{r}, \mathbf{m}) = \frac{\mu_0}{4\pi \|\mathbf{r}\|^3} (3\hat{\mathbf{r}}\hat{\mathbf{r}}^T - \mathbb{I})\mathbf{m} \quad (2.2)$$

where μ_0 is the permeability of free space, \mathbf{r} is the position vector (with associated unit vector $\hat{\mathbf{r}}$) from the magnetic source to the point of interest, \mathbf{m} is the magnetic moment vector of the

magnetic source, and \mathbb{I} is a 3×3 identity matrix. Thus, \mathbf{b}_e can be expressed using (2.2) as

$$\mathbf{b}_e = \mathbf{b}_{\text{dpl}}(\mathbf{r}_e, \mathbf{m}_e) \quad (2.3)$$

where \mathbf{r}_e is the position vector from the external magnet to the sensor position and \mathbf{m}_e is the magnetic moment vector of the external magnet. However, in actuality, we cannot measure the exact \mathbf{r}_e and \mathbf{m}_e , which results in the B-field error. Also the real magnetic field includes multi-pole magnetic fields, which are not modeled in (2.2). Thus, (2.1) can be rewritten as

$$\mathbf{b}_c = \mathbf{b}_s - [\mathbf{b}_{\text{dpl}}(\mathbf{r}_e, \mathbf{m}_e) + \mathbf{b}_{\text{err}}] \quad (2.4)$$

Here the B-field error, \mathbf{b}_{err} , is specified as

$$\begin{aligned} \mathbf{b}_{\text{err}} &= \mathbf{b}_s - \mathbf{b}_c - \mathbf{b}_{\text{dpl}}(\mathbf{r}_e, \mathbf{m}_e) \\ &= \mathbf{b}_{\text{dpl}}(\mathbf{r}_e + \mathbf{r}_{\text{err}}, \mathbf{m}_e + \mathbf{m}_{\text{err}}) + \mathbf{b}_{\text{quad}} \\ &\quad + \mathbf{b}_{\text{hexa}} + \dots - \mathbf{b}_{\text{dpl}}(\mathbf{r}_e, \mathbf{m}_e) \end{aligned} \quad (2.5)$$

where \mathbf{r}_{err} and \mathbf{m}_{err} are a positioning error and a magnetic moment measurement error of the external magnet, respectively. In (2.5), those two dipole terms scale with $\|\mathbf{r}_e\|^{-3}$ as described in (2.2), and the quadrupole term and the hexapole term scale with $\|\mathbf{r}_e\|^{-5}$ and $\|\mathbf{r}_e\|^{-7}$, respectively [58].

Because the error terms in (2.5) are inversely proportional to the distance, they reduce as the external magnet moves farther from the sensor array. Conversely, the B-field from the MACE increases as the MACE gets closer to the sensor array. To express this relationship, we define a new parameter, *Signal Quality Ratio* (SQR) in B-field, as

$$SQR_B = \frac{\|\mathbf{b}_c\|}{\|\mathbf{b}_{\text{err}} + N_s\|} \approx \frac{\|\mathbf{b}_c\|}{\|\mathbf{b}_{\text{err}}\|} \propto \left(\frac{\|\mathbf{r}_e\|}{\|\mathbf{r}_c\|} \right)^3 \quad (2.6)$$

where \mathbf{r}_c is a position vector from the sensor array to the MACE and N_s is a noise level of the sensor. The magnetic field error due to multi-pole terms in (2.5) is negligible as they are much smaller than the dipole term in (2.6). Note that, assuming that N_s is negligible, SQR_B is inversely proportional to the third order of the distance.

The directional differentiation of the analytical model (2.2) results in

$$\frac{\partial^2 \mathbf{b}_{\text{dpl}}(\mathbf{r}, \mathbf{m})}{\partial \|\mathbf{r}\|^2} = \frac{3\mu_0}{\pi \|\mathbf{r}\|^5} (3\hat{\mathbf{r}}\hat{\mathbf{r}}^T - \mathbb{I})\mathbf{m}. \quad (2.7)$$

The SQR in the second order differentiated B-field is expressed as

$$\begin{aligned} SQR_L &= \frac{\|\partial^2 \mathbf{b}_c / \partial \|\mathbf{r}_c\|^2\|}{\|\partial^2 (\mathbf{b}_{\text{err}} + N_s) / \partial \|\mathbf{r}_e\|^2\|} \\ &\approx \frac{\|\partial^2 \mathbf{b}_c / \partial \|\mathbf{r}_c\|^2\|}{\|\partial^2 \mathbf{b}_{\text{err}} / \partial \|\mathbf{r}_e\|^2\|} \propto \left(\frac{\|\mathbf{r}_e\|}{\|\mathbf{r}_c\|} \right)^5. \end{aligned} \quad (2.8)$$

Assuming that N_s is negligible, SQR_L is inversely proportional to the fifth order of the distance ratio. Because the $\|\mathbf{r}_e\|$ is larger than $\|\mathbf{r}_c\|$, SQR_L is always higher than SQR_B . The more the B-field is differentiated, the better SQR is achieved because of the scaling law. However, the number of the differentiation is limited by the number of the sensor elements and the noise is magnified by the differentiation. In this paper, the second order differentiation was sufficient for the given number of the sensors and the noise level of the sensors.

Another advantage of using the second order directional differentiation is that we can calculate the vertical directional differentiation using a lateral 2-D array of mono-axial Hall-effect sensors. Equation (2.9) is always valid at all positions based on Maxwell's equations in the absence of current or a changing electric field,

$$\nabla^2 \mathbf{b} = \frac{\partial^2 \mathbf{b}}{\partial x^2} + \frac{\partial^2 \mathbf{b}}{\partial y^2} + \frac{\partial^2 \mathbf{b}}{\partial z^2} = \mathbf{0}. \quad (2.9)$$

Equation (2.9) shows that the second order derivative in the z -direction equals a negative sum

of those in the x - and y -directions. Though Hall-effect sensors in the XY -plane measure the magnetic fields in the z -direction, the second order derivative in the z -direction can be calculated without using multiple layers in the z -direction based on the above property. Here, we define the second order z -directional derivative K as

$$K(x, y) = \frac{\partial^2 B_z}{\partial z^2} = -\frac{\partial^2 B_z}{\partial x^2} - \frac{\partial^2 B_z}{\partial y^2} \quad (2.10)$$

where B_z is a z -directional component of \mathbf{b} . In the two-dimensional sensor array, K is calculated by using the magnetic field of the neighboring sensors. Using the five-point stencil finite difference method, K at the sensor node (i, j) , or $K^{i,j}$, is expressed as

$$K^{i,j} \approx -\frac{B^{i,j-1} + B^{i,j+1} + B^{i-1,j} + B^{i+1,j} - 4B^{i,j}}{h^2} \quad (2.11)$$

where $B^{i,j}$ is the z -directional component of the \mathbf{B} -field measured by the sensor at the node (i, j) , and h is the nodal distance between neighboring sensors.

We conducted experiments to compare SQR_L with SQR_B in order to verify the analysis performed in (2.6) and (2.8). Because our setup measures only the z -directional components of the \mathbf{B} -field, we defined two new terms, $SQR_{z,B}$ and $SQR_{z,L}$ as (2.12) and (2.13).

$$SQR_{z,B}(\mathbf{r}_e, \mathbf{m}_e, \mathbf{r}_c, \mathbf{m}_c) = \frac{1}{n} \sum_i \sum_j \frac{|B_c^{i,j}(\mathbf{r}_c, \mathbf{m}_c)|}{|B_e^{i,j}(\mathbf{r}_e, \mathbf{m}_e) - B_{e,dpl}^{i,j}(\mathbf{r}_e, \mathbf{m}_e)|} \quad (2.12)$$

where n is the number of sensors, $B_c^{i,j}(\mathbf{r}_c, \mathbf{m}_c)$ is the z -directional magnetic field from the MACE, and $B_e^{i,j}(\mathbf{r}_e, \mathbf{m}_e)$ is the z -directional magnetic field from the electromagnet; each is measured by the sensor at node (i, j) in the absence of the other's magnetic field. $B_{e,dpl}^{i,j}(\mathbf{r}_e, \mathbf{m}_e)$

is the z -directional magnetic field of the electromagnet assuming the dipole model.

$$SQR_{z,L}(\mathbf{r}_e, \mathbf{m}_e, \mathbf{r}_c, \mathbf{m}_c) = \frac{1}{n} \sum_i \sum_j \frac{|K_c^{i,j}(\mathbf{r}_c, \mathbf{m}_c)|}{|K_e^{i,j}(\mathbf{r}_e, \mathbf{m}_e) - K_{e,dpl}^{i,j}(\mathbf{r}_e, \mathbf{m}_e)|} \quad (2.13)$$

where $K_c^{i,j}(\mathbf{r}_c, \mathbf{m}_c)$ and $K_e^{i,j}(\mathbf{r}_e, \mathbf{m}_e)$ are the second derivatives of the z -directional magnetic fields from the MACE and the external magnet, respectively. Both of these are calculated from (2.11). $K_{e,dpl}^{i,j}(\mathbf{r}_e, \mathbf{m}_e)$ is the second derivative of the z -directional magnetic field of the external magnet assuming the dipole model, which is calculated using (2.7).

Although SQR_z represents only the z -directional components of SQR, the comparison of $SQR_{z,L}$ and $SQR_{z,B}$ indirectly represents the effect of the scaling law in (2.6) and (2.8) on the signal quality. In the experiments, we set \mathbf{m}_c to $(0, 0, 0.45) \text{ A}\cdot\text{m}^2$ and \mathbf{m}_e to $(0, 0, 30.0) \text{ A}\cdot\text{m}^2$, and both $SQR_{z,B}$ and $SQR_{z,L}$ are measured for 10 seconds, then averaged.

Figure 2.4 shows that SQR_L is higher than SQR_B where the distance ratio ($\|\mathbf{r}_e\|/\|\mathbf{r}_c\|$) is larger than 1. This means that SQR_L becomes a clearer standard than SQR_B does. Especially, as \mathbf{r}_c becomes smaller and \mathbf{r}_e becomes larger, SQR_L increases exponentially while SQR_B stays in low level. These experimental results show that the proposed method gives better signal information than the B-field subtraction method.

2.2.3 Algorithm

The developed algorithm finds the optimal \mathbf{r}_c and \mathbf{m}_c by minimizing a cost function using the Levenberg-Marquardt Algorithm (LMA). LMA is a trust region based optimization method, which uses the steepest descent method for global convergence and Newton's method (quadratic method) for local convergence in a way that gives smooth transition between them [59]. This optimization solver is known as the efficient and effective solution for a magnetic marker local-

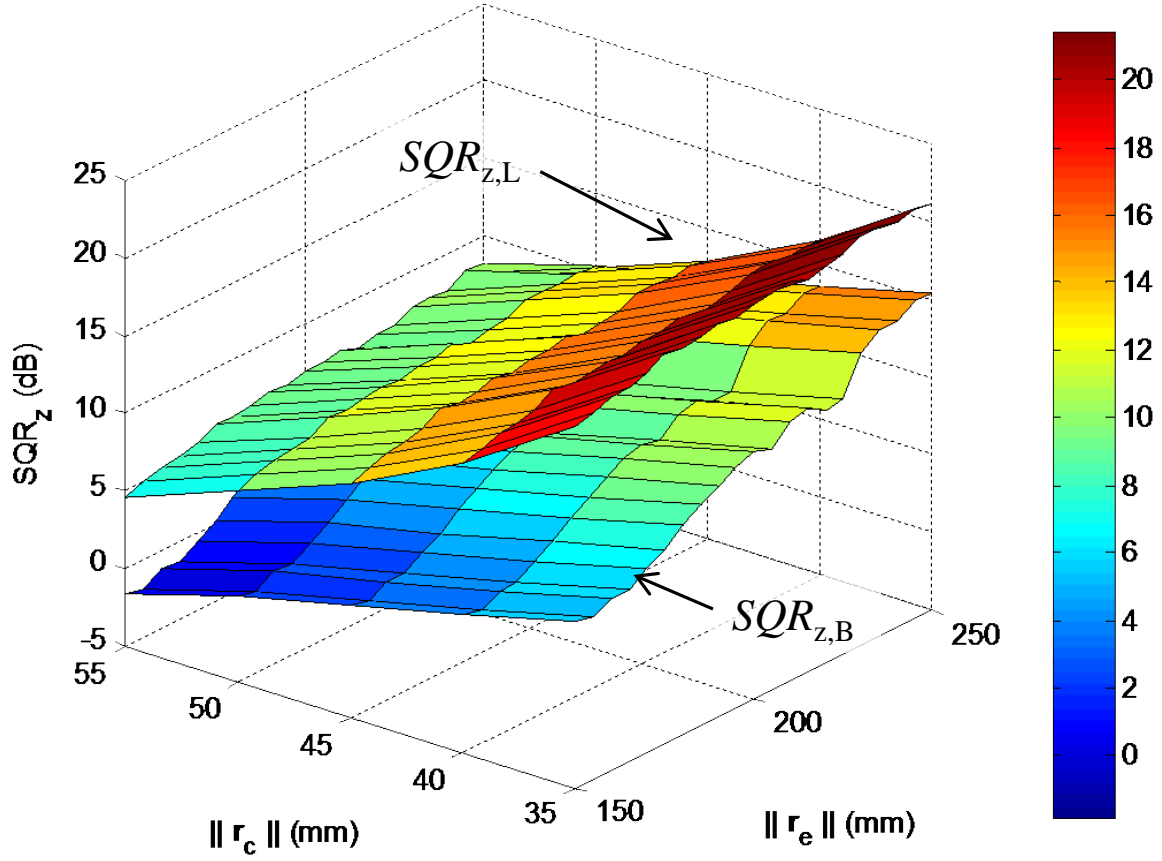


Figure 2.4: Experimental comparison of $SQR_{z,B}$ and $SQR_{z,L}$. $SQR_{z,L}$ is higher than $SQR_{z,B}$ in all regions. The z -directional distance from the MACE and the external magnet were set from 30 mm to 75 mm and 160 mm to 230 mm with 5 mm increments, respectively. The electromagnet generated 1 mT B-field at the center of the array in the $+z$ -direction. The measurement was done for 10 seconds.

ization problem [60]. The cost function is defined as

$$c = \sum_i \sum_j (K^{i,j} - K_{e,dpl}^{i,j}(\mathbf{r}_e, \mathbf{m}_e) - K_{c,dpl}^{i,j}(\mathbf{r}_c, \mathbf{m}_c))^2 \quad (2.14)$$

where $K^{i,j}$ is the second z -directional derivative of B-field based on the measured data at the sensor node number (i, j) and $K_{c,dpl}^{i,j}(\mathbf{r}_c, \mathbf{m}_c)$ is the MACE's modeled second z -directional derivative of B-field at the sensor node number (i, j) . $K_{dpl}^{i,j}$ is computed by using the following analytical equation, which is derived from (2.2),

$$\begin{aligned} K_{dpl}^{i,j}(\mathbf{r}, \mathbf{m}) &= \frac{\partial^2 B_z}{\partial z^2} \\ &= \frac{\mu_0}{4\pi} \left(\frac{9m_z}{\|\mathbf{r}\|^5} - \frac{45r_z(\mathbf{m} \cdot \mathbf{r} + m_z r_z)}{\|\mathbf{r}\|^7} + \frac{105r_z^3(\mathbf{m} \cdot \mathbf{r})}{\|\mathbf{r}\|^9} \right) \end{aligned} \quad (2.15)$$

where m_z is the z -directional component of \mathbf{m} and r_z is the z -directional component of \mathbf{r} .

Figure 2.5 shows a flow chart of the developed algorithm, and describes how each term of the cost function is calculated. The goal of the algorithm is to estimate the optimal \mathbf{r}_c and \mathbf{m}_c minimizing the cost function, (2.14). First, the measured magnetic field ($B^{i,j}$) is transformed to the second derivative ($K^{i,j}$) by using (2.11). Second, the electromagnet's input current (\mathbf{I}_e) gives the estimate of its magnetic moment (\mathbf{m}_e). Using the calculated \mathbf{r}_e , \mathbf{m}_e , and (2.15), we can obtain the second derivative of the electromagnet's B-field ($K_{e,dpl}^{i,j}(\mathbf{r}_e, \mathbf{m}_e)$). The key of the cost function is the last term ($K_{c,dpl}^{i,j}(\mathbf{r}_c, \mathbf{m}_c)$). The optimal \mathbf{r}_c and \mathbf{m}_c of the previous iteration become the initial conditions for the current \mathbf{r}_c and \mathbf{m}_c . The terms are calculated by (2.15), and iteratively updated by the optimization. The new optimal \mathbf{r}_c and \mathbf{m}_c that minimize the cost function become the current position and orientation of the capsule.

For a real-time application, the termination condition is important. In a numerical optimization, the termination of the loop is usually set by a threshold on the function value change during the last iteration, the search step size during the last iteration, or the number of iterations. In the real-time application, typically the threshold on the number of iteration guarantees a certain

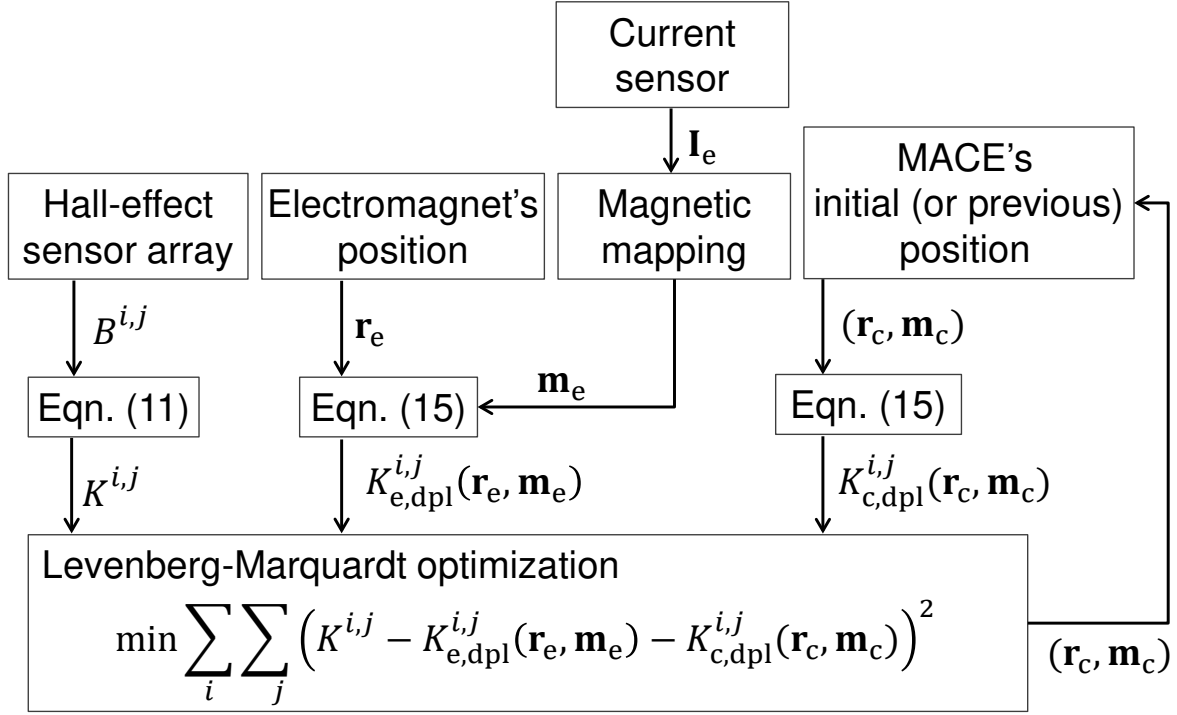


Figure 2.5: Block diagram of the main localization algorithm. The proposed algorithm minimizes the cost function to find the position (\mathbf{r}_c) and orientation (\mathbf{m}_c) of the MACE. Initial position and orientation of the MACE is continuously updated by the algorithm for the real-time tracking. Measured B-field's second derivative is calculated using Laplacian of the B-field, and the estimated second derivative of B-field is calculated using the second derivative form of the dipole equation.

time window for the optimization loop. Thus, the method should employ the number of iteration as the optimization termination condition. In the exemplary system, we used maximum 20 iterations which guarantees 5 ms. This value was achieved experimentally. MatLAB code for the algorithm is shown in Appendix E

2.3 Experiments

We conducted experiments to evaluate the accuracy and reliability of the developed localization methods. Since water and biological tissue do not affect the low frequency magnetic field, our simple and magnetically transparent experimental setup is applicable to magnetic capsule endoscopy. As a single magnet works as a magnetic source for both actuation and localization

in the proposed method, The MACE was represented by a box shaped ($6.4 \times 6.4 \times 12.8 \text{ mm}^3$) NeFeB magnet with $0.45 \text{ A} \cdot \text{m}^2$ magnetic moment. The work space for the MACE was given as $70(w) \times 70(d) \times 50(h) \text{ mm}^3$ below the sensor array. A plane with a slope was used for the working surface in the experiment (Fig. 2.6(b)). The external magnet, which was positioned 20 cm below the array, generated a 2.5 mT rotating magnetic field at the center of the MACE for climbing rolling locomotion. While it is rolling from the initial position, (20, -20, -35) mm, to the final position, (-18, 18, -20) mm, the proposed method ran in real-time at 200 Hz (limited by LMA loop speed) to track the position and orientation of the MACE. The B-field subtraction method ran in parallel with the proposed method for comparison. For the ground truth position and orientation, two video cameras recorded the MACE with visual markers (Fig. 2.6(a)). 5-D visual reference data was extracted using an image processing software [61].

A total of 10 experiments were conducted, with each experiment taking approximately 6 seconds for the MACE to traverse the surface. Each trial had the same initial condition and planned trajectory. All the manipulation and localization were done autonomously by the pre-programmed codes in LabView. Distance errors were measured by Euclidean distance and angular errors were measured by orientation vector difference using visual reference data.

Table 2.2 shows the summarized experimental results. Overall, the proposed method is more accurate than the B-field subtraction method. Its total average errors were $2.1 \pm 0.8 \text{ mm}$ (distance) and $6.7 \pm 4.3^\circ$ (angular), respectively, while the errors of the B-field subtraction method were $2.6 \pm 1.3 \text{ mm}$ and $8.3 \pm 6.5^\circ$, respectively. The fact that its maximum errors (4.7 mm and 30°) were much smaller than the others (10.5 mm and 50.3°) means that the proposed method is more stable. Figure 2.7(a)-(c) show the worst case error of the experimental trials. The proposed method more closely and more stably tracked the ground truth position than the B-field subtraction method did (see the abruptly increasing position errors near the initial position in Fig. 2.7(a)).

Error termination by the differentiation explains the improved accuracy. In the B-field subtraction method, the position and orientation of the MACE fluctuate because of the rotating

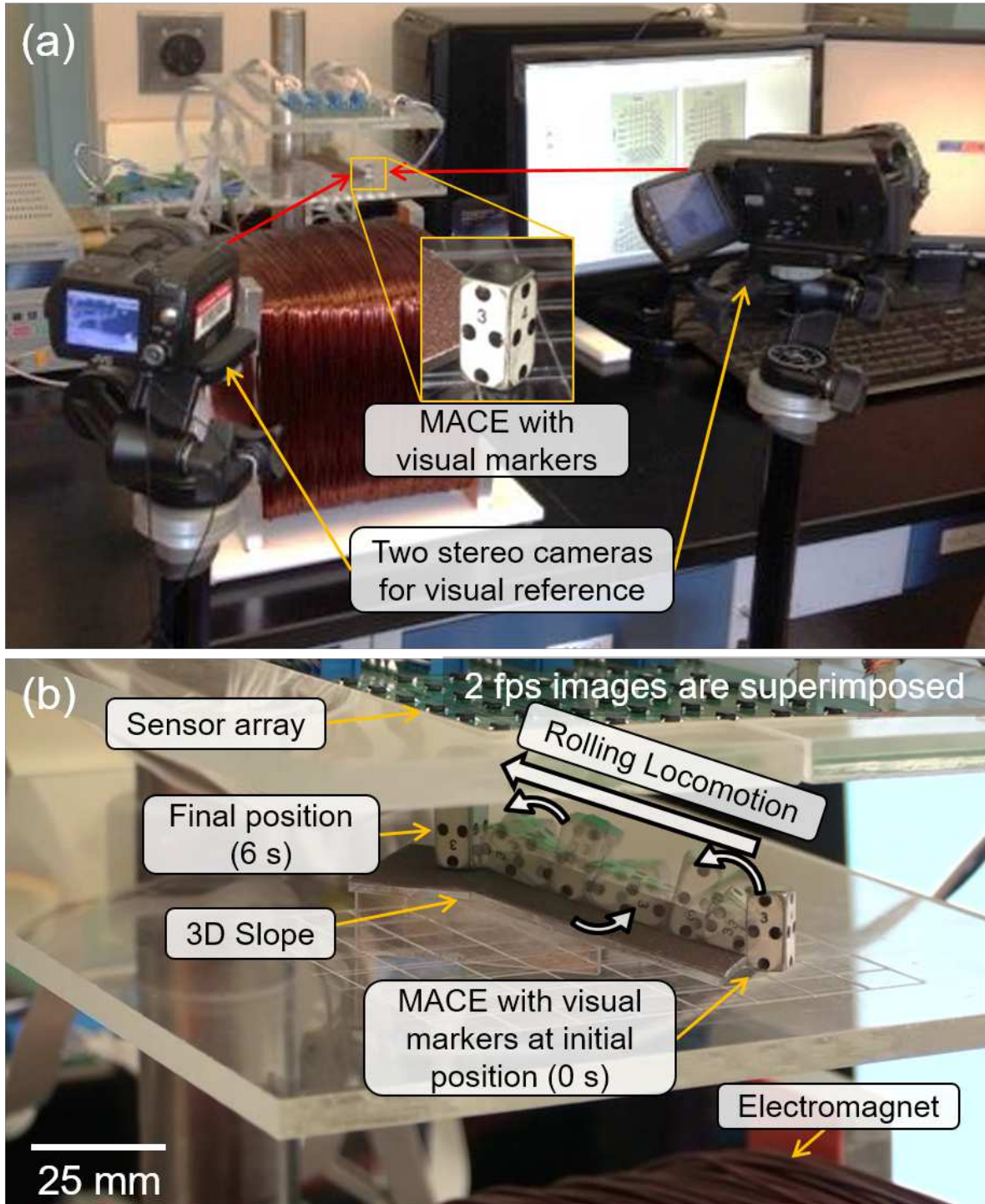
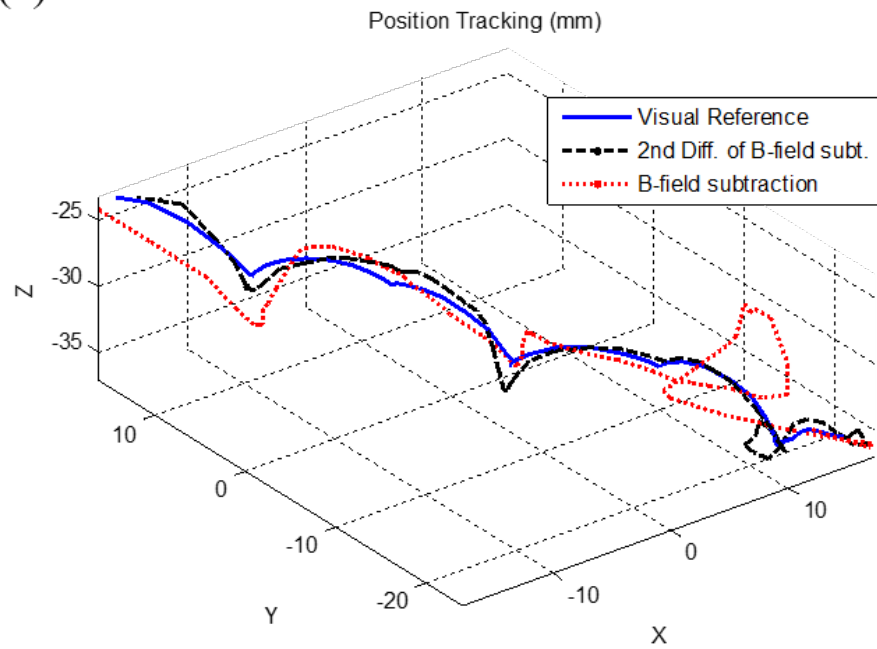


Figure 2.6: Experimental setup and the dynamic motion of the MACE. (a) The MACE has markers on its surface. We reconstructed the position and orientation of the moving robot using the markers in images. (b) The MACE traversed the slope with the external magnetic actuation which gave rolling locomotion to the MACE.

(a)



(b)

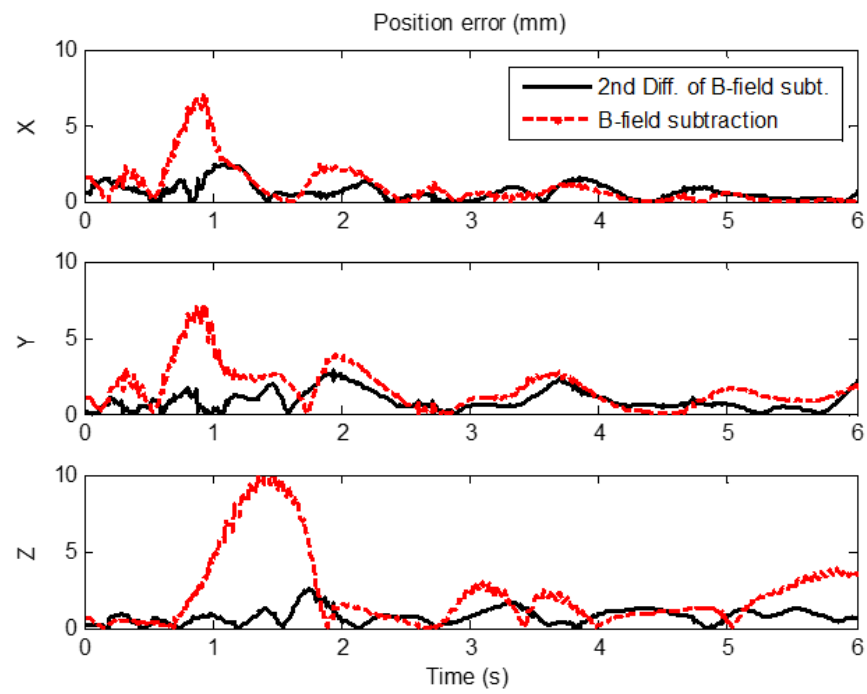


Table 2.2: Dynamic Motion Tracking Experiment Results

Number of trials=10*	Position error (mm)			Orientation error (°)		
	Avg.±Std.**	Min	Max	Avg.±Std.**	Min	Max
The proposed method	2.1±0.8	0.07	4.7	6.7±4.3	0.03	30.0
B-field subtraction method	2.6±1.3	0.4	10.5	8.3±6.5	0.07	50.3

* Each trial had the same initial condition and trajectory.

** The total average of the 10 experiments.

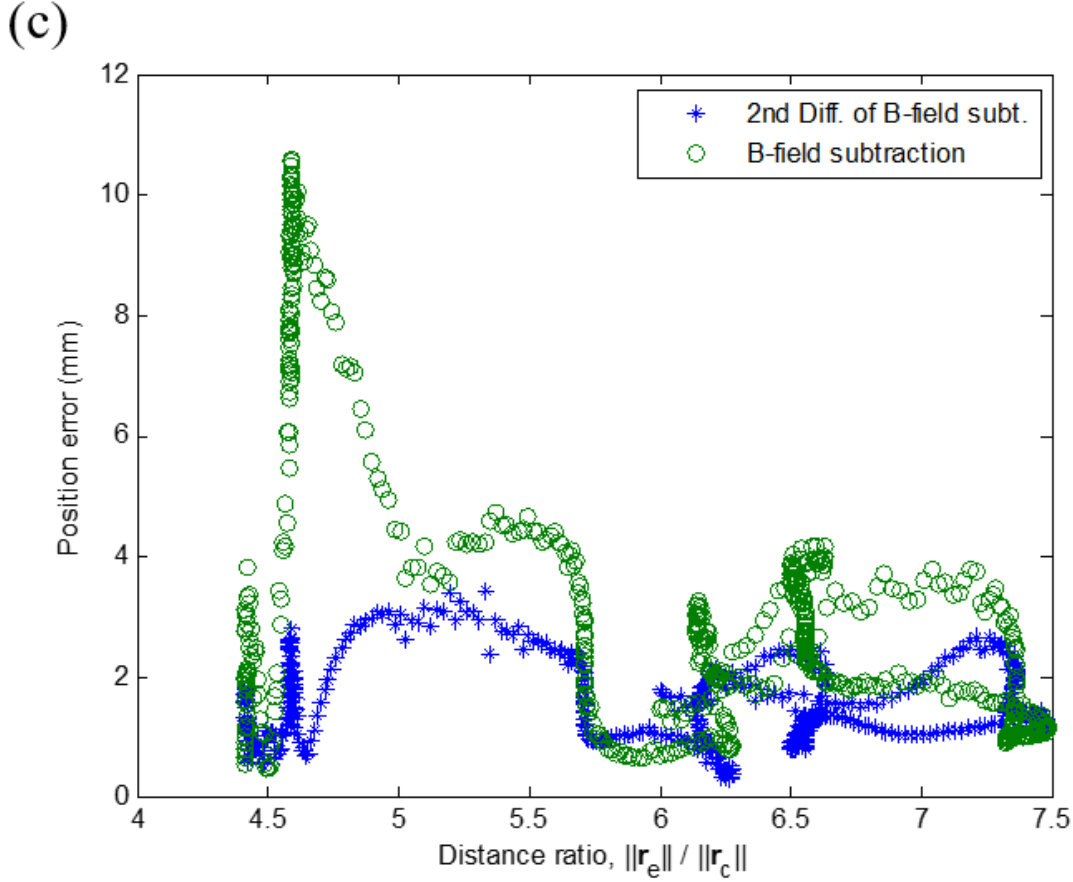


Figure 2.7: Result of the dynamic motion tracking experiment (the worst case). (a) The proposed method tracked the MACE in real-time with the external magnetic actuation. (b) While the B-field subtraction method had a significant loss of track near the starting point and errors in the middle of the track, the proposed method tracked the MACE's motion through the whole path with the minor error. (c) As the distance ratio, $\|\mathbf{r}_e\| / \|\mathbf{r}_c\|$, increases, the localization error shows a decreasing trend. The proposed method shows less positioning error than the B-field subtraction method in almost all ranges. The error fluctuates because of the rotating magnetic field of the MACE.

external magnetic field. This error is due to the magnetic field error in the analytical magnetic model in (2.5). This factor is still non-negligible and results in poor accuracy. However, by taking the proposed second order differentiation, those fluctuations are significantly reduced as shown in the plot. This method improves z -directional localization accuracy significantly, although it doesn't impact the x - and y -position accuracy (Fig. 2.7(b)) as it is applied in z -direction.

The distance ratio, $\|\mathbf{r}_e\|/\|\mathbf{r}_c\|$, is critical to localization accuracy. Although our nonlinear optimization method does not show an explicit relationship between SQR values and localization error, Fig. 2.7(c) shows that larger distance ratios correspond to smaller localization errors, and that the second derivative method yields smaller errors. These results are consistent with the theoretical analysis in (2.6) and (2.8).

2.4 Discussion

The developed real-time localization method gives accurate estimation of the position and orientation of a magnetically manipulated robot. This method doesn't require internal sensors, and allows to remain the mechanical and electrical configuration of the robot simple, which is useful for an untethered magnetic robot for medical applications where optical tracking is not possible. Table 2.3 shows the detailed comparison with other magnetic localization methods. Even though the effective distances in the experiments are different, the proposed localization method shows the smallest position error and the fastest speed for controlling a capsule robot in real-time compared to the other magnetic localization methods.

However, the proposed localization method would have a limited clinical application because of the short effective distance (< 50 mm). Beyond 50 mm, SQR values drop below 5 dB (see Fig. 2.4) even with the second derivative method. This means the noise and error terms occupy more than 36% of the whole measured signal. With such poor signal conditioning, the nonlinear optimization algorithm tends to either diverge or give unreasonable estimations.

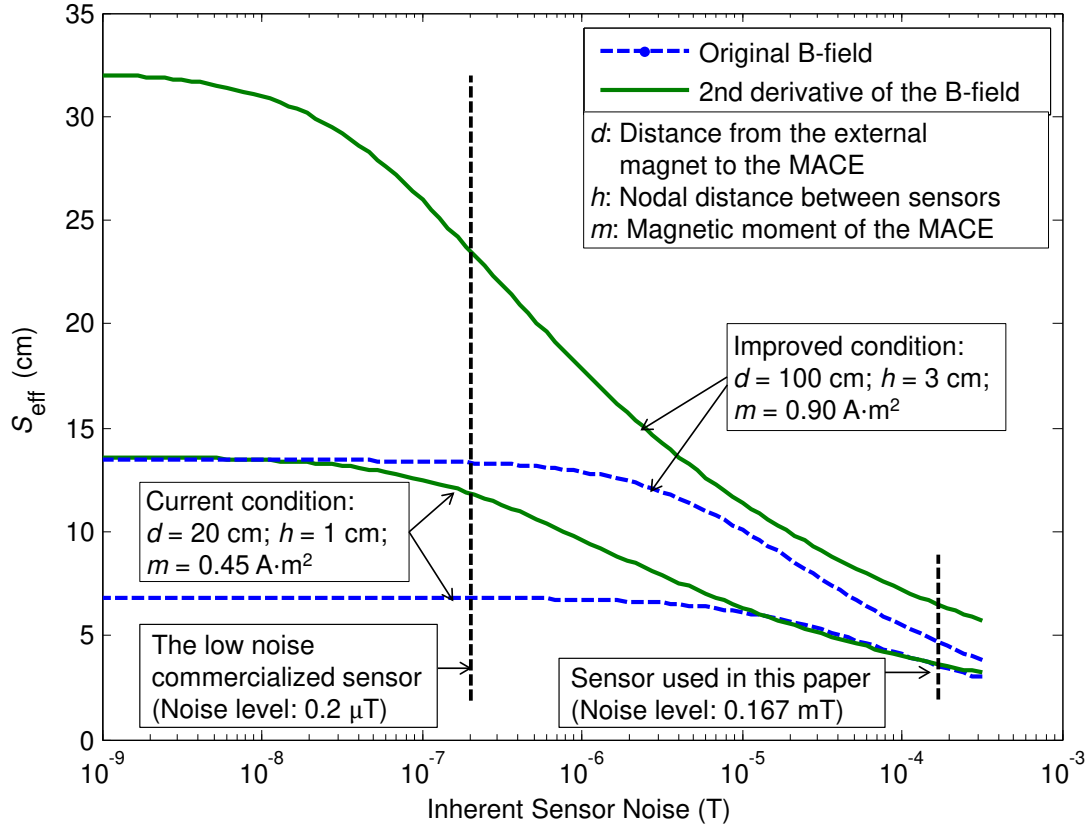


Figure 2.8: Simulated effective localization range (S_{eff}) as a function of the inherent sensor noise. With the (1, 1, 1) mm position misalignment and $1 \text{ A}\cdot\text{m}^2$ magnetic moment error from the external magnet, it is shown that the S_{eff} can be extended to 23 cm with the currently existing sensors. As inherent sensor noise gets smaller, it is preferable to use the second order derivative for better accuracy and long effective localization distance. The external magnetic field on the MACE was (0, 0, 3) mT.

Table 2.3: Comparison of Existing Magnetic Localization Methods with the Proposed Method

	Popek <i>et al.</i> [54]	Di Natali <i>et al.</i> [55]	Yim <i>et al.</i> [56]	The proposed method	Than <i>et al.</i> * [62][63]
Internal Sensor(s)	6 Hall-effect sensors	6 Hall-effect sensors + 1 tri-axial accelerometer	1 Hall-effect sensor	None	None
External Sensor(s)	None	None	None	64 Hall-effect sensors	2 pairs of gamma ray detectors
Position Error (mm)	11	3.4 ± 3.2	2.0	2.1 ± 0.8	0.4
Orientation Error ($^{\circ}$)	11	19 ± 50	5 ± 1.2	6.7 ± 4.3	2
Real-time (Loop speed)	No	Yes (14 ms)	No	Yes (5 ms)	Yes (2-3 ms)
Effective localization Range (mm)	136.0 - 144.0**	0 - 150	44.2 - 57.2	5 - 50	200 - 400

* Non-magnetic localization method (positron emission marker detection).

** Range in the experiment. Effective localization range is not shown explicitly in the paper.

The effective distance can be increased by using lower noise Hall-effect sensors and a bigger magnet. In the experiments, we used a small magnet ($6.4 \times 6.4 \times 12.8 = 524.3 \text{ mm}^3$, NdFeB, $0.45 \text{ A} \cdot \text{m}^2$), but doubling the volume of a cylindrical shape, ($\phi 11 \times 11 = 1,045 \text{ mm}^3$, NdFeB, $0.90 \text{ A} \cdot \text{m}^2$), would still be within the limits for a swallowable capsule endoscope (diameter $< 12 \text{ mm}$, length $< 30 \text{ mm}$). We simulated the effective distance as a function of the inherent sensor noise. We assumed that 20 dB is the minimum SQR level for quality localization (same as 10% error) to determine the effective distance, S_{eff} . In the simulation, the original equations, including noise terms from (2.6) and (2.8), were used. Figure 2.8 shows the relationship between the inherent sensor noise and S_{eff} . Both the B-field subtraction method and the proposed method have increased effective distances as the inherent sensor noise decreases. While the B-field

subtraction method saturates at 13 cm, the second derivative method shows a maximum of 23 cm effective distance without saturation using currently existing sensors (e.g., MMC3316xMT, MESMIC co, RMS noise: 0.2 μT). Additionally, an extremely low inherent noise sensor, such as 0.02 μT RMS noise level sensors, would give nearly 30 cm of S_{eff} , which satisfies the effective range guideline of magnetic capsule endoscopy.

Further, changing the design parameters affect the S_{eff} . These parameters are the distance from the external magnet to the MACE, d , the nodal distance between sensors, h , and the magnetic moment of the MACE, m . A large value of d improves S_{eff} because the long actuation distance minimizes the effect of the external magnetic field, which is effectively filtered by the directional differentiation. On the other hand, a small value of h reduces S_{eff} because it increases the effect of the noise after the directional differentiation. This is because the directional differentiation operator gives the division by h in the equation (2.11). A large value of m improves the S_{eff} because it increases the magnetic field on the sensor array. Additionally, it reduces the effect of the external magnetic field on the sensor array because a weaker magnetic field is required to generate the same force and torque compared to when the value of m is small.

The method could be used in different size scales of magnetic robots. As we discussed above, using a strong and big magnetic robot is much beneficial in terms of the localization. A strong magnetic source generates a strong magnetic field which is easy to be detected by the magnetic sensing system. The strong magnetic field on the sensor array will improve the signal to noise ratio. Additionally, the actuation magnetic field does not need to be strong for the actuation of the robot, because the force and torque are proportional to the magnetic moment of the magnetic source. This will reduce the overall actuation magnetic field, which minimizes the external magnetic field on the sensor array. These two facts, 1) the strong signal from the magnetic robot and 2) the less disturbing external magnetic field, will enhance overall SQR. In a small scale, it appears opposite to the large scale magnetic robots. In a small scale magnetic robot localization, the magnetic field from the magnetic robot dramatically reduces because the magnetic moment is proportional to the volume of the robot, which scales to the three power

of the length of the robot. On the other hand, the magnetic field required to actuate the robot increases to the three power of the body length because the actuating magnetic field has to compensate the loss of the magnetic moment from the size reduction.

A simulation study is conducted to quantitatively verify the effect of the size of the robot on the effective localization range, S_{eff} . Fig. 2.9 shows the simulation result. It is shown that S_{eff} (20 dB SNR) is proportional to the edge length of the robot in a log scale. The second order differentiation makes the curve flatter than the B-field subtraction method, which helps to localize micro magnetic robots in a relative longer distance than the B-field subtraction method. Additionally, S_{eff} is also a function of the nodal distance between sensors, h . A high value of h makes the magnetic field weak at the edge of the sensor array. Thus, it is better to reduce h for a better SQR. However, in the case of second order differentiation solution, too small value of h increases the effect of the sensor noise due to the property of the spatial numerical differentiation in Eq (2.11). In the simulation, h value which is equal to 10% of S_{eff} gave the best result among different h values. This simulation assumes that we use current state-of-art magnetic sensors, such as fluxgate sensors (4 nT noise level), for the sensor array, and NdFeB N52 for the material for the magnetic object to be localized.

As a large scale magnetic object, a magnetic object with $1 \text{ m} \times 1 \text{ m} \times 1 \text{ m}$ could be localized at 3 m distance. A magnetic object with $10 \text{ cm} \times 10 \text{ cm} \times 10 \text{ cm}$ volume could be localized at 50 cm distance. In mesoscale, a $1 \text{ cm} \times 1 \text{ cm} \times 1 \text{ cm}$ could be localized at 12 cm. In milli-scale, a magnetic object with $1 \text{ mm} \times 1 \text{ mm} \times 1 \text{ mm}$ volume could be localized at 3 cm. In microscale, a magnetic object with $100 \text{ }\mu\text{m} \times 100 \text{ }\mu\text{m} \times 100 \text{ }\mu\text{m}$ would be localized in 8 mm distance. In this analysis, the localization of small scale magnetic robots appears challenging due to the short localization distance. The short range not only limits the placement of the magnetic sensor array in applications, but also causes sensor saturation problems. Because the sensor system is very close to the magnetic robot, the actuation magnetic field applies almost directly to the magnetic sensors. Especially very sensitive magnetic sensors for the localization of the small magnetic objects, the sensor system would be easily saturated by the actuation magnetic field,

which would lead to a failure of the magnetic localization. For example, a fluxgate sensor with 4 nT resolution will be saturated at 20 μ T magnetic field actuation even with 16-bit resolution. This will significantly limit the actuation of the magnetic robots. In conclusion, the magnetic localization of a magnetic object smaller than $1\text{ mm} \times 1\text{ mm} \times 1\text{ mm}$ volume would not be practical. In those size scales, it seems other localization modality, such as X-ray or ultrasonic localization, is practical because the detection ranges are not directly affected by the volume of the object.

2.5 Summary

In this chapter, we introduced a new real-time 5-D localization method for an untethered meso-scale magnetic robot, which is manipulated by a computer-controlled external electromagnetic system. The developed magnetic localization setup is a 2-D array of mono-axial Hall-effect sensors, which measure the perpendicular magnetic fields at their positions. We propose two steps for localizing the magnetic robot more accurately. First, the dipole modeled magnetic field of the electromagnet is subtracted from the measured data in order to determine the pure magnetic field from the magnetic robot. Next, the subtracted magnetic field is twice differentiated in the perpendicular direction of the array, so that the effect of the electromagnetic field in the localization process is minimized. Five variables regarding the position and orientation of the magnetic robot are determined by minimizing the error between the measured magnetic field and the modeled magnetic field in an optimization method. The resulting position error is $2.1 \pm 0.8\text{ mm}$ and angular error is $6.7 \pm 4.3^\circ$ within the applicable range (5 cm) of magnetic field sensors at 200 Hz. The proposed localization method would be used for the position feedback control of untethered magnetic devices or robots for medical applications in the future.

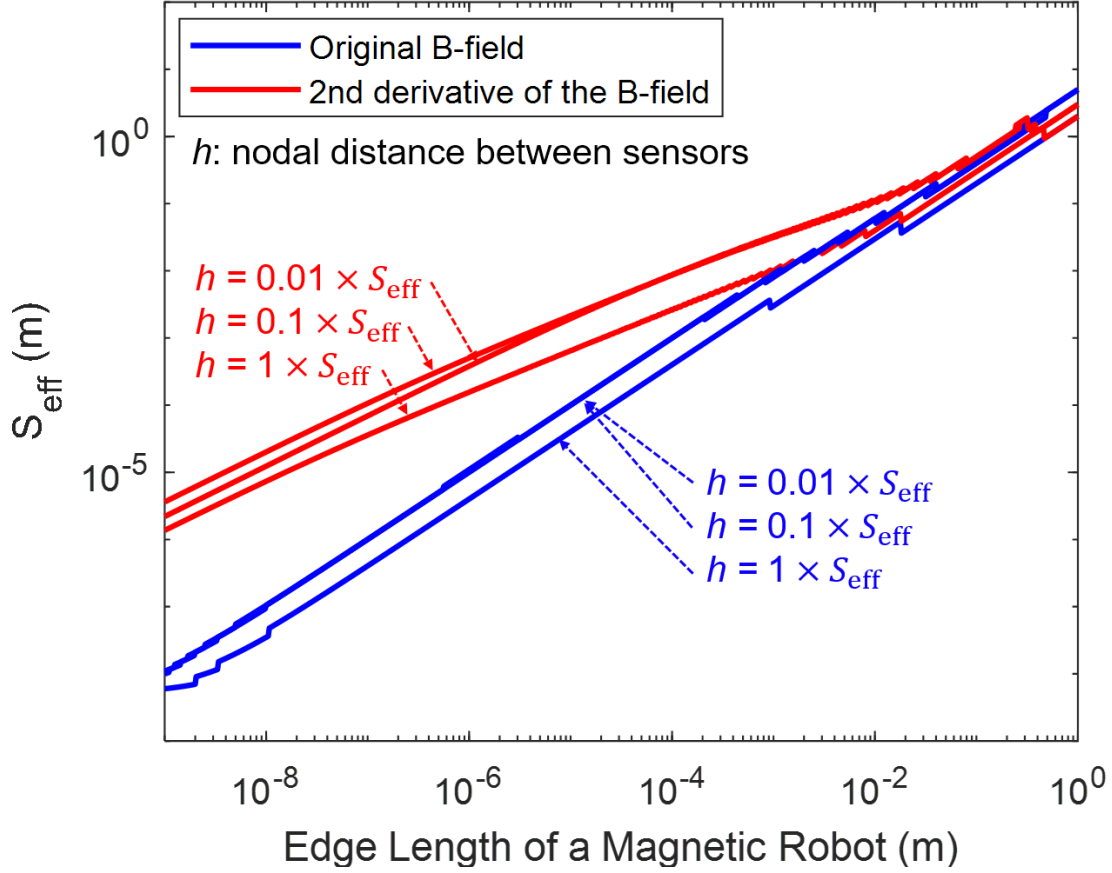


Figure 2.9: Simulated effective localization range (S_{eff}) as a function of an edge length of a magnetic robot. It is shown that the effective localization range reduces proportional to the size of the robot in a log scale. The second order directional differentiation makes the slope flatter than the slope of the original B-field subtraction method. The nodal distance between sensors (h) affect S_{eff} . Especially in the second order directional derivative case, h value of 0.1 gave the longest S_{eff} . In the B-field subtraction method, S_{eff} saturates when h is smaller than 0.1 of the S_{eff} value. The simulation employs the current state-of-art magnetic sensor (fluxgate sensor with 4 nT noise level), sensor position misalignments proportional to the robot body length (l), and 1% magnetic moment error from the external magnet.

Chapter 3

A Simultaneous Calibration Method for Magnetic Robot Localization and Actuation Systems

3.1 Introduction

We have shown the localization of the magnetic robot under the magnetic actuation in the previous chapter. The method yields basic information for the control, e.g., where the robot is or how the robot orients. Additionally, the method is compatible with the magnetic actuation. However, before controlling the MACE, there is a step required: calibration of sensing and actuation systems.

We combined the magnetic actuation and sensor system. In the previous chapter, we used 64 mono-axial magnetic sensors and an Omnimagnet as the magnetic actuator. However, the combination of both systems can have various configurations. Figure 3.1(a) shows a system developed as a second generation of the actuation and localization in our group, where the actuators are differently configured. This new design is to improve the localization quality as well as the actuation performance. This system allows a larger workspace compared with

uniform magnetic field generators, such as Helmholtz coils [64]. This system demonstrated its capability on controlling a magnetic soft capsule endoscope on a plastic stomach model with a swine tissue model *in vitro* [65].

The combined system requires a high standard calibration. This is because the sensor and actuation systems share the magnetic field, where the magnetic fields from the robot and the actuation system are superimposed together. In such a case, the decoupling of the robot's magnetic field from the actuator's field relies on a precisely calibrated parametric magnetic model [66]. Inaccurate actuation and sensing models could lead to a false position and orientation estimation of the robot. This could cause an error or a failure of the control for the magnetic robot.

One way to calibrate a combined magnetic actuation and sensing system is to independently calibrate the actuation system and the sensing system. For the calibration of the magnetic sensor system, the position, orientation, and gain of each sensor can be calibrated either individually or simultaneously. For example, for the individual calibration, Pang *et al.* [67] proposed a non-linear model to calibrate a single triaxial magnetometer, which could capture both the manufacturing errors and non-linear effects using a non-linear optimization. However, this method is not applicable for calibrating the magnetic sensor array, where the relative positions and orientations among sensors are also critical to estimate the position and orientation of the robot. For the simultaneous calibration, Hu *et al.* [68], Plotkin *et al.* [69], and Li *et al.* [70] proposed calibration methods of using a permanent magnet as a reference source. These methods find sensors' calibration parameters based on a numerical optimization by using measurement data when the permanent magnet is in different positions and orientations. For the calibration of an actuation system, Petruska *et al.* introduced a method to calibrate multi-core electromagnetic actuation systems [71]. The method uses a numerical optimization with a multi-pole magnetic field model. Measurement data are gathered using a pre-calibrated Gauss meter, when the actuation system generates the magnetic field.

The other way to calibrate both systems is simultaneous calibration of both systems by us-

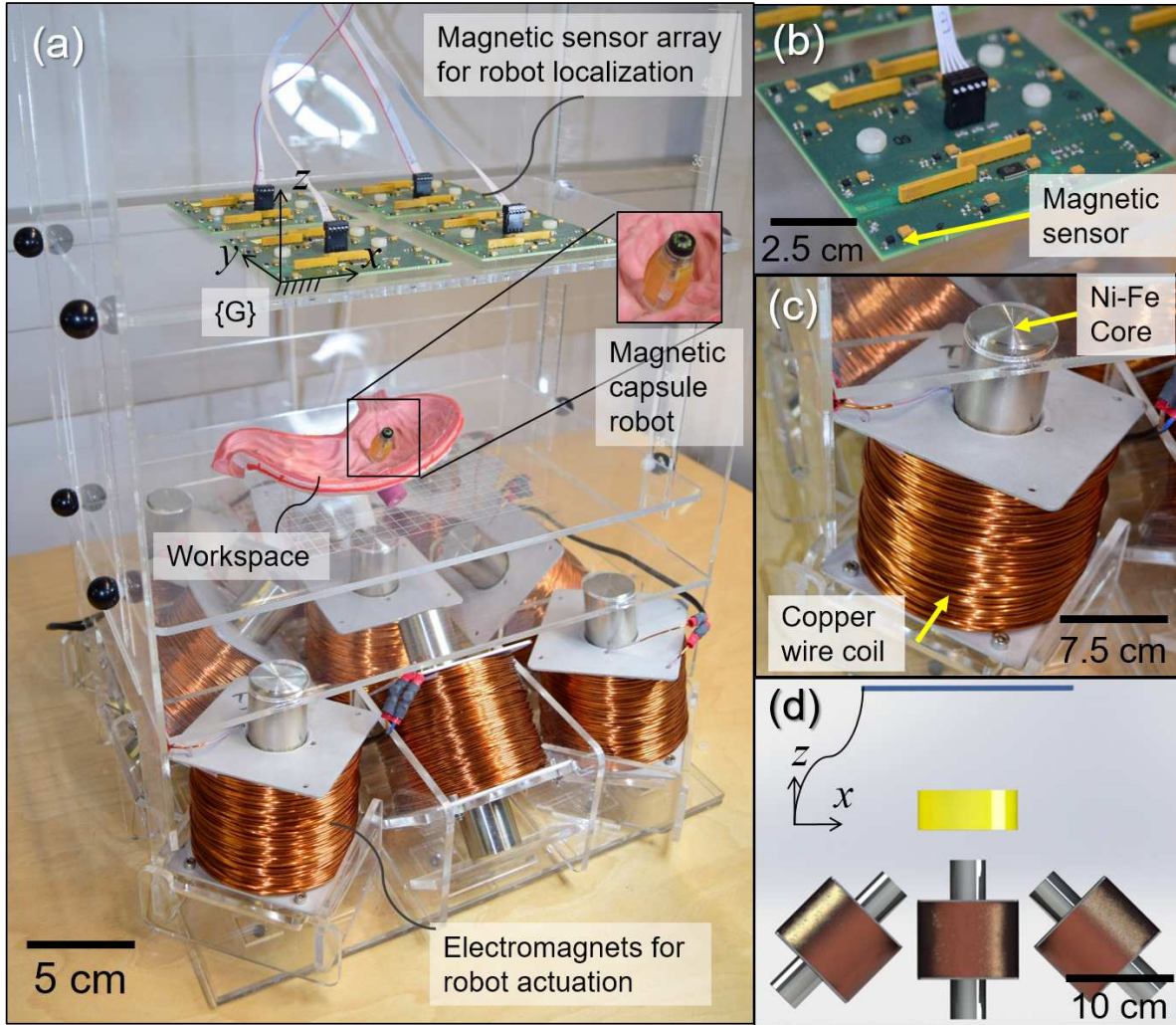


Figure 3.1: Experimental setup of the proposed magnetic localization and actuation system. (a) A magnetic robot is localized by a magnetic sensor array and actuated by nine electromagnets with Ni-Fe cores. The sensor array is placed in the other side of the workspace to avoid saturation due to the magnetic field of the actuators. In the current configuration, the sensor array is placed 250 mm above the electromagnets. The global frame is attached to the corner of the sensor array. (b) Close-up view of the magnetic sensor. Magnetic sensors are placed on a 8×8 grid with 30 mm spacing. (c) Close-up view of one of the electromagnets. (d) Side view of the system CAD image. Grey cylinders: magnetic cores ($\phi 36 \times 160 \text{ mm}^3$). Brown hollow cylinders: copper coils ($\phi(40-100) \times 80 \text{ mm}^3$). Yellow cylinder: workspace ($\phi 100 \times 40 \text{ mm}^3$) located 130 mm above the center of the central core (center to center). Blue thin box: sensor array ($210 \times 210 \text{ mm}^2$) placed 250 mm above the central core.

ing uncalibrated electromagnets as calibration sources. The simultaneous calibration method is advantageous over separate calibration methods in several aspects. First, the simultaneous calibration method enables automated self-calibration of the system, which improves the accuracy and the speed of the calibration process. This is because a large data set is provided by the automated process in a relatively short time, without errors from manual operations. The whole procedure can be done in fifteen minutes with a good precision in a real system. Second, the simultaneous calibration method allows a coordination calibration between a sensor system and an actuation system, which is not possible with the separate methods. Third, the simultaneous automatic calibration method enables system parameter updates for both long-term correctness and flexible reconfiguration for specific tasks.

In this chapter, we propose a simultaneous calibration method for both the magnetic sensor and actuator systems by formulating the calibration problem using a bundle adjustment (BA) framework [72]. In this method, the parameters of both the sensor and actuation systems can be solved simultaneously. The actuation system generates magnetic fields, and the sensor system logs the measurements of the magnetic fields correspondingly. An over-complete set of measurements are used to construct a system of equations. The system parameters include positions, orientations, and sensitivities of all the sensors, and the electromagnets' positions and magnetic moments. Here we assume that the positions of the sensors are known. Randomly generated magnetic fields from the electromagnets are modeled by the magnetic dipole field equation, and the measurements of the fields in magnetic sensors are modeled by a three-dimensional (3-D) polynomial model. The system parameters are estimated by solving a large scale optimization problem (1,836 parameters). We also provide a necessary constraint to fix a gauge freedom[72] to eliminate a freedom in the choice of a magnetic scale. The method was applied to general solenoid type magnetic actuation systems, OctoMag[73] and its large-scaled version[71], in simulated environments using finite-element-analysis (FEA) tools, and a custom designed magnetic sensing and actuation system (Fig.3.1 (a)) in experiments. In all cases, the calibrated models showed over 99.45% coefficients of determination (R^2 values).

This chapter is organized as follows: Section 3.2 introduces the simultaneous calibration method. In Section 3.3 and 3.4, the proposed method is verified by simulations and experiments. Section 3.5 discusses benefits and limitations of the method, and Section 3.6 concludes with a summary of the research.

3.2 Simultaneous Calibration Method

In the simultaneous calibration method, the uncalibrated sensors and electromagnets work as calibration sources. Although the parameters of the system are inaccurate before the calibration, all the parameters for the sensor and actuation systems are calibrated simultaneously by the property of the calibration model in Section 3.2.4. It is assumed that the current sensors are pre-calibrated before the calibration and the positions of the magnetic sensors are known.

The method is composed of three steps. First, the electromagnets generate a number of random magnetic fields. For each trial, the magnetic field is measured by magnetic sensors while the electric currents are measured by a current sensor at each coil. Second, the magnetic field of a known sample magnet is measured by the sensor array. The sample magnet is placed inside the workspace with an arbitrary position and orientation. Third, all the measurement data are fed into the calibration model, and a numerical solver estimates the solution.

For readability, we use small non-italic bold letters for vectors, italic capital letters for matrices, italic small letters for variables, and non-italic double-bold letters for spaces or stacked matrices.

3.2.1 System Description

The targeted calibration system is composed of a magnetic sensor array and a set of electromagnets. The final application of the system is to control a magnetic robot using the actuation system (electromagnets) while the magnetic robot is localized by a localization algorithm using

sensor data.

The sensor array measures magnetic fields from a magnetic robot and the electromagnets. The magnetic sensor can be either mono-axial or multi-axial. In this paper, the authors used triaxial sensors as a harder example to calibrate. With the coupled magnetic fields from the magnetic robot and the actuators, the robot can be localized by an algorithm from [66]. Details of the selection of the magnetic sensors and the design of the sensor array are explained in C

The actuation system generates desired magnetic fields and their spatial gradients at the center of the magnetic robot. The magnetic field is non-uniform throughout the workspace. Systems using non-uniform solenoidal magnetic field, such as OctoMag [73] or MiniMag [74], could be categorized as an applicable system. The example system (Fig. 3.1(a)) has sixty-four sensors and nine electromagnets. The configuration is explained in our previous work [65] and the design methodology of such a system is described in Appendix B

3.2.2 Framework: Calibration as Bundle Adjustment

Bundle adjustment (BA) has been employed in online simultaneous localization and mapping (SLAM) [75] and offline structure from motion (SfM) [76], which enables precise recovery of the parameters of both the sensors and landmarks. It is essentially an optimization-based method that can handle the simultaneous estimation of large numbers of parameters. It can be robust to external noises in the measurements. In the case where the measurement noise is zero-mean and normally distributed, BA solves a maximum likelihood estimation problem [72].

In our method, the measurements of the electric currents and the magnetic field can be treated equivalently as the feature points of the images in BA. The positions, orientations, and gains of the actuators and sensors are similar to the parameters of landmarks and camera(s). These parameters are constrained by the magnetic field dipole model under specific conditions.

In order to solve the calibration problem in the BA framework, we must consider parameterization, error modeling, building constraints, removing gauge freedom, and choosing a proper

Table 3.1: Parametrization

i -th Sensor Parameter ($1 \leq i \leq N$)	Symbol and Space
Position vector	$\mathbf{r}_i \in \mathbb{R}^3$
Non-orthogonal sensitivity matrix with rotation	$G_i \in \mathbb{R}^{3 \times 3}$
Quadratic sensitivity matrix	${}^x H_i, {}^y H_i, {}^z H_i \in S\mathbb{R}^{3 \times 3}$
j -th Actuator Parameter ($1 \leq j \leq M$)	
Position vector	$\mathbf{r}_j \in \mathbb{R}^3$
Magnetic moment vector	$\mathbf{m}_j \in \mathbb{R}^3$
k -th Measurement Values ($1 \leq k \leq L$)	
i -th magnetic sensor reading	$\mathbf{v}_{ik} \in \mathbb{R}^{3N}$
j -th current sensor reading	$I_{jk} \in \mathbb{R}^M$

* \mathbb{R} : Euclidean space; $S\mathbb{R}^{3 \times 3}$: n -dimensional symmetric matrix

N, M, L : The total number of sensors, actuators, and measurements

optimization solver.

3.2.3 Parametrization

The proposed method involves a large set of parameters (the example system in the experiment has 1,836 parameters to be calibrated). In such a large parameter space, an appropriate parametrization is required for a reliable optimization result [72]. The parameter set is composed of sensor parameters and actuator parameters. The system of the parameters are represented in Fig. 3.2 and Table 3.1.

Sensor Parameters

A sensor has parameters for position, orientation, axes distortion, and gain (either linear or non-linear). For a general sensor calibration, we regard each sensor has a non-linear response and a cross-coupling effect among the axes. The non-linearity is attributed by hard-iron or soft-iron effect from ferrous material on the circuit board [77]. The distortion of axes is attributed by fabrication errors from the manufacturing process or thermal stress from the soldering process. In the case of an extremely sensitive triaxial magnetometer, such as a fluxgate magnetometer, the transverse field effect (TFE) becomes an additional source for the non-linearity and cross-

coupling effects [78]. A couple of models are presented to capture the non-linearity and the axes distortion [67, 79]. These models are for single triaxial magnetometers, so the axis rotation is neglected assuming that the axis rotation is pre-calibrated. However, in general, a system with multiple sensors might have a different orientation for each sensor. This is because the fabrication process might change the orientations, or different orientations can be intended to increase the signal to noise ratio to a certain direction. Involving the non-linearity, cross-coupling, and sensor rotation, a 3-D polynomial model could be used. The model can be easily expanded by

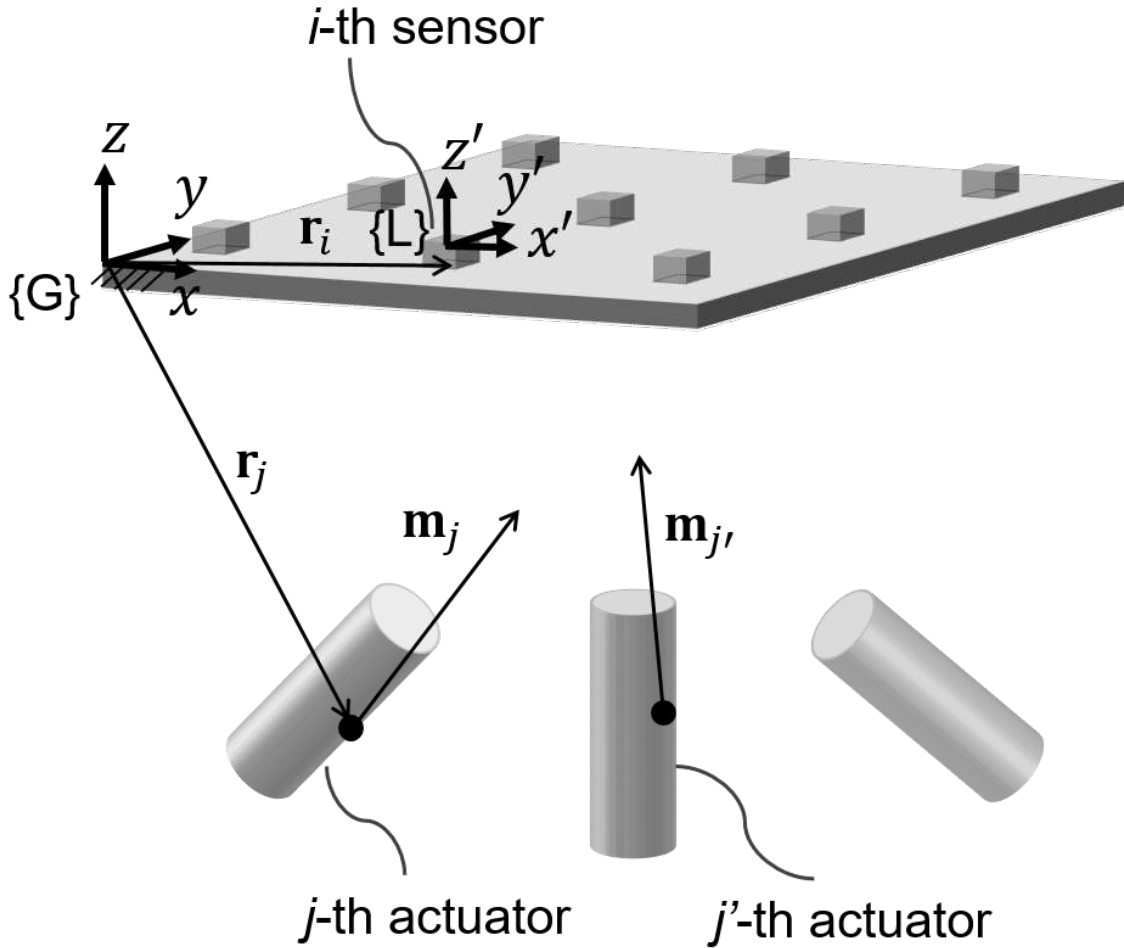


Figure 3.2: Geometric parameters of the sensor and actuation systems. All the position vectors and rotation matrices are expressed in the global frame, $\{G\}$. The local frame, $\{L\}$, is used to express gains of the sensors. \mathbf{m}_j and $\mathbf{m}_{j'}$ shows magnetic moments of j - and j' -th actuators, respectively. Black dots show the shifted magnetic center of the actuators due to mutual inductions.

increasing the order of the polynomials with the expense of computation.

In this paper, we use a 3-D quadratic model. This model is not only able to capture the non-linearity of the sensors precisely, but is also computationally practical. The 3-D quadratic model with sensor orientations involves 27 parameters for each sensor. The authors assume that the position of the sensors are known. The experimental setup has 64 sensors, thus 1,782 parameters for sensors are presented.

Actuator Parameters

A magnetic actuator has a position, an orientation, and a magnetic moment. A typical electromagnet has a coil and a core, and their axes are aligned together. In such a case, the orientation and the magnitude of the magnetic moment of the electromagnet can be combined into a 3-D vector. A system with more than two cores has a mutual induction which might change the magnetic center's position and the magnetic moment's orientation compared to a single electromagnet is presented. The experimental setup has 9 actuators, thus 54 parameters for actuators are presented.

3.2.4 Calibration Model

The calibration model is based on a sensor measurement model and a magnetic actuation model. The magnetic field from the actuators are measured by the magnetic sensors, and the values are expressed in arbitrary units. Additionally, the electric currents are measured by the current sensors attached to the actuators. We assume that the current sensors are the only reliable sensors with zero-mean Gaussian noise corruption.

Sensor Measurement Model

The magnetic field is measured by the magnetic sensor array. A single sensor reads the magnetic flux density, or the B-field, through the voltage difference across the ends of a magneto-

sensitive resistor. We assume that the sensor is non-linear, of which the axes are skewed and rotated, and the gains are different from the factory specifications. Using a quadratic model, the recovered B-field on the i -th sensor at the k -th measurement is

$$\bar{\mathbf{b}}_{ik}(\mathbf{p}_{s,i}, \mathbf{v}_{ik}) = G_i \mathbf{v}_{ik} + \begin{bmatrix} \mathbf{v}_{ik}^\top H_{x,i} \mathbf{v}_{ik} \\ \mathbf{v}_{ik}^\top H_{y,i} \mathbf{v}_{ik} \\ \mathbf{v}_{ik}^\top H_{z,i} \mathbf{v}_{ik} \end{bmatrix} \quad (3.1)$$

where $\mathbf{p}_{s,i}$ is an array of parameters for G_i , $H_{x,i}$, $H_{y,i}$, and $H_{z,i}$. In this expression, G_i is a linear mapping with no additional constraints, meaning it represents the effects of scaling, rotation, and shear. $H_{x,i}$, $H_{y,i}$ and $H_{z,i}$ are symmetric 3×3 matrices, which involve rotations and quadratic terms together. Note that the other symbols are explained in Table 3.1.

As each sensor in the sensor array has multiple measurements, it is convenient to express the recovered B-field values from the whole measurements in a stacked matrix form as

$$\bar{\mathbb{V}}_s(\mathbf{p}_s, \mathbf{v}) = \begin{bmatrix} \bar{\mathbf{b}}_{11}(\mathbf{p}_{s,1}, \mathbf{v}_{11}) & \cdots & \bar{\mathbf{b}}_{1L}(\mathbf{p}_{s,1}, \mathbf{v}_{1L}) \\ \vdots & \ddots & \vdots \\ \bar{\mathbf{b}}_{N1}(\mathbf{p}_{s,N}, \mathbf{v}_{N1}) & \cdots & \bar{\mathbf{b}}_{NL}(\mathbf{p}_{s,N}, \mathbf{v}_{NL}) \end{bmatrix} \quad (3.2)$$

where \mathbf{p}_s and \mathbf{v} are stacked vectors for all $\mathbf{p}_{s,i}$ and \mathbf{v}_{ik} , respectively.

B-field Actuation Model

The system described in Fig. 3.1a can be effectively modeled by the dipole magnetic field. This assumption is useful when a large-scale optimization is involved because the dipole model avoids intensive computations, but gives accurate estimation. A method using the magnetic dipole model to fit the magnetic field for a workspace is presented in [73]. The method uses a magnetic dipole to fit the magnetic field of a unit-current contribution. By increasing the number and the order of magnetic poles, more accurate model could be achieved [71]. In this method,

high order magnetic poles, such as quadrupole, hexapole, and octupole, are introduced. These high-order poles are essentially solutions from spherical harmonics to solve Laplace equation of the magnetic scalar potential. Due to the large search space for the optimization, it is preferable to have the least amount of parameters. In the current problem, the authors chose a single dipole model for each unit-current contribution as the method in[73]. A detailed analysis on the accuracy of the model with respect to the model complexity is present in Section IV.

The dipole magnetic field on the i -th sensor from the j -th actuator at the k -th measurement is expressed as

$$\begin{aligned} \mathbf{b}_{ij,k} &= B_{ij} \mathbf{m}_j I_{jk}; \\ B_{ij} &\equiv \frac{\mu_0}{4\pi \|\mathbf{r}_{ij}\|^3} (3\hat{\mathbf{r}}_{ij} \hat{\mathbf{r}}_{ij}^\top - \mathbb{I}), \quad \mathbf{r}_{ij} \equiv \mathbf{r}_i - \mathbf{r}_j \end{aligned} \quad (3.3)$$

where $\mathbf{b}_{ij,k}$ is the magnetic field vector in \mathbb{R}^3 , B_{ij} is a 3×3 matrix which only depends on the displacement vector, $\hat{\cdot}$ is a unit vector normalization operator, \mathbb{I} is the identity matrix, and μ_0 is the permeability of free space.

For magnetically actuated robots, multi-degrees-of-freedom (DOF) actuation is preferred as it can give more authority to control the robot, and avoid singularities or reduce the energy consumption using the redundancy. Because the magnetic field is superimposed at a point, we can consider the sum of the magnetic fields from each actuator as the resultant magnetic field.

The magnetic field at multiple measurement points from multiple current inputs could be expressed in a matrix equation as

$$\mathbf{b}_k = \mathbb{B} \mathbf{m} \mathbf{i}_k \quad (3.4)$$

where

$$\mathbb{B} = \begin{bmatrix} B_{11} & \cdots & B_{1M} \\ \vdots & \ddots & \vdots \\ B_{N1} & \cdots & B_{NM} \end{bmatrix}, \quad \mathbb{M} = \begin{bmatrix} \mathbf{m}_1 & \cdots & \mathbf{0} \\ \vdots & \ddots & \vdots \\ \mathbf{0} & \cdots & \mathbf{m}_M \end{bmatrix},$$

\mathbf{b}_k is the modeled magnetic field on all the sensors in a stacked vector form, \mathbb{B} is the actuation matrix from magnetic moments to the magnetic field on each sensor, \mathbb{M} is the magnetic moment package for the actuators (diagonal: magnetic moments, off-diagonal: zero-vectors), and \mathbf{i}_k is the measured electric current for all the actuators in a stacked form at the k -th measurement.

Similar to the sensor measurement model, (3.2), it is convenient to express the B-field values into a stacked matrix form as

$$\mathbb{V}_a(\mathbf{p}_a, \mathbf{i}) = \begin{bmatrix} \mathbf{b}_1 & \cdots & \mathbf{b}_L \end{bmatrix} = \mathbb{B}\mathbb{M} \begin{bmatrix} \mathbf{i}_1 & \cdots & \mathbf{i}_L \end{bmatrix} = \mathbb{B}\mathbb{M}\mathbb{J} \quad (3.5)$$

where \mathbf{p}_a is a vector including all the actuation parameters, \mathbf{i} is a stacked vector for all \mathbf{i}_k , and \mathbb{J} is a stacked matrix for all the current measurements.

3.2.5 Formulation of a Cost Function

Here, the optimization goal is to find the optimal actuation/sensor parameters based on the observation data. In the bundle adjustment framework, this goal is indirectly achieved by minimizing the errors between the prediction from the model and the measurement. In our problem, this optimization goal is achieved by formulating a cost function whose input parameters are the parameters we laid out in Parametrization section.

In a mathematical form, the cost function is formed to minimize the errors between the B-field values given by the sensor model, (3.2), and the actuation model, (3.5). The problem can be stated in a least square manner,

$$\begin{aligned}
& \underset{\mathbf{p}_s, \mathbf{r}_j}{\text{minimize}} \quad ||\bar{\mathbf{V}}_s - \mathbb{B}\mathbf{M}\mathbf{J}||_F^2 \\
& \text{subject to} \quad \mathbf{p}_{s,\text{lb}} \preceq \mathbf{p}_s \preceq \mathbf{p}_{s,\text{ub}} \\
& \quad \mathbf{r}_{j,\text{lb}} \preceq \mathbf{r}_j \preceq \mathbf{r}_{j,\text{ub}}, \quad 1 \leq j \leq M \\
& \quad g(\mathbf{p}_s) = 0
\end{aligned} \tag{3.6}$$

where $|| \cdot ||_F$ is the Frobenius norm; \mathbf{p}_s is the sensor parameters in (3.2); $\mathbf{p}_{s,\text{lb}}$ and $\mathbf{p}_{s,\text{ub}}$ are sensor parameters' lower and upper boundaries, respectively; $\mathbf{r}_{j,\text{lb}}$ and $\mathbf{r}_{j,\text{ub}}$ are actuator position parameters' lower and upper boundaries, respectively; \preceq is an element-wise (general) inequality symbol. These boundaries come from the manufacturing tolerance or estimation tolerance for each parameter. $g(\cdot)$ is an additional constraint to resolve the gauge freedom, which is described in (3.8).

Minimum Number of Measurements

The total number of the equations should be larger than the total number of parameters to solve the optimization problem. The total number of the equations is a multiplication of the number of the sensor elements, $3N$ (in case of a triaxial sensor), and the total number of measurements, L . Additionally, we have an additional constraint for the optimization, $g(\cdot)$, which gives one more equation. The total number of parameters are the sum of the number of the sensor parameters, $27N$, and the number of actuator parameters, $6M$. This formulates an inequality, $3NL + 1 \geq 27N + 6M$, which results in

$$L \geq 9 + \frac{6M - 1}{3N}. \tag{3.7}$$

Although the minimum number of the measurements is defined, it is beneficial to collect measurement data more than the minimum number to improve calibration accuracy. The large number of data minimizes Gaussian error from the sensor system effectively through the opti-

mization process.

Resolving Gauge Freedom

There is a gauge freedom in the magnetic scale. The measurements are invariant under a scaling of either the norm of the magnetic moment mapping, \mathbb{M} , or the norm of one of the G_i values. To resolve the gauge freedom, we need to introduce a physical reference which can give absolute values for the magnetic scale.

The physical reference is introduced using a permanent magnet whose magnetic moment is known. By measuring the magnetic field of the permanent magnet inside the workspace, the magnetic moments of the actuators and the gain for the sensors are related with the physical values.

A ‘temporary’ value for the gauge freedom parameter would be needed for a better calibration. This is because the measurement of the magnetic field of the permanent magnet is not redundant as the measurement of the magnetic fields from the electromagnets (number of the sample is much smaller and the noise is not compensated). The temporary value can be re-corrected after the first calibration. Although the measurement of the magnetic field from the reference magnet is a one-time measurement, it is preferred to expose the sensors to the magnetic field of the magnet for a long period of time and take the mean value of the measured data. This process would minimize the effect of Gaussian noise during the measurement of the reference magnet.

The temporary magnetic scale is added on the cost function. We can fix the magnetic scale by constraining either the sensor gain or the magnetic moment of the actuator to a certain number. The sensor gain might be close to the real value as it is specified in the manufacturer’s data sheet. Fixing the mean value of the gain of the sensors as the best pre-knowledge (magnetometer

specification data) as

$$\text{mean}\left(\frac{\|G_i\|_F^2}{3}\right) - g^2 = 0 \quad (3.8)$$

where g is the gain value of the sensors in the specification sheet. Adding (3.8) to the constraint in the scalar function $g(\cdot)$ of (3.6) finalizes the formulation for the optimization task.

Reassignment of Global Reference

We have fixed the gauge freedom to the ‘temporary’ value in the previous section. The value should be corrected according to the absolute physical value. This procedure should be performed after the first main optimization task.

The reference reassignment process involves additional optimization; however, we use the result parameters from the first optimization. We can formulate the optimization task to find the magnetic scale of the system compared with the reference magnet. The optimization is formulated as

$$\underset{\alpha, \mathbf{r}_r, \hat{\mathbf{n}}_r}{\text{minimize}} \quad \|\alpha \bar{\mathbf{V}}_s(\mathbf{p}_s, \mathbf{v}_r) - \begin{bmatrix} B_{1r} & \cdots & B_{Nr} \end{bmatrix}^\top \hat{\mathbf{n}}_r m\|_2^2 \quad (3.9)$$

where α is the magnetic scale correction factor, \mathbf{v}_r is the magnetic field measurement data when the reference magnet is in the workspace, B_{ir} is formulated using relative positions, $\mathbf{r}_i - \mathbf{r}_r$, \mathbf{r}_r is the position of the reference magnet, $\hat{\mathbf{n}}_r$ is the orientation vector of the reference magnet, and m is the known magnetic moment of the reference magnet.

Using α from the optimization, we can reassign magnetic scales as

$$G_i^* = \alpha G_i, \quad H_i^* = \alpha H_i, \quad \mathbf{m}^* = \alpha \mathbf{m} \quad (3.10)$$

where the ‘*’ symbol means a corrected value.

3.2.6 Choosing a Numerical Solver

We choose interior-point algorithm (IPA) [80] to solve the bundle adjustment problem. Because the non-linear optimization problem stated in (3.6) has both equality, (3.8), and inequality constraints (box constraints for the boundaries), and a high-dimensional parameter space to optimize over, we need an optimization solver which can handle the constraints well. We use the built-in function *fmincon* with the ‘interior-point’ setting in Matlab (MathWorks, Inc.). MabLab codes for the method is provided in Appendix F

3.3 Simulation Results

The proposed method was tested in a simulation environment, where all the system parameters are known as the ground-truth for the ease of comparison. As a general solenoid type magnetic actuation system, we chose OctoMag[73] and its large-scaled version[71] as simulation models (Configurations are shown in Fig. 3.3(a-b). Those systems are modeled in a commercialized finite-element-analysis (FEA) software (COMSOLTM, Comsol group).

The sensor system is simulated based on the data sheet of the sensor for the experiments (LIS3MDL, STMicroelectronics). The sensor array has sixteen sensors in a 2-D grid, and the sensor array was placed tangent to the workspace. The placement of the sensor array is to simulate a system which uses the sensor array as a localization system, where the sensor array does not disturb the movement of the magnetic robot, but close to sense the magnetic field from it.

From the ground-truth configuration, random magnetic fields were generated with random electric current inputs. The random electric currents and magnetic fields were measured with virtual electric current sensors and magnetic sensors with Gaussian noises. The magnetic sensors have 900 nT standard deviation (STD) gaussian noise, and the current sensors have 10 mA STD Gaussian noise. These measurements were fed into the optimization task, (3.6). The

parameter boundaries were 5% offset from the ground-truth values, except the magnetic moments as they are hard to predict before the calibration. From the given configuration, there were 675 parameters and 1 non-linear constraints in total. For the termination condition of the optimization, the first-order optimality tolerance was set to the noise level of the sensors.

The validation data set is generated separately to check the accuracy of the model. The actuation model validation set is the B-field set inside the workspace, when coils are running with arbitrary inputs. The sensing model validation set is the B-field set at the place of the sensor array with different current inputs than training datasets.

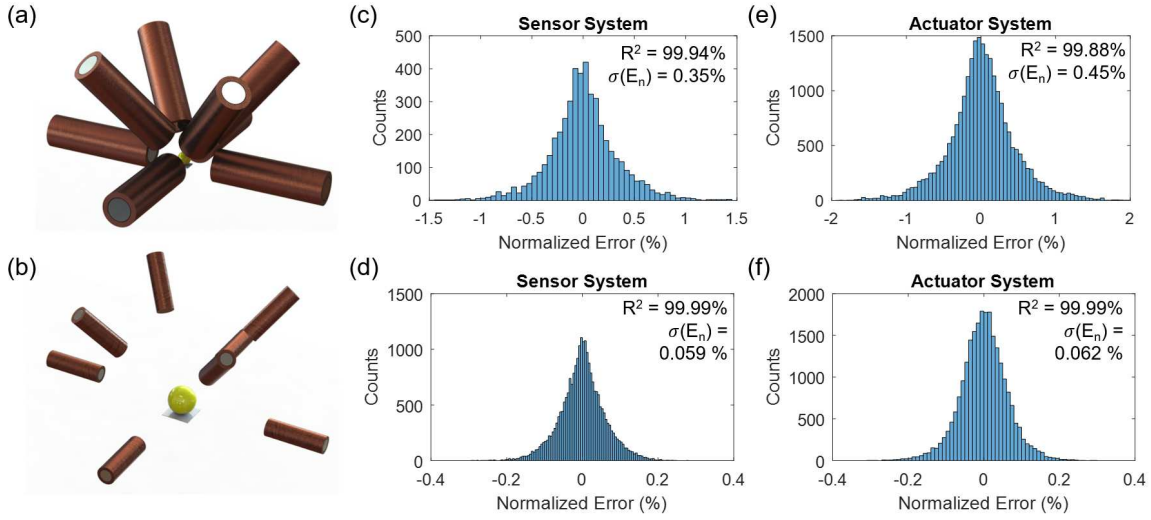


Figure 3.3: Simulation results. (a), (b) Rendered images of configurations of OctoMag and large-scale Octomag. Red hollow cylinders: coils. Grey metallic cylinders: cores. Yellow sphere: a workspace. Grey plate below the workspace: a sensor array. (c)-(f) Normalized error distributions after the calibration (total sample counts are 24,000 for both cases). The STD of the normalized errors were less than 0.45% in all cases. The sensor and actuation systems' coefficients of determination (R^2 values) were over 99.88 % in all cases.

Figure 3.3 shows the simulation result. After the calibration, the sensor and actuation model had shown low normalized errors. STD of the normalized error of the sensor and actuation systems were 0.35%, 0.45% for OctoMag system, respectively, and 0.059% and 0.062% for the large-scale OctoMag system, respectively¹. The determinant of coefficient (R^2 value) for all

¹The sensor noise floors normalized by the range of the applied field were 0.008% and 0.025% for OctoMag and the large scale OctoMag system, respectively.

cases were over 99.88%.

3.4 Experimental Results

3.4.1 Experimental Setup and Procedure

The proposed method was applied to a custom-designed magnetic localization and actuation system (Fig. 3.1). The system consists of nine electromagnets and sixty-four triaxial magnetic sensors located on an 8×8 grid with 30 mm nodal distance. The sensor array was placed 250 mm above the central electromagnet in z -direction and their centers were aligned on the xy -plane. The system specifications are shown in Table 3.2.

Table 3.2: Specification of the Localization and Actuation Setup

	Value
Magnetic sensor	LIS3MDL, STMicroelectronics
- Nodal distance	30 mm
- Sensitivity	17.11 bit/ μ T (digital)
- RMS Noise	0.32 μ T (x -, y -axis), 0.41 μ T (z -axis)
Current sensor	Current sensor of ESCON 70/10, Maxon Motor
- Sensitivity	1 V/A
- Noise	0.735 mA
Soft-iron core	Permenorm 5000 H2, VACUUMSCHMELZE
- Material	Ni-Fe
- Dimension	$\phi 36 \times 160$ mm ³
Copper-wire coil	ENOFLEX-180 ($\phi 1.18$ mm), HELCA Metal
- Dimension	($\phi 40$ (in)-100(out)) $\times 80$ mm, 1500 turns
Reference magnet	NdFeB N42
- Dimensions	$\phi 10 \times 10$ mm ³
- Magnetic moment	0.836 A \cdot m ²
Current driver (ESCON 70/10, Maxon Motor)	

Manufacturing errors are present in both the localization and actuation systems. The sensor system involves errors from the orientation, and sensitivity of each sensor. The electromagnet contains a position shift due to the mutual inductance, and a model error from the magnetic moment mapping. All of these design parameters and manufacturing tolerances are shown in

Table 3.3. Note that the initial parameters define the initial conditions, and tolerances define the boundary conditions for the numerical solver.

Before the calibration procedure, the DC magnetic field around the system and the current sensor offset are nullified. The sensor system's values are measured for a period of time (20 sec) and their mean values are set as nullifying offsets. The magnetic field noise floor was 50 μT , and current sensor offset was $\pm 5 \text{ mA}$.

In the experiment, the electromagnet generated five-hundred random magnetic fields ($L = 500$) from current inputs ranging in $[-3, 3] \text{ A}$. The currents were measured by the current sensors while the magnetic field was measured by each magnetic sensor independently. After the measurements, the magnetic field of the reference magnet was measured inside the workspace in an arbitrary orientation and position. All the measurement data were fed into (3.6), and the optimization task was solved by the interior-point algorithm. The data measurements and the optimization took three minutes and fifteen minutes², respectively. After the optimization, the parameters were re-corrected to fix the gauge freedom using (3.9) and (3.10).

3.4.2 Magnetic Sensor System Calibration Result

The sensor measurement was compared with the ground-truth data. A triaxial Gauss meter (460-010, Lake Shore co.) was used for the ground-truth data measurement. To generate mag-

²A dual-core CPU (Intel Xeon E5-1650, 3.5 Ghz) was used.

Table 3.3: Initial Parameters and Tolerances

Parameters	Initial Value and Tolerance
\mathbf{r}_j	$\mathbf{r}_{j,\text{ideal}}^* \pm 40 \text{ mm}$
G_i	$58 \times \mathbb{I} \pm 5.8 \text{ nT/bit}$
H_i	$\mathbb{O} \pm 5.8 \text{ nT/bit}^2$
\mathbf{m}_j	$\mathbf{m}_{j,\text{ideal}}^* \pm 40 \text{ A}\cdot\text{m}^2/\text{A}$

\mathbb{I} and \mathbb{O} are an identity matrix and a zero matrix in \mathbb{R}^3 , respectively

* $\mathbf{r}_{i,\text{ideal}}$, $\mathbf{m}_{j,\text{ideal}}$ are designed position values of each sensor and actuator.

netic fields to be measured, a set of random current inputs ran in the coils. The random current inputs were generated using a uniform distribution within $[-1, 1]$ A. The input currents should be within a proper range, such that the magnitude of the magnetic field is linear to the input currents and the magnetic field does not saturate the magnetic sensors. The magnetic field was measured first by the sensor array. After that, the Gauss meter measured the magnetic field at the same location of each sensor with the same current input. In total, 1,350 data points were measured for both the sensor array and the Gauss meter.

As a reference method, we applied the calibration method from Plotkin *et al.*[69] to the sensor system calibration. The method uses a permanent magnet to calibrate a magnetic sensor system. The method is modified to calibrate triaxial magnetic sensors, whereas the original method is for single axis magnetic sensors. $\phi 6 \times 6 \text{ mm}^3$ NdFeB N52 magnet was used as the calibration source. The magnet was placed in hundred different locations and its magnetic field was measured by the sensor array.

Figure 3.4(a) shows the sensor system calibration result. Using the proposed method, the sensor model had R^2 value of 99.84%, and the normalized error STD of 0.59 %. The calibration result from the reference method[69] resulted in R^2 value of 99.57% and normalized error STD of 0.97%. The result shows that the proposed method is comparable with the previous sensor system calibration method.

3.4.3 Actuation System Calibration Result

The actuation system was calibrated simultaneously by the proposed method. To validate the calibration results, we compared the modeled magnetic field from (3.4) with the measured magnetic field using the Gauss meter. The input currents for the electromagnet were generated randomly within $[-1, 1]$ A using a uniform distribution. The errors were calculated by the difference between the measured magnetic field and the modeled magnetic field. The Gauss meter was placed in a $50 \times 50 \times 50 \text{ mm}^3$ cubic grid which fit into the workspace. In total, 1,350

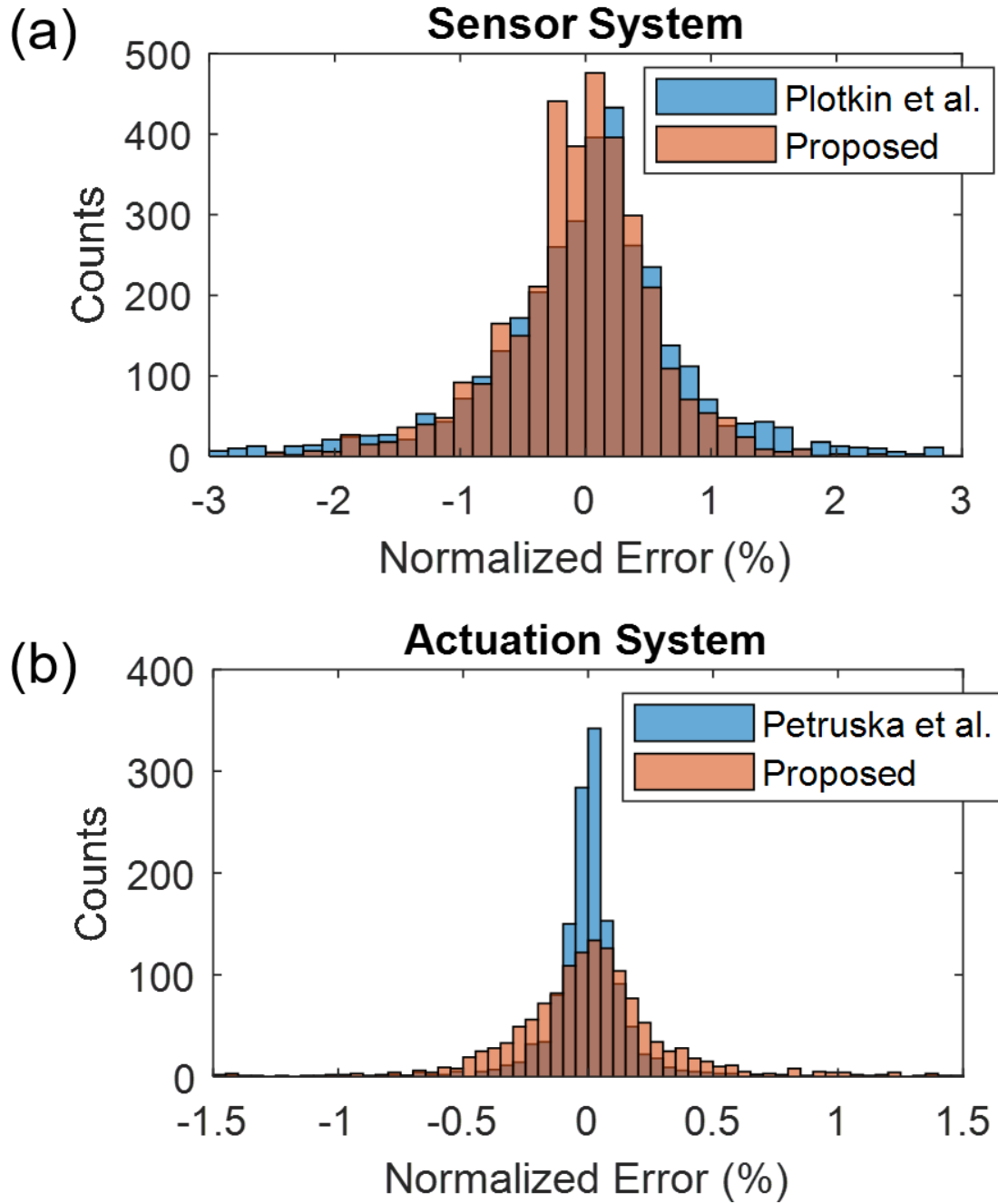


Figure 3.4: Experimental calibration results. (a) Sensor system calibration result ($n = 1350$). The method from Plotkin *et al.*[69] showed R^2 value of 99.57% with 0.97 % standard deviation of the normalized error. Our method showed R^2 value of 99.84 % with 0.59 % standard deviation of the normalized error. (b) Actuation system calibration result ($n = 1350$). The method from Petruska *et al.*[71] showed R^2 value of 99.91% with 0.19 % STD of the normalized errors. Our method showed R^2 value of 99.45 % with 0.47 % STD of the normalized errors.

data points were measured and compared.

The result of the proposed method is compared with the result from the method of Petruska *et al.*[71] as a reference. To collect the data for the reference method, the Gauss meter measured B-field directly inside the workspace when each coil ran $[-3, 0, 3]$ A. These data were fit into spherical harmonics model with one B-coefficient for each magnetic source.

Figure 3.4(b) shows the experimental results. The proposed method resulted in the actuation model with R^2 value of 99.45% and the normalized error STD of 0.47 %. The calibration method from[71] resulted in R^2 value of 99.91 % and normalized error STD of 0.19%. The result shows that the proposed method is comparable with the previous actuation system calibration method.

3.5 Discussion

3.5.1 Actuator Model's Complexity and Accuracy

More complex models, such as multipole expansion models using spherical harmonics[71], for actuators could also be potentially used in our simultaneous calibration method. We used a magnetic dipole field model in this paper because the model is computationally tractable and yields accurate results in the tested systems. For these systems, a more complex model may improve the actuator calibration accuracy but will increase the computational costs and may result in over-fitting.

We compared the model fitting accuracy when using different actuator models, in terms of the number and order of the magnetic poles by varying the size of the workspace and the distance from magnetic sources to the workspace. We conducted a set of control experiments in a simulated environment using finite-element-analysis (FEA). Figure 3.5(a) shows the simulated configuration where a coil with a core is placed near to another core. We varied the workspace dimensions, the bounding sphere radius r_w , and the distance between the center of the coil and

the center of the workspace, d , and obtained the magnetic field data from FEA when a unit-current flows through the coil. The magnetic field data were fitted with actuation models using the method from [71].

Figure 3.5 shows the result of the actuation model fitting. In Fig. 3.5(b), the general trend shows all multi-pole models work better when increasing the distance between the workspace and the magnetic sources. With a fixed number of magnetic sources (three sources), even the dipole model yields STD value less than 1% in all ranges. Fig. 3.5(c-d) show the accuracy of the model when the size and position of the workspace is fixed ($r_w/d_c=0.375$ and $d/d_c=1.75$). In Fig. 3.5(c), with a fixed number of sources (three sources), by increasing the order of the poles, the accuracy of the model is improved. In Fig. 3.5(d), the actuation model improves with an increased the number of sources. In all cases, the simplest model (with a single dipole) fits the B-field in the workspace less than 1% STD of the normalized errors.

3.5.2 Placement of the Sensor Array

The sensor array placement might affect the accuracy of the calibration result. If the sensor array is too far away from the workspace, then the sensor array could not observe the magnetic field around the workspace. In such a case, the actuation model on the sensor array is accurate, but might not in the workspace. To achieve the best result, it is preferred to place the sensor array inside the workspace. Then the magnetic field observed in the sensor array closely matches with the magnetic field of the workspace.

The sensor array could be placed near by the workspace as well. This is important for the applications where it is hard to place the sensor array inside the workspace due to mechanical constraints. Additionally, a system needs to be automated and calibrated regularly would be one of the applications. In such a case, it is recommended to place the sensor array as close as possible to the workspace, so that the B-field on the sensors are close to the B-field of the workspace. Note that the simulations and experiments were conducted to simulate those cases

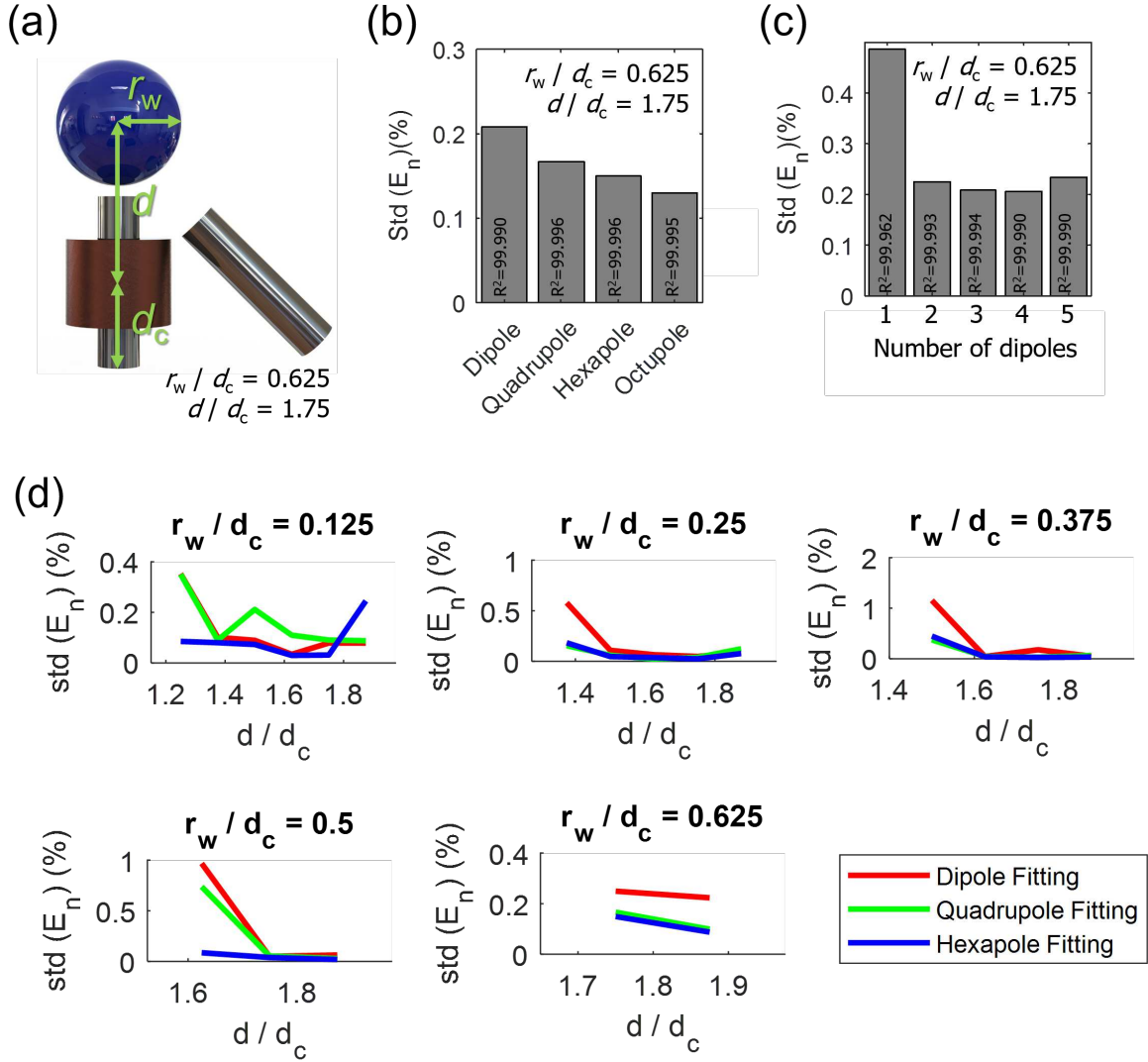


Figure 3.5: Comparison of model fitting accuracy using different actuation models. (a) Experimental setup for FEA. A coil with a core and an extra core are used. The workspace is a blue sphere with a radius, r_w , and is placed above the closest coil with a center-to-center distance, d . The length of the cores is d_c . (b) Actuation model fitting results using a dipole model together with up to different orders of multi-pole models. Note that for each coil or core, three sources of each order of dipole or multipole models are applied in the actuation model fitting. (c) Actuation model fitting results using different number of dipole sources. (d) Actuation model fitting results using different orders of actuation models by varying the workspace's range and distance. For each workspace configuration, three dipoles, three dipoles with three quadrupoles, and three dipoles with three quadrupoles and three hexapoles are used.

where the sensor array is near to the workspace.

3.5.3 Applications of the Method

There are two major applications of the proposed method. First, the method could be employed for an automatic calibration with the least amount of human labor. This would be beneficial for a system which needs recalibration often. For example, magnetic sensors require gain updates due to their time-variant soft-iron effect [81] or a long-term gain-offset drift from the environmental change, such as the Earth's magnetic field change. Depending on the time scale of the gain change of the system or environment, the update can be scheduled regularly. A user could expose the reference magnet to the sensor system before the calibration, and the rest of the calibration could be done automatically.

Second, the proposed method allows the automatic calibration for reconfigurable magnetic sensing and actuation systems. The reconfiguration may be beneficial for improving dexterity, energy efficiency, or avoiding singularities of an actuation system. Especially, the reconfiguration of the system would be critical in medical robotics, because a treatment of a patient might have a preferred direction. In the case of the reconfiguration, the parameter space could be minimized including only the actuation parameters enabling *in-situ* calibration.

3.5.4 Limitations

The method is limited to solenoidal magnetic actuation and sensing systems. The original method applies when the dipole magnetic field dominates and the sensor array is close to the workspace. The method could be expanded to multi-pole actuation systems. All of these magnetic fields could be regarded as diverging magnetic fields toward the center of the source. The method's fundamental limitation is that the method cannot be applied to non-diverging magnetic field generator towards the center of the actuator, such as Helmholtz coil systems[64]. To calibrate such a system, a method with the spherical multi-pole B-field expansion model [71]

should be utilized. In this case, the calibration is limited only for the actuation system assuming that the sensor system is calibrated beforehand. The sensor system must be placed inside the workspace during the calibration to expose the sensor system to the near-ranged magnetic field and removed afterwards.

3.6 Conclusion and Future Work

A simultaneous calibration method for a magnetic localization and actuation system is proposed. Uncalibrated electromagnets are used as calibration sources based on the magnetic dipole model. By utilizing the ability of the electromagnet that generates various magnetic fields at a fixed position, a system of equations is constructed and solved automatically based on a bundle adjustment framework. Both simulation and experimental calibration results demonstrate the effectiveness of the proposed calibration method. The proposed method would be utilized for the calibration of a reconfigurable electromagnetic actuation and localization systems for bio-medical applications as future work.

Chapter 4

Control of Magnetically Actuated Soft Capsule Endoscope

4.1 Introduction

Main tasks of a MASCE (hereafter referred to as “the robot”) are a visual endoscopy and a medical function, such as biopsy or drug release. In this chapter we assume that the function is biopsy. The details of the implementation of the biopsy function using the MASCE platform is explained in Chapter 5. For the visual endoscopy and the biopsy, the robot performs various motions (Fig. 4.1). For the visual endoscopy, the robot navigates inside a stomach using rolling locomotion and observes the stomach wall with the orientation control (Fig. 4.1A). For the biopsy, the robot anchors on a tumor (Fig. 4.1B) and inserts the biopsy needle using the collapse motion (Fig. 4.1C). Note that the orientation control on a flat surface is different than the orientation control on a tumor, as the concave shape of the tumor makes the robot to roll-off downward the tumor without a special control.

In this chapter, we introduce the magnetic energy well for the control of the MASCE. Berge-man *et al.* introduced the magnetic energy well for trapping neutral atoms in 3-D space in an open-loop manner [82]. In this concept, the lowest magnetic energy is spatially placed in a

desired position to trap the atoms. However, this is only possible with diamagnetic materials, which have negative magnetic moments in 3-D space. Earnshaw's theorem forbids magnetic trapping for positive magnetic moments in 3-D space, which is our case.

Although the magnet of the robot has the positive magnetic moment in our application, it is found that we could exploit the magnetic energy well when we reduce the space into 2-D Cartesian space associated with 2-D orientation space. This is only possible if the magnet is supported by a surface (thus, the space dimension is reduced) as like our robot is on the stomach wall. We utilized this property and created magnetic energy wells for controlling the three motions (Fig. 4.1D to L). This open-loop energy based controller is closed by a high level proportional-integral(PI) controller using feedback.

4.2 Magnetic Actuation Background

4.2.1 Magnetic Field Models

In this chapter, we assume that the magnetic field inside the workspace is non-uniform and is dominated by magnetic dipoles. This assumption is along with the actuation model from Chapter 3. Additionally, we assume that the robot has a magnetic dipole, which is controlled by the magnetic field. In short, the magnetic dipole moment inside the robot is actuated by the multiple of dipole dominant external magnetic field.

Let us start with the magnetic interaction of a magnetic dipole inside the magnetic field. The magnetic scalar potential energy of a magnetic dipole is defined as

$$E_{p,m} = -M\hat{\mathbf{n}} \cdot \mathbf{b} \quad (4.1)$$

where M is the magnetic dipole moment magnitude, $\hat{\mathbf{n}} \in \mathbb{S}^2$ is an orientation unit vector of the dipole, and $\mathbf{b} \in \mathbb{R}^3$ is the external magnetic field. Here \mathbb{S}^2 is the 2-sphere manifold for

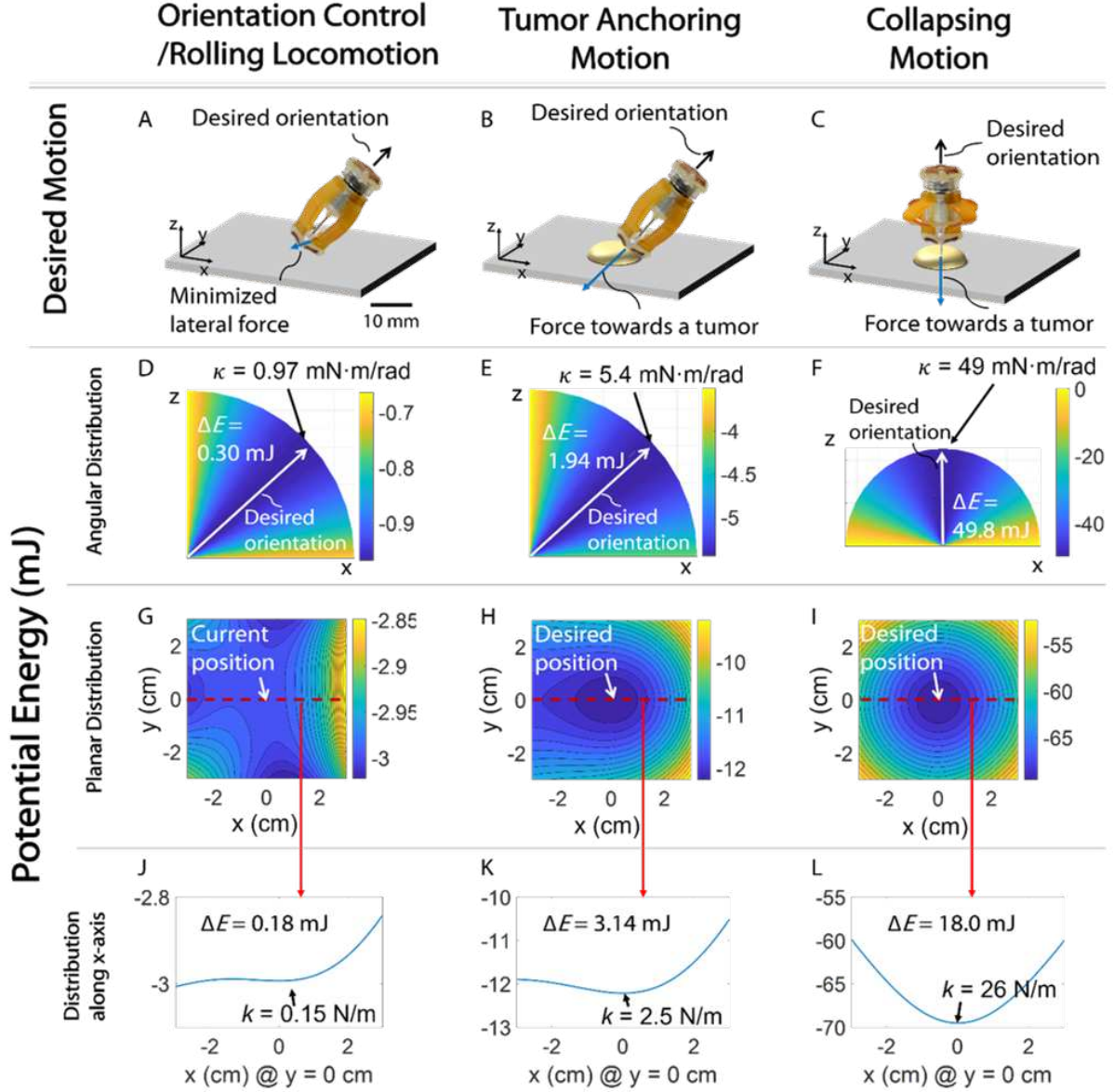


Figure 4.1: Simulated energy distributions for different controlled motions. (A to C) The desired motions for orientation control/rolling locomotion, tumor anchoring motion, and collapsing motion. (D to E) Simulated magnetic energy distributions with respect to the robot's orientations (y -axis). The desired angles lie on the lowest potential energy in each mode. ΔE denotes the depth of the potential energy. (G to i) Simulated magnetic energy distributions with respect to the robot's 2-D position (x - and y -axes) are shown. The local minimum of each potential energy is placed at either the current position or desired position. (J to K) The x -directional profiles of the potential energies are shown. The desired positions are placed at the each local minimum. The depths of the potential energy well, ΔE , are different for different motion types. The simulated spring constant, k , indicates how strongly the magnetic energy well attracts the robot to the center of the magnetic energy well.

indicating the orientation.

The magnetic force and torque are derived from the energy by taking the negatives of the gradients. First, the spatial gradient in the 3-D Cartesian coordinate of the potential energy yields the magnetic force

$$\mathbf{f} = -\nabla_{\mathbf{r}}(E_{p,m}) = (M\hat{\mathbf{n}} \cdot \nabla_{\mathbf{r}})\mathbf{b} = M \left(\frac{\partial \mathbf{b}}{\partial x} \frac{\partial \mathbf{b}}{\partial y} \frac{\partial \mathbf{b}}{\partial z} \right)^{\top} \hat{\mathbf{n}} \quad (4.2)$$

where $\nabla_{\mathbf{r}}(\cdot)$ is the gradient in the 3-D Cartesian coordinate. The negative of the gradient of the magnetic potential energy in \mathbb{S}^2 yields the magnetic torque

$$\boldsymbol{\tau} = -\nabla_{\hat{\mathbf{n}}}(E_{p,m}) = M\hat{\mathbf{n}} \times \mathbf{b}. \quad (4.3)$$

where $\nabla_{\hat{\mathbf{n}}}(\cdot)$ is the gradient on \mathbb{S}^2 .

We can further calculate the hessian of the magnetic potential energy, which is useful to calculate the curvature of the magnetic energy well. We use only x -, y -directional differentiation for the Cartesian coordinate assuming that the stomach surface is laid on the xy -plane. The hessian of the magnetic dipole potential energy is equal to

$$\mathbf{H} = M \begin{bmatrix} \mathbf{H}_{11} & \mathbf{h}_{12} & \mathbf{h}_{13} \\ \mathbf{h}_{21} & H_{12} & H_{23} \\ \mathbf{h}_{31} & H_{32} & H_{33} \end{bmatrix} \quad (4.4)$$

where

$$\begin{aligned}
\mathbf{H}_{11} &= (\hat{\mathbf{n}} \cdot \mathbf{b})\mathbb{I} - \mathbf{n} \otimes \mathbf{b} \in \mathbb{R}^{3 \times 3} \\
\mathbf{h}_{12} &= \mathbf{h}_{21}^T = -\hat{\mathbf{n}} \times \frac{\partial \mathbf{b}}{\partial x} \in \mathbb{R}^{3 \times 1} \\
\mathbf{h}_{13} &= \mathbf{h}_{31}^T = -\hat{\mathbf{n}} \times \frac{\partial \mathbf{b}}{\partial y} \in \mathbb{R}^{3 \times 1} \\
H_{22} &= -\hat{\mathbf{n}} \cdot \frac{\partial^2 \mathbf{b}}{\partial x^2} \\
H_{23} &= H_{32} = -\hat{\mathbf{n}} \cdot \frac{\partial^2 \mathbf{b}}{\partial x \partial y} \\
H_{33} &= -\hat{\mathbf{n}} \cdot \frac{\partial^2 \mathbf{b}}{\partial y^2}
\end{aligned}$$

where \mathbb{I} is the identity matrix.

To generate those values, such as the force, torque, or a specific curvature of the magnetic energy well, we need to use the external magnetic actuation. After the calibration procedure introduced in Chapter 3, we can find a magnetic field map as

$$\mathbf{b} = \mathbb{B}(\mathbf{r})\mathbf{i} \quad (4.5)$$

where $\mathbf{b} \in \mathbb{R}^3$ is the magnetic field generated by the coils at a position $\mathbf{r} \in \mathbb{R}^3$, $\mathbb{B}(\cdot) \in \mathbb{R}^{3 \times 9}$ is the magnetic field mapping matrix with 9 current inputs, $\mathbf{i} \in \mathbb{R}^9$ is electric current inputs in each coil. Here, \mathbf{b} could be used directly for the torque control as in Eq. 4.3.

A calculation of the gradient of B-field is required for the force calculation. By taking a gradient of (4.5) in the 3-D Cartesian coordinate system and arranging it into a 9×9 matrix, we find the magnetic field gradient map as

$$\mathbf{h} = \begin{bmatrix} \partial \mathbb{B}(\mathbf{r}) / \partial x \\ \partial \mathbb{B}(\mathbf{r}) / \partial y \\ \partial \mathbb{B}(\mathbf{r}) / \partial z \end{bmatrix} \mathbf{i} = \mathbb{G}(\mathbf{r})\mathbf{i} \quad (4.6)$$

where $\mathbf{h} = (\frac{\partial \mathbf{b}^\top}{\partial x} \quad \frac{\partial \mathbf{b}^\top}{\partial y} \quad \frac{\partial \mathbf{b}^\top}{\partial z})^\top \in \mathbb{R}^9$ is the magnetic field gradient expressed in a vector form, $\mathbb{G}(\cdot) \in \mathbb{R}^{9 \times 9}$ is the magnetic gradient actuation map. Further, utilizing this form, we get the force map as

$$\mathbf{f} = M \begin{bmatrix} \hat{\mathbf{n}}^\top & \mathbf{0} & \mathbf{0} \\ \mathbf{0} & \hat{\mathbf{n}}^\top & \mathbf{0} \\ \mathbf{0} & \mathbf{0} & \hat{\mathbf{n}}^\top \end{bmatrix} \mathbb{G}(\mathbf{r})\mathbf{i} = \mathbb{F}(\mathbf{r}, \hat{\mathbf{n}}, M)\mathbf{i} \quad (4.7)$$

where $\mathbb{F}(\cdot) \in \mathbb{R}^{3 \times 9}$ is the force mapping matrix.

4.2.2 System Dynamics

The robot on a surface could be modeled as an inverted pendulum (Fig. 4.2). The robot has a pivot point on the surface and the center of the mass is located at the end the moment arm. The pendulum is actuated by the magnetic force and torque. Additionally, we need to consider the dynamics from the magnetic actuation system (coil system). As the actuation system described in Chapter 3 requires very strong magnetic field and its gradient, the coils are with high numbers of turns. This results in a strong magnetic field with low electric current inputs, but sacrifices the system's bandwidth. The measured settling time of a coil with the presence of a magnetic core was 0.1 second. Thus, we consider the coil system's dynamics by modeling it as a RL circuit first order dynamics.

The system dynamics is expressed as

$$\begin{aligned} \dot{\hat{\mathbf{n}}} &= \mathbf{w} \times \hat{\mathbf{n}} \\ (I_{xx}\dot{\mathbf{w}}) &= M\hat{\mathbf{n}} \times \mathbf{b} + (L\hat{\mathbf{n}}) \times (m\mathbf{g}) + (L\hat{\mathbf{n}}) \times \mathbf{f} \\ \dot{\mathbf{i}} &= -A\mathbf{i} + A\mathbf{u} \end{aligned} \quad (4.8)$$

where $\hat{\mathbf{n}} \in \mathbb{S}^2$ is the unit vector orienting the heading of the robot, $(\dot{\cdot})$ indicates time derivatives, $\mathbf{w} \in \mathbb{R}^3$ is the angular velocity, I_{xx} is the moment of inertia of the robot in the long axis direction

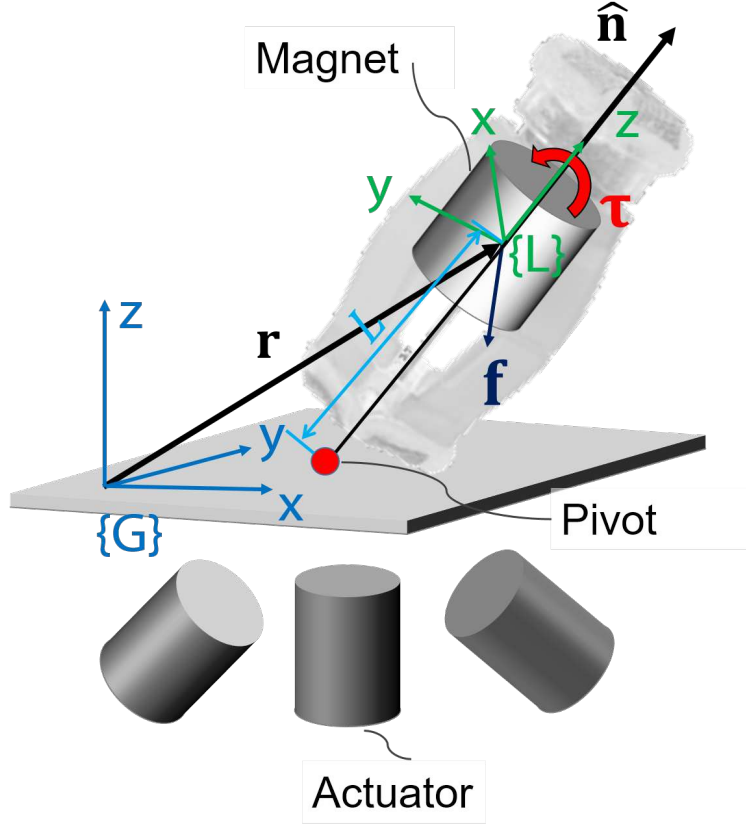


Figure 4.2: System dynamics and a local coordinate definition. The inverted pendulum is employed to express the system dynamics of the capsule robot.

at the pivot¹, M is the magnetic moment of the magnet inside the capsule, L is the distance from the pivot to the center of the mass, $\mathbf{g} \in \mathbb{R}^3$ is the gravitational acceleration, $A \in \mathbb{R}^{9 \times 9}$ is the diagonal matrix of the exponential decay constant of the electromagnetic coils, and $\mathbf{u} \in \mathbb{R}^9$ is the command input for electric current. Note that \mathbf{b} and \mathbf{f} are from Eq. (4.5, 4.2) where the electric current dynamics is connected with the inverted pendulum dynamics.

4.2.3 Local Coordinate Definition

It is useful to attach a local coordinate for an efficient calculation of the magnetic field or force on the robot. For example, if we want to apply the magnetic force as the same direction of

¹The other moments of inertia are neglected.

the axis of the robot for the robot collapse, we can control the force along the axis, and remove the values in the other axes to zero.

The local coordinate is attached at the center of the mass of the robot, and its z -axis is aligned with the magnetic axis (Fig. 4.2). In this case, the pose of $\{L\}$ could be defined based on $\hat{\mathbf{n}}$. The pose difference could be expressed in axis-angle representation. The axis is calculated as

$$\boldsymbol{\zeta} = \hat{\mathbf{n}} \times \hat{\mathbf{z}}_{\{G\}} \quad (4.9)$$

where $\boldsymbol{\zeta} \in \mathbb{R}^3$ and $\hat{\mathbf{z}}_{\{G\}}$ is the z -axis of the global coordinate. $\hat{\mathbf{z}}_{\{G\}}$ could be simply substituted by $(0, 0, 1)$. Here the angle between two axes could be calculated as $\theta = \sin^{-1}(\|\boldsymbol{\zeta}\|_2)$, and the orientation axis could be redefined as a unit vector, $\hat{\boldsymbol{\zeta}} = \boldsymbol{\zeta}/\|\boldsymbol{\zeta}\|_2$ when $\|\boldsymbol{\zeta}\|_2$ is not zero. Then the rotation matrix can be formulated as

$$\mathbf{R} = e^{\theta[\hat{\boldsymbol{\zeta}}]_{\times}} \quad (4.10)$$

where $e^{(\cdot)}$ is the matrix exponential operator and $[\cdot]_{\times}$ is a skew symmetric matrix operator. When $\|\boldsymbol{\zeta}\|_2$ is zero, the rotation matrix is simply the 3×3 identity matrix. The rotation matrix, \mathbf{R} , describes the pose of $\{G\}$ seen by $\{L\}$, which would be used to transform the B-field and forces seen in $\{L\}$. The magnetic field seen by $\{L\}$ is

$$\mathbf{b}_{\{L\}} = \mathbf{R}\mathbf{b}_{\{G\}} \quad (4.11)$$

where $\mathbf{b}_{\{G\}}$ is the B-field seen by $\{G\}$. The force seen by the local coordinate is described as

$$\mathbf{f}_{\{L\}} = \mathbf{R}\mathbf{f}_{\{G\}} \quad (4.12)$$

where $\mathbf{f}_{\{G\}}$ is the force seen by $\{G\}$.

4.3 Controls

The capsule robot is actuated by the non-uniform magnetic field. As we discussed in the system dynamics, the actuation system is slow (0.1 second settling time). Relatively, the system dynamics of the robot is fast due to the low mass (10 gram) and the low moment of inertia ($22.5 \text{ g}\cdot\text{cm}^2$). The inverted pendulum's time constant is 0.04 second. To overcome this challenge, we utilized the magnetic energy well for controlling the robot which showed open-loop stable behaviors, and further the open-loop is closed by a hierarchical PI controller. We derive specific controllers for each motion shown in Fig. 4.1.

4.3.1 Orientation Control and Rolling Locomotion

The orientation controller is constructed as an hierarchical manner. The low level controller utilizes the magnetic energy well to control the orientation, and the high level controller closes the loop to clear error offsets or to reject disturbances. We explain the low-level controller first and the high-level controller at the end of this section.

The robot's motion is controlled by applying a specific magnetic field and its gradient. The robot balances the torque from the gravitational force and the magnetic torque, so that resultant orientation is the desired orientation. More precisely, the desired orientation is at the lowest energy of the sum of the gravitational potential energy and the magnetic potential energy (Fig. 4.1D). Not only for the magnetic torques, but also the magnetic force needs to be considered. A weak magnetic energy well (Fig. 4.1G, J. Please compare with the other locomotion's magnetic energy well depth, ΔE , and its spring constant to attract the robot to the center of the magnetic energy well, k) in 2-D plane is created to stabilize the robot's position. In such a case, the robot is not trapped by the magnetic energy well or pushed away by the inverted magnetic energy well in 2-D. The rolling locomotion is an extension of the orientation control. By rotating the desired orientation of the capsule, the robot rolls on a surface of the stomach. The rolling locomotion translates the robot like a wheel.

In this concept, it is easy to solve the problem when we separate the gravitational terms from the magnetic terms. The gravity cancellation B-field is calculated as

$$\hat{\mathbf{n}}L \times m\mathbf{g} + M\hat{\mathbf{n}} \times \mathbf{b}_c = 0 \rightarrow \mathbf{b}_c = -m\mathbf{g}/M \quad (4.13)$$

where \mathbf{b}_c is the B-field which cancels the gravity for the inverted pendulum model of the robot. \mathbf{b}_c would be superposed to the B-field for controlling the angle of the robot. Note that the gravity cancellation does not require feedback control.

By separating the effect of the gravity, the B-field which regulates the orientation of the capsule could be simply the B-field with the same direction as the desired orientation. Then the B-field for the orientation regulation is

$$\mathbf{b}_o = c\hat{\mathbf{n}}_d \quad (4.14)$$

where c is an adjustable gain value and $\hat{\mathbf{n}}_d \in \mathbb{S}^2$ is the desired orientation of the robot.

The force in x -, y -direction is set to zero to stabilize the robot at the current position. The depth of the magnetic energy well is set to be the minimum, as creating a strong magnetic energy well always try to attract the capsule to the current point and disturbs moving towards the other direction. The input currents are bounded by the system capability (e.g., the capability of the electric current driver or power supply), and also the magnetic field from the actuator on the magnetic sensor should be less than the saturation limit of the magnetic sensors for the

localization. Above criteria could be formulated as an online optimization problem as

$$\begin{aligned}
& \underset{\mathbf{i}}{\text{minimize}} && \alpha \|\mathbf{i}\| + \beta \Sigma \\
& \text{subject to} && \mathbf{b} = \mathbf{b}_c + \mathbf{b}_o \\
& && \mathbf{f}_{x,y} = \mathbf{0} \\
& && -\boldsymbol{\epsilon} < \mathbf{h} < \boldsymbol{\epsilon} \\
& && -\mathbf{b}_{\text{sat}} \preceq \mathbf{b}(\mathbf{r}_{s,i}) \preceq \mathbf{b}_{\text{sat}} \\
& && -\mathbf{i}_m \preceq \mathbf{i} \preceq \mathbf{i}_m
\end{aligned} \tag{4.15}$$

where $\mathbf{i} \in \mathbb{R}^9$ is the electric currents running in the coils as optimization parameters, α and β are the tunable gain between two optimization criteria (minimization of the current input and minimization of the energy well curvature), \mathbf{b} is the desired B-field from Eq. (4.5), $\mathbf{f}_{x,y} \in \mathbb{R}^2$ is the x -, y -components of the magnetic force from Eq. (4.2), $\boldsymbol{\epsilon}$ is the boundary for the magnetic gradient², \mathbf{h} is the magnetic field gradient values from Eq. (4.6), \mathbf{b}_{sat} is the saturation limit of the magnetic sensor, $\mathbf{b}(\mathbf{r}_{s,i})$ is the magnetic field calculated on the i -th sensor's position, $\mathbf{r}_{s,i}$, \preceq is the element-wise inequality, and \mathbf{i}_m is the maximum current for the current driving system. Here, Σ is the maximum absolute curvature of the magnetic energy well. This value is calculated as

$$\Sigma = \max(\text{svd}(H(E_{p,m}))) \tag{4.16}$$

where $H(\cdot)$ is the hessian from Eq. (4.4), $\text{svd}(\cdot)$ is an operator to calculate the scalar matrix of singular value decomposition.

The open-loop controller is closed by the high level PI-controller. The controller generates output which becomes the control input for the open-loop controller, $\hat{\mathbf{n}}_d$. As the control input, $\hat{\mathbf{n}}_d$, lies in the \mathbb{S}^2 manifold, we define the orientation error as how much rotation is required to the reference orientation. In such a case, it is convenient to express the rotations in $\text{so}(3)$,

²This value is a term to make the controller robust, when $\mathbf{f}_{x,y}$ is not reliable due to unexpected localization failures

which is the Lie Algebra of the rotation group, $SO(3)$, or more compactly using the axis-angle representation. A vector in the axis-angle representation could be mapped to $so(3)$ by a skew symmetric matrix. We use these rather than $SO(3)$ itself because they lie in the linear space, thus the sum of the rotation error could be defined in a linear manner. The error between the reference orientation, $\mathbf{n}_{\text{ref}} \in \mathbb{S}^2$, and the current orientation, $\hat{\mathbf{n}}$, is defined as a cross product of those two values as

$$\mathbf{e} = \hat{\mathbf{n}} \times \hat{\mathbf{n}}_{\text{ref}}. \quad (4.17)$$

This implies how much rotation we miss to the reference orientation from the current orientation in the axis-angle representation. Then the PI control input could be defined as

$$\mathbf{u}_{\text{pi}} = K_p \mathbf{e} + K_i \int \mathbf{e} dt \quad (4.18)$$

where K_p is the proportional gain and K_i is the integral gain. As the maximum magnetic torque applies when the magnetic moment and the magnetic field are perpendicular, we can saturate the size of the PI control input as $\pi/2$. This could be done by limiting the maximum size of the \mathbf{u}_{pi} as

$$\|\mathbf{u}_{\text{pi}}\|_2 = \pi/2 \quad \text{if} \quad \|\mathbf{u}_{\text{pi}}\|_2 \geq \pi/2. \quad (4.19)$$

Finally, the PI control gain, \mathbf{u}_{pi} , could be transformed into a 3-D rotation, which belong to $SO(3)$, as

$$\mathbf{R}_{\text{gain}} = e^{[\mathbf{u}_{\text{pi}}]_{\times}} \in SO(3) \quad (4.20)$$

where $e^{(\cdot)}$ is the matrix exponential map and $[\cdot]_{\times}$ is the skew-symmetric matrix operator. Then the final control input in the high level controller forms as

$$\hat{\mathbf{n}}_{\text{d}} = \mathbf{R}_{\text{gain}} \hat{\mathbf{n}}_{\text{ref}}. \quad (4.21)$$

This value $\hat{\mathbf{n}}_{\text{d}}$ would be plugged into Eq. (4.15) to connect with the low level controller.

4.3.2 Anchored Orientation Control

Anchoring on a tumor requires a different motion (Fig. 4.1B) than the rolling locomotion, because of the mound-like shape of a tumor. The robot can easily roll off the tumor when a downward force, such as the gravity, is applied. This is because the magnetic torque cannot be applied on the same axis as the magnetic moment, where the magnetic torque fails to hold the robot's rotation. This problem is handled by creating a relatively strong magnetic energy well at the center of the tumor (Fig. 4.1H, K; compare with the other locomotion's energy well depths and its spring constants). This attracts the magnet to the desired position with a magnetic force, which compensates the gravity or any other downward force. Note that the magnetic force should not be too strong to collapse the robot in this case. This control is formulated as an online optimization problem.

$$\begin{aligned}
& \underset{\mathbf{i}}{\text{minimize}} && -\min(\text{eig}(H(E_{m,p}))) \\
& \text{subject to} && \mathbf{b} = \mathbf{b}_c + \mathbf{b}_o \\
& && \mathbf{f}_{x,y,\{L\}} = \mathbf{0} \\
& && |f_{z,\{L\}}| < f_{z,\text{th}} \\
& && -\mathbf{h}_{\max} \preceq \mathbf{h} \preceq \mathbf{h}_{\max} \\
& && -\mathbf{i}_m \preceq \mathbf{i} \preceq \mathbf{i}_m
\end{aligned} \tag{4.22}$$

where $\min(\text{eig}(H(-E_{m,p})))$ is the minimum curvature of the magnetic energy well, $\text{eig}(\cdot)$ is the operation to find the eigenvalues of a given matrix, $\mathbf{f}_{x,y,\{L\}} \in \mathbb{R}^2$ and $f_{z,\{L\}}$ are the magnetic force in x -, y - and z -direction in the local coordinate $\{L\}$, respectively, $f_{z,\text{th}}$ is the minimum absolute force to collapse the robot, and \mathbf{h}_{\max} is the magnetic gradient boundary, which is larger than ϵ to create the strong forces toward the tumor.

4.3.3 Collapsing controller

The collapsing motion (Fig. 4.1C) could be used for a medical function, such as biopsy. The motion is driven by applying a strong magnetic gradient to the robot towards the center of the tumor, while keeping the orientation of the capsule by applying a strong magnetic field as the desired orientation to the robot. Because the strong magnetic field is required, it temporarily saturates the magnetic sensor system. Due to the saturation, the robot is controlled in an open-loop manner by creating a strong magnetic energy well at the tumor position (Fig. 4.1I, L). After the robot successfully collapses, the robot could restore the shape by removing the strong magnetic gradient, while keeping the direction of the robot with a static magnetic field.

The collapse controller could be formulated as another online optimization problem. In this problem, we maximize the curvature of the magnetic energy well as well as the downward collapsing force. The problem is expressed as

$$\begin{aligned}
& \underset{\mathbf{i}}{\text{minimize}} && \gamma f_{z,\{L\}} - \delta \min(\text{eig}(H(E_{m,p}))) \\
& \text{subject to} && \mathbf{b}_{x,y,\{L\}} = \mathbf{0} \\
& && \mathbf{f}_{x,y,\{L\}} = \mathbf{0} \\
& && b_{z,\{L\}} > b_{\text{th}} \\
& && f_{\min} < -f_{z,\{L\}} < f_{\max} \\
& && -\mathbf{i}_m \preceq \mathbf{i} \preceq \mathbf{i}_m
\end{aligned} \tag{4.23}$$

where γ and δ are tunable gains between the collapsing magnetic force and the magnetic energy well curvature, $\mathbf{b}_{x,y,\{L\}}$ is the magnetic field in x -, y -direction in $\{L\}$, $b_{z,\{L\}}$ is the magnetic field in z -direction in $\{L\}$, b_{th} is a threshold value to stabilize the robot in the desired orientation, $f_{z,\{L\}}$ is the collapsing force towards the tumor in $\{L\}$, f_{\min} is the minimum force (0.4 N) to collapse the capsule, and f_{\max} is the maximum force (0.8 N) to collapse the capsule. MatLAB codes for all of the controllers above are provided in Appendix G.

4.4 Teleoperation

The robot is manipulated by a custom-designed teleoperation system. The teleoperation system helps a user to manipulate the robot intuitively without having an orientation coordination difficulty. The teleoperation system is composed of a master system and a slave system. The master system is composed of the master capsule robot and a magnetic localization system. The slave system is composed of the slave robot, the magnetic actuation system and the magnetic localization system. The master capsule and the slave capsule are identical, except the fact that the slave capsule might have a functional attachment, such as a needle or a drug chamber. The motions of the master capsule and the slave capsule are synchronized. Therefore, by manually manipulating the master capsule, the slave capsule moves as the same way as the master capsule moves. Figure 4.3 (video is available in supplementary files) shows the synchronized motions of the capsule robots. When a user orients the master robot in a specific direction manually, the orientation of the slave robot is aligned with the orientation of the master capsule. The rolling locomotion can be achieved by rolling the master robot. The collapsing motion is performed in the same manner. By measuring the compression of the master robot using the magnetic localization technique, the collapse of the master robot is detected. The collapse of the master robot triggers the collapse of the slave capsule.

4.5 Conclusion

Orientation control, tumor-anchored orientation control, and collapsing control for the magnetically actuated soft capsule endoscopes are proposed. By utilizing the magnetic energy well, open-loop stable behaviors of the capsule robot are achieved. The controllers are closed using high level proportional integral (PI) controllers to remove the error offset or to reject disturbances. Further, we proposed teleoperation of the capsule robot, and demonstrated the teleoperation by synchronizing the motions of the master and slave capsule robots.

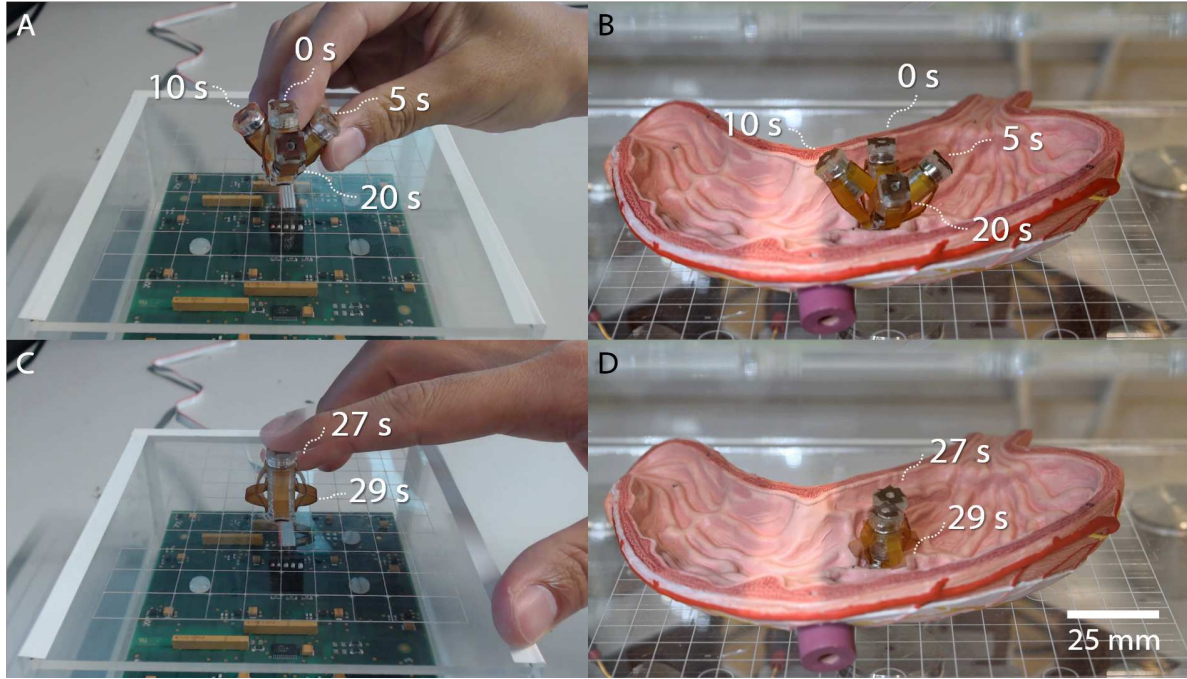


Figure 4.3: Teleoperation of the capsule robot. The images show the snapshots of the teleoperation manipulation of the slave capsule (**B**, **D**) using the master capsule (**A**, **C**). The master capsule is the same capsule as the slave capsule without the needle, which is manually moved and pressed on a smooth acrylic surface. The orientation changes in the master robot (**A**) are used as inputs to the slave robot (**B**), so that the orientation of the slave robot is synchronized with the orientation of the master robot. In the same manner, the compression of the master robot (**C**) is used as an input for the slave robot (**D**), so that the collapsing motions are synchronized. The master capsule's 5-DOF localization and compression are measured by the 8 x 8 magnetic sensor array under the surface (Video is found in Supplementary Information).

Chapter 5

Application: Magnetically Actuated Soft Capsule Endoscope for Fine Needle Biopsy

5.1 Introduction

While capsule endoscopy has already begun to revolutionize the diagnosis of GI disorders in the clinic, the possibilities afforded by capsule endoscopy are still being explored. One of the major limitations of commercially available devices is their inability to take biopsy samples after a suspicious lesion is identified. Acquiring a biopsy currently requires an additional endoscopic procedure, adding to the overall time and expense of making an accurate diagnosis. The ability to take biopsy samples is therefore a highly desirable addition to the feature set of capsule endoscopes [83].

Several capsule designs for taking biopsy samples have already been presented. The idea of taking biopsy samples in the GI tract with a small, swallowable device appeared as early as 1967 when an electromagnetic biopsy device was first presented by Driller and Neumann [84]. The capsule utilizes the peristalsis of the lower GI tract, air pressure through a tether, and an electromagnetically actuated razor inside the robot for cutting tissue. Kong *et al.* developed a rotational micro biopsy device [85, 86], which can cut sample tissues using a rotational razor

inside the capsule, utilizing torsional springs (thermally or SMA triggered). Swain suggested a multiple capsule design in his patent [87], utilizing forceps or cutting razor-style biopsy tools through a narrow hole on the side of the capsule. Park *et al.* proposed a forceps-style biopsy tool actuated by a torsion spring, using a shape-memory alloy trigger [88]. Chen *et al.* suggested a forceps-style biopsy tool which is driven by a coil-based wireless power transfer system with double-balloon-enteroscopy-style locomotion [89]. Simi *et al.* integrated a magnetic torsion spring in a biopsy capsule that enables a blade to cut a tissue when the external magnetic field is removed [90].

Although most of the biopsy capsule designs have been created with lower GI tract applications in mind, it is possible that some of them may additionally work in the upper GI tract. One previous design has been specifically investigated for upper GI tract procedures. Yim *et al.* presented a magnetically actuated soft capsule endoscope (MASCE) with micro-grippers [45]. MASCE carries and deploys thermo-sensitive micro-grippers in the stomach and retrieves them with an adhesive patch after the micro-grippers grab the stomach tissues using its self-folding mechanism. However, experiments indicated that the yield of micro-gripper retrieval is low (3%), and in some cases a physician may prefer a targeted biopsy to the stochastic sampling performed by the micro-grippers.

Regardless of the location in the GI tract, one of the main limitations of all prior designs is that they can only take superficial biopsy samples. Those are useful to retract the tissues on the mucosal layer of the GI tract, however, it is difficult to reach deep masses inside the GI tract. Those mechanisms can miss submucosal tumors (SMTs), which can lower the diagnostic accuracy.

This chapter presents a novel magnetically actuated soft capsule endoscope with fine-needle capillary biopsy (FNCB) functionality called B-MASCE. FNCB is a type of biopsy technique to extract tissue samples using a fine needle. It was reported that fine-needle biopsy technique provides better accuracy than other biopsy techniques like forceps or brush, with the absence of complications in the GI tract [91, 92]. Because the needle can penetrate deep inside the mass of

a lesion, this technique improves diagnostic accuracy even in the case of SMTs.

The design of B-MASCE enables both the required motion for FNCB (axial jabbing motion of the needle) and rolling locomotion on the surface of a stomach. It is controlled by the magnetic force and torque on an internal magnet with external magnetic field control. Soft material-based legs connecting the two ends of the capsule work as a spring and a guide for the needle. The design is based on the clinical data suggesting the appropriate needle gauge and penetration depth for FNCB. *Ex vivo* experiments and a demonstration were performed in a porcine stomach with simulated SMT phantom tumors, and it was verified that biopsy samples were successfully captured.

5.2 Application Scenario

5.2.1 Fine-Needle Biopsy Techniques

Fine-needle aspiration biopsy technique, also known as fine-needle aspiration cytology, describes the method of aspirating cells from suspicious tissue lesions through a thin and hollow needle. During the procedure, a hollow needle is inserted into a mass to extract samples of tissue. Once removed, they are sent to the laboratory for further examination. It is commonly used to investigate lumps located in the thyroid or the breast, and it has also been successfully applied in the GI tract [93].

There are two types of fine-needle biopsy techniques. During the so-called FNAB, the fine needle is passed into the tissue and a negative pressure is applied by means of a syringe attached to the needle. The second method is called fine-needle capillary biopsy (FNCB) technique. The needle is passed into the tissue, and five to ten successive fast jabbing movements in and out of the tissue are performed [94, 95, 96]. The capillary force in the needle retains the detached cells inside the lumen. Clinical research has shown that there is no difference in terms of the diagnostic accuracy between the two techniques and it is recommended to use theB FNC

technique due to the technical ease [97].

Fine needle biopsy techniques have better diagnostic accuracy over forceps biopsy and brush cytology in GI tract applications [93, 98, 99, 100]. Clinical research by Zargar *et al.* has shown that FNAB outperforms the other two techniques in upper GI application (overall diagnostic accuracy: FNAB=94%, Brush=85%, Forceps=88%). Especially in case of submucosal tumors, infiltrative malignancies, and ulceronecrotic malignancies, FNAB is significantly better as the needle can penetrate deeply into the tumor mass while the other methods only capture superficial tissues of the stomach (e.g. diagnostic accuracy for SMT: FNAB=93%, Brush=7%, Forceps=14%) [91].

5.2.2 FNAB application on MASCE: B-MASCE

FNAB technique is applied to our previous magnetically actuated soft capsule endoscopy (MASCE) platform [33]. Fig. 5.1 shows the prototype of B-MASCE. A fine-needle is attached to the top part of it, and the capsule collapses along its longest dimension in order to deliver the needle out of the bottom part of the capsule. More details of the design will be discussed in the next section.

Fig. 5.2 shows the overall application scenario. First, B-MASCE is swallowed by a patient. For the protection of the esophagus, the robot is capsuled by ice as proposed in [101]. After the ice has melted, the capsule can move around inside the stomach to visually inspect the stomach wall with the on-board camera. The stomach is insufflated by carbonated water to ensure free movement of the capsule and a clear view of the surface of the stomach. If a suspicious lesion is found, then B-MASCE is positioned on the lesion's surface, and performs FNAB. After the operator has completed the procedure, the capsule is retracted by a thin tether attached to its top body. After the retraction, the needle is taken out and attached to a syringe to remove the tissue inside the needle. The removed tissue is smeared, stained, and fixed on a microscope slide, and sent to a cytology center in a hospital.

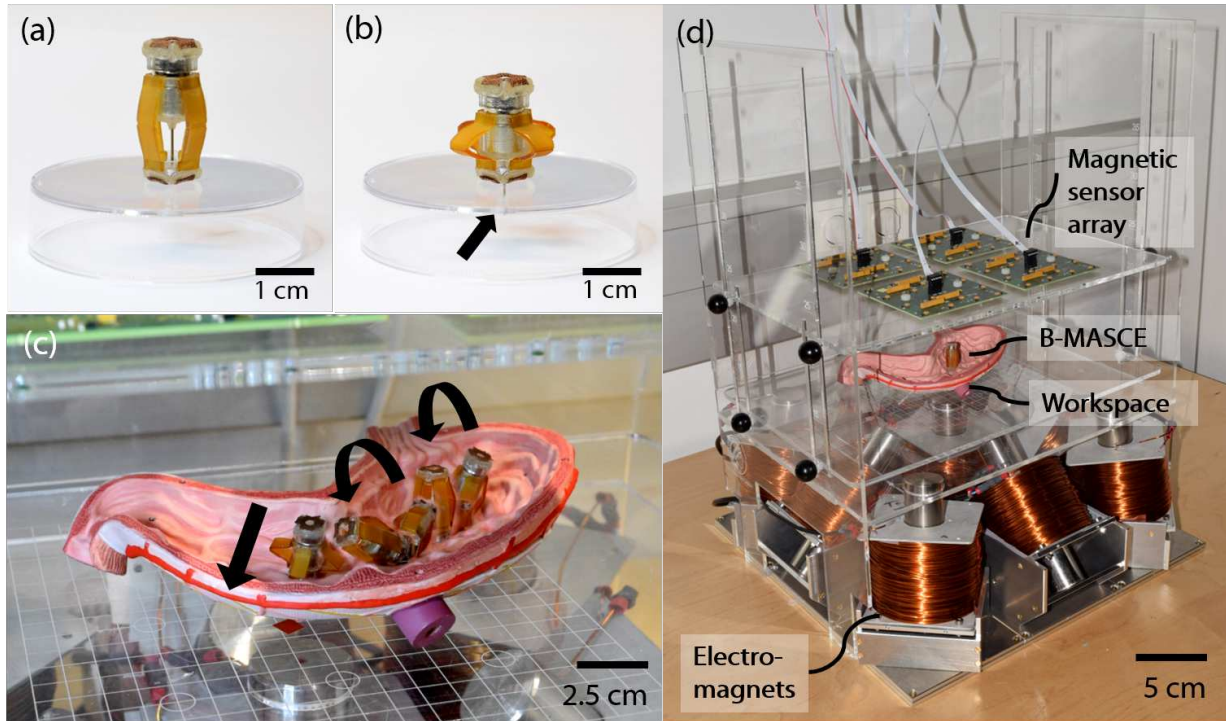


Figure 5.1: Prototype of B-MASCE. **(a, b)** The robot collapses by the magnetic force, whereas the magnetic torque stabilizes the angle of the robot. The robot exposes the biopsy needle by collapsing. The black arrow indicates the exposed needle. **(c)** The robot performs rolling locomotion and collapsing motion on a plastic human stomach anatomy model. The curved arrows indicate the rolling locomotion, and the straight arrow indicates the collapsing motion. **(d)** The robot is manipulated by a custom designed magnetic actuation and localization system. The magnetic localization system is composed of multiple magnetic sensor arrays, and the magnetic actuation system is composed of multiple electromagnets.

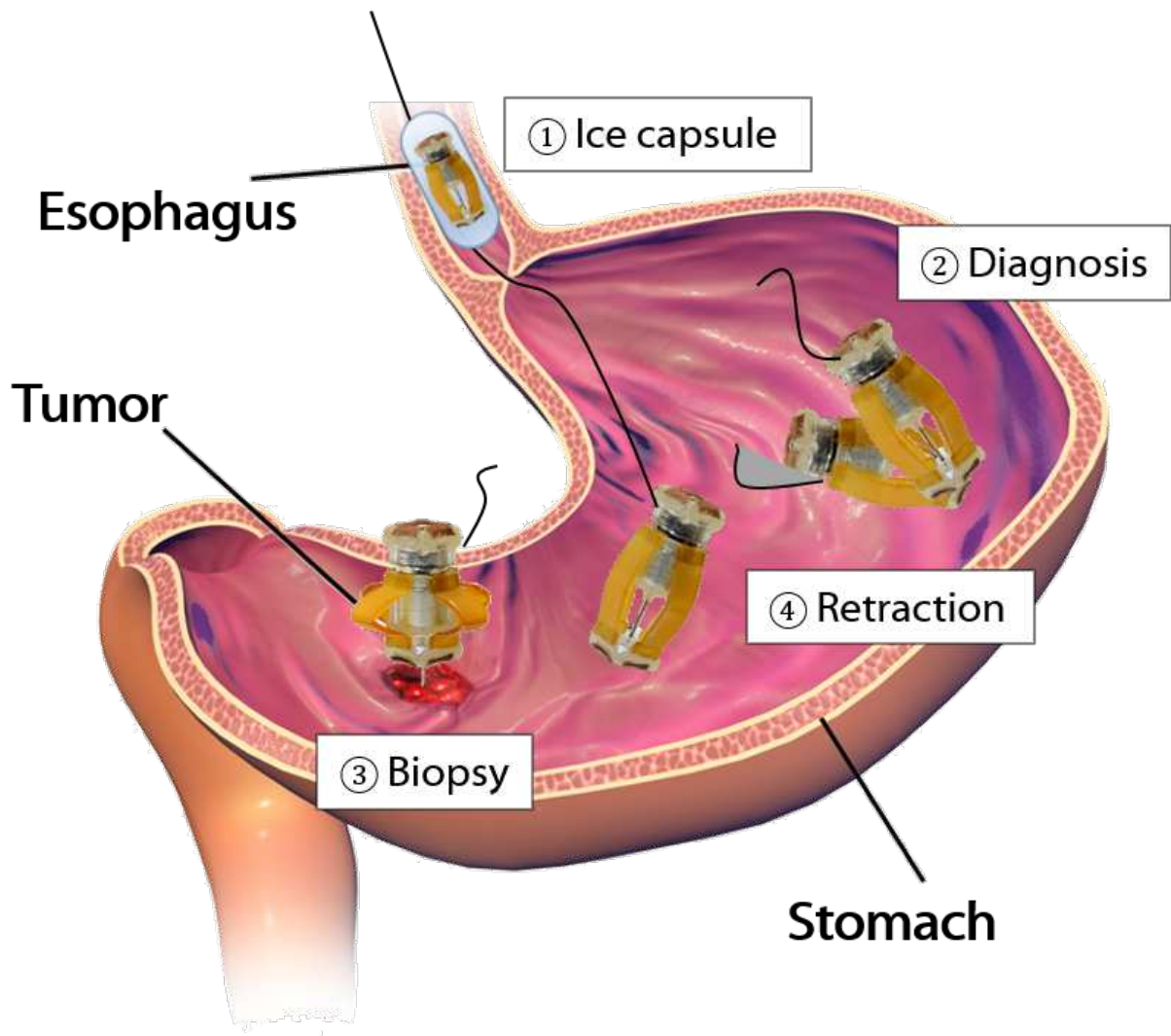


Figure 5.2: Application scenario. The robot reaches to the stomach through the esophagus. The ice capsule protects the esophagus while the robot passes by. The robot performs a visual endoscopy with rolling locomotion and camera orientation control. Afterwards, the robot reaches to a suspicious lesion. The robot performs biopsy and is retracted by a thin tether attached to the top part of the robot. (Stomach illustration in background: “Gastric Ulcer” by BruceBlaus / CC BY)

Table 5.1: Design Parameters

Overall dimension	$\varnothing 12 \text{ mm} \times 30 \text{ mm}$
Fine-needle	24 G, 15 mm (length)
Penetration depth	10 mm
Magnet	NdFeB 52 G, $\varnothing 8 \times 12 \text{ mm}^3$
Sarrus linkage:	
-Young's modulus	2.07 MPa
-Leg dimension	14 mm (H) \times 6 mm (W) \times 1.5 mm (D)
-Flexure hinges dimension	Circular: 0.275 mm (D), 0.4 mm (radius) V-Shaped: 0.275 mm (D), 135° groove

5.3 Design of B-MASCE

5.3.1 Design Features

Fig. 5.3 shows the design features of B-MASCE, which is composed of a fine-needle, a permanent magnet, a four-legged Sarrus linkage, an upper housing, a lower housing, anti-slip pads and a tether. The magnet exerts magnetic force and torque to the robot in response to a controlled external magnetic field. The magnetic torque is used to orient the capsule and the magnetic force is used to collapse the Sarrus linkage and deliver the needle through the hole in the bottom of the capsule.

The restoration force from the Sarrus linkage restores the shape of the capsule when the magnetic force is removed. Sinusoidal variation of the axial magnetic force causes repeated smooth motion of the needle in and out of the tissue, which is the required motion for the FNCB technique. The Sarrus linkage also restricts the collapsing motion to guide the needle along the axial direction of the capsule, which makes the motion insensitive to slight variations in the applied magnetic fields. The anti-slip pads enhances the friction during the collapsing movement to prevent unintended capsule motion prior to the needle penetration.

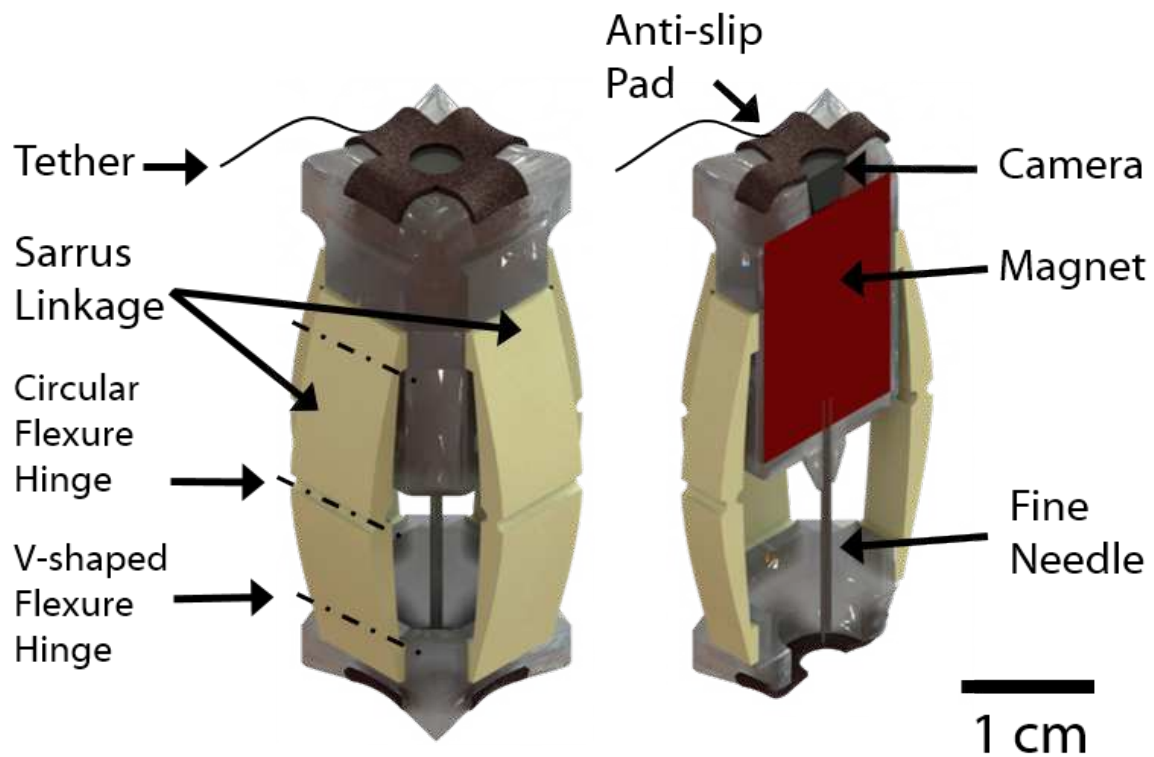


Figure 5.3: CAD model of B-MASCE. The robot is composed of a magnet, a camera, a needle, a lower body, an upper body, a Sarrus linkage, anti-slip pads, and a tether.

5.3.2 Design Parameters

Table 5.1 shows the design parameters of B-MASCE. In this prototype, the design parameters have been selected to meet the clinical requirements and to prove initial feasibility.

Needle Gauge. Clinical research has shown that 19 gauge (G) to 25 G are recommended [102, 103] to penetrate into tissues and get biopsy samples, and there is no performance difference in the range. For the capsule a 24 G hypodermic needle was chosen that has $\varnothing 0.5652$ mm outer diameter and $\varnothing 0.311$ mm inner diameter.

Penetration Depth. The average stomach thickness is 5.107 mm [104], the average upper GI tumor size is 58 mm (diameter), and the upper GI tumors are visually identifiable at sizes greater than 20 mm diameter [105]. In the case of SMT, the needle penetration depth should be longer than the thickness of the wall, but not so long that the full thickness is pierced. The penetration depth is chosen as 10 mm to meet both criteria.

Magnet Size. The magnet must be large enough to generate sufficient magnetic force and torque. As the size of the capsule is limited, the size of the magnet is chosen to be the maximum size possible inside the capsule's upper body. The magnetic force and torque are controlled by the external magnetic field, which was discussed in Chapter 4 in detail. The magnetic force should be larger than the sum of the restoration force of the Sarrus linkage and the penetration resistance of the targeted tissue. The penetration resistance is different for every tissue and there is no clinical data on stomach tumor tissue. However, as the magnetic force can be adjusted easily by the external magnetic field, this is a matter of tuning for each tissue. In the current state of the research, we have used the penetration resistance of a needle with a liver tissue, which is almost 0.05 N at 10 mm penetration with a 18 G ($\varnothing 1.27$ mm) needle [106].

Leg Design. The Sarrus linkage leg design is adopted from the previous design shown in [33, 35, 36, 56]. However, for the biopsy functionality, the linkage must be tuned to ensure that the combined magnetic and linkage forces provide sufficient net force for inserting and retracting the needle. For the design of the linkage, the retraction force is more critical than insertion force,

because the insertion force can be safely increased by generating stronger external magnetic field gradients. However, the capsule is designed to retract the needle using only the restoring force of the compliant legs. This is done for safety; if the field gradient were used to retract the needle, it could cause the capsule to suddenly leave the stomach wall, resulting in a momentary loss of control. Thus, we designed the legs to be stiff enough to restore the capsule shape against the tissue's retraction resistance, which is 0.4 N at 10 mm penetration [106].

There are in total twelve hinges in four Sarrus linkage legs. The rotational stiffness of each hinge can be calculated with the equations introduced in [107]. The upper and lower hinges are regarded as V-shaped flexure hinges and the middle one as a circular hinge. Using the values in Table 5.1, the dimensionless rotational stiffness is expressed as

$$K = \frac{1}{Ebt^2} \left(\frac{M}{\theta} \right); K_V = 0.3513; K_C = 0.0643, \quad (5.1)$$

where K_V and K_C are the dimensionless rotation stiffness values using the empirical fitting data from [107] for V-shaped flexure hinges and circular hinges, respectively, E is the Young's modulus of the material, b is the depth (z -direction in Fig. 5.4a of the hinges), t is the minimum thickness of the hinges, M is the moment on the hinges, and θ is the rotation angle. All the units are in SI unit and *rad*.

The compression force induces torques on the hinges, which results in angle changes in the hinges and a vertical translation of the upper body. Based on the kinematics of the linkages, the relationship between the penetration depth and restoration force of the capsule is expressed as

$$\begin{aligned} F_r &= Ebt^2 \left(8K_V \frac{\theta}{r \sin \theta} + 4K_C \frac{2\theta}{r \sin \theta} \right); \\ \Delta L &= 2r(1 - \cos \theta) \end{aligned} \quad (5.2)$$

where F_r is the restoration force. Using (5.2), the restoration force is plotted with the penetration depth in Fig. 5.4b. The restoration force is always larger than the maximum needle retraction

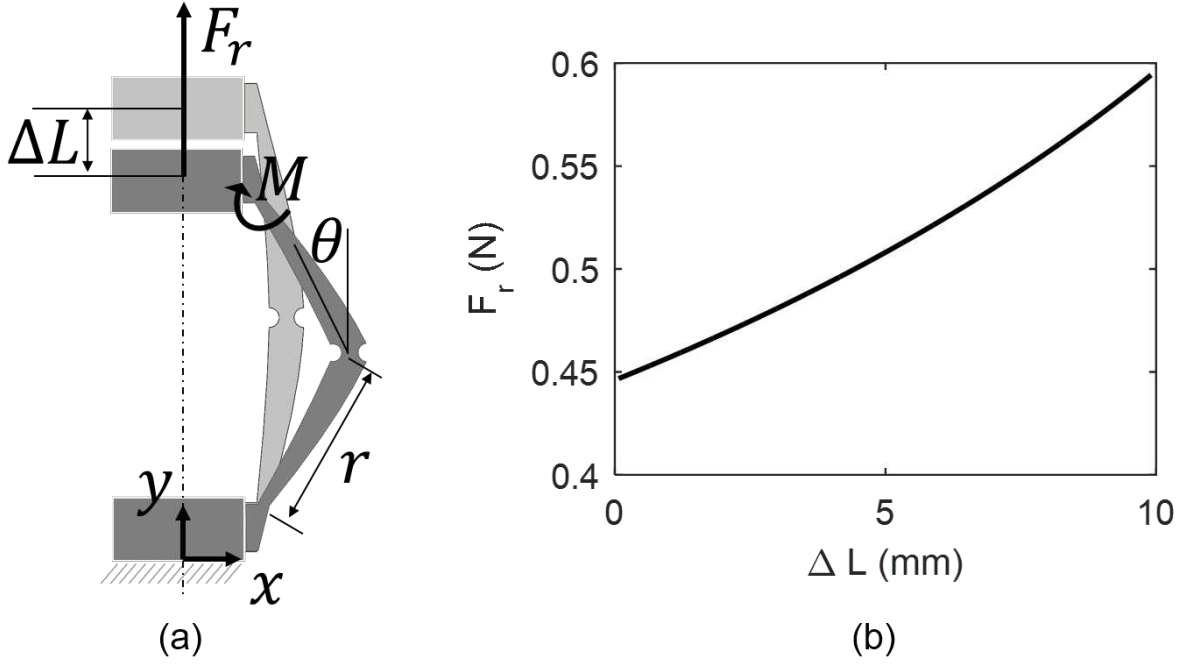


Figure 5.4: Restoration force estimation. (a) Diagram for the estimation of restoration force of the capsule by the penetration depth. Counter forces and counter moments are omitted for the visibility. (b) Restoration force along the penetration depth. The legs are designed to overcome the tissue resistance force when the needle is being retracted.

resistive force (0.4 N, 10 mm penetration) [106], the needle will be retracted when the external magnetic force is removed. Although the current design is enough to fulfill the requirements for FNCB, it might be useful to apply magnetic shape programming techniques [108, 109] to the legs for additional functionality.

5.3.3 Fabrication

The robot is fabricated using 3D printing and polymer molding techniques. Firstly, the robot is designed in a computer-aided-design (CAD) tool (SolidworksTM, Dassault Systèmes). Detailed mechanical drawings are provided as Fig. D.1 in Appendix D. The solid parts of the robot, the upper body housing and the lower body, are directly 3D printed (Material: VeroClear, Printer: Objet 260 Connex3, Stratsys, Ltd.). The Sarrus-linkage legs are polyurethane casts

(ST-1060, BJB Enterprise Inc., Young's modulus: 2.07 MPa) from a negative molding. The negative molding was fabricated using silicone rubber (Mold Star™ 15 Slow, Smooth-on, Inc.) with 3D printed master parts. The detailed recipe is explained in [33]. The fabricated housings and legs are combined using cyanoacrylate glue (LOCTITE 406, Henkel Co.). The hypodermic needle (24 G \times 1", B. Braun Co.) is cut to 12 mm length by a nipper, and then inserted into the upper housing. The cut part of the needle remains open. After the needle is attached, a permanent magnet and a dummy camera are inserted inside the upper body. The anti-slip pads were cut from sandpapers and attached to the body using. The choice of the sandpaper does not preclude any means of the surface treatment of the robot.

5.4 *Ex vivo* Experiments

We have conducted *ex vivo* experiments to prove the concept and feasibility of B-MASCE. A porcine stomach is used as an *ex vivo* experiment model. The porcine stomach presents slippery mucosa layer as well as wrinkles like a human stomach, which are the challenges for the manipulation of the robot. To simulate targeted tumors, we created gelatin-agarose phantom tumors, based on the method from [110], with fluorescent bead mixed in the *ex vivo* model. Those phantom tumors simulate the mechanical properties of real tumors. The fluorescent microbeads are used for the identification of the biopsy results. Two tumors are created between the second and third layers of the stomach wall to simulate sub-mucosal tumors (Fig. 5.5A) [111]. The *ex vivo* model was placed inside the magnetic driving system (Fig. 5.5B).

Preparation of *ex vivo* model

We used the porcine upper GI-tract with simulated submucosal tumors (SMTs) for the *ex vivo* experiments. The preparation of the *ex vivo* model was in the order of opening, washing, tumor creation, tumor injection, and fixing on a frame. The anterior wall of the stomach is cut by a scalpel, and internal material is washed out. After the wash, the material for the simulated

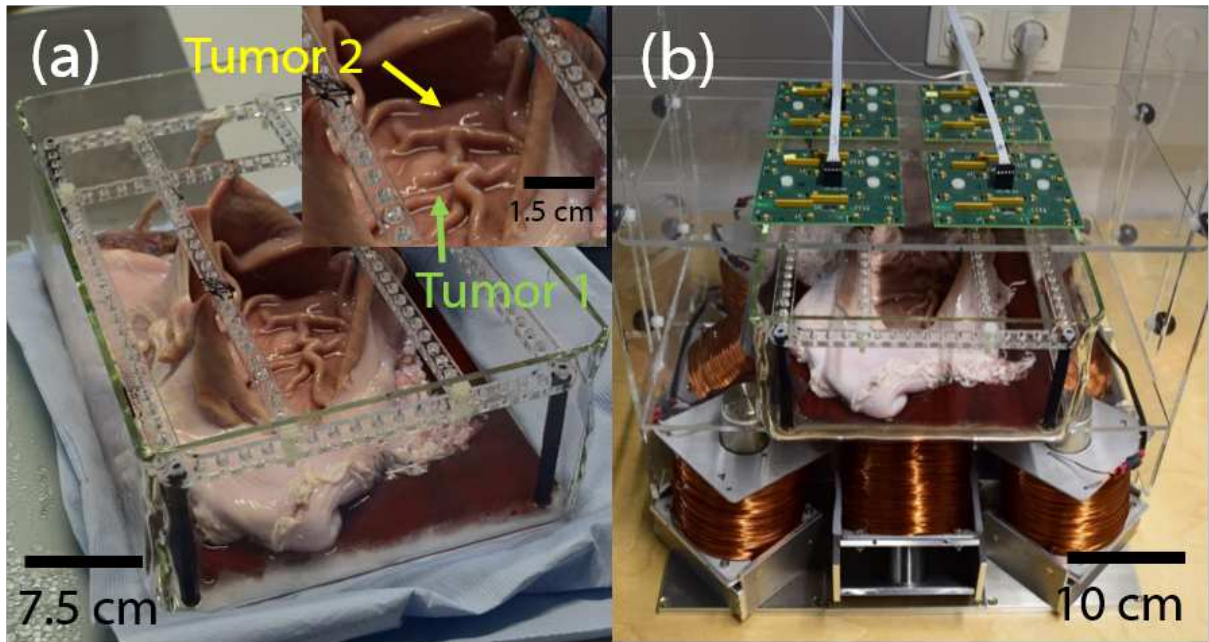


Figure 5.5: *Ex vivo* model preparation. (a) The picture shows the prepared *ex vivo* porcine stomach with created two sub-mucosal phantom tumors. The arrows indicate the embedded two phantom tumors inside the layers of the stomach walls. (b) The *ex vivo* model was placed inside the magnetic actuation and localization system.

tumors are created. Those tumors are created using gelatin-agarose mixture to simulate the mechanical property of the tumor [110]. The gelatin from bovine skin (~ 225 g Bloom, Type B, Sigma-Aldrich Co.) and agarose (BioReagentsTM BP1423-500, Fisher Scientific Int, Inc.) were boiled to 90°, mixed, and cooled down. At 60°, the mixture was divided into two parts. Each part was mixed with different fluorescent micro beads (3 μ m, Fluoro-maxTM, G0300 & R0300, Thermo Fisher Scientific co.). At 40°, 10% formalin was mixed to crosslink the gelatin and agarose. At 30°, the mixtures were injected between the second and the third layers of the stomach wall using syringes with needles. The injection bulges the layers as like a shape of a tumor. After the injection, the stomach is cooled to fix the gelatin-agarose mixture firmly.

***Ex vivo* experiments**

The *ex vivo* experiments were conducted with 10 trials for each tumor. The robot performed the rolling locomotion and biopsy via the teleoperation. The user observed the experiments through a camera attached on top of the fish tank of the *ex vivo* model (same view as Fig. 5.6). Each demonstration took approximately 1.5 minutes for the approach and the biopsy. After the biopsy, the robot was retrieved and the liquid and solid mixture inside the needle was ejected on glass slides by applying a positive air pressure on the one side of the needle. The ejected samples were examined under a fluorescent microscope.

The fluorescent signal had shown the 100% ($n = 10$) identification rate of Tumor 1, and 70% ($n = 10$) identification rate of Tumor 2. Figure 5.7 shows the samples for each tumor. The samples show the fluorescent micro-beads in masses of gelatin-agarose mixture. The results indicate that the robot collected sample from each phantom SMT.

In addition to the *ex vivo* experiments, we also performed an active imaging test with an on-board camera. We used NanEye 2-D (AMS co.). Adding the camera naturally provides a tether to the robot, which would be used to retract. In this case, the experiment with the camera also becomes a test for the control stability with a disturbance from the tether. During the active

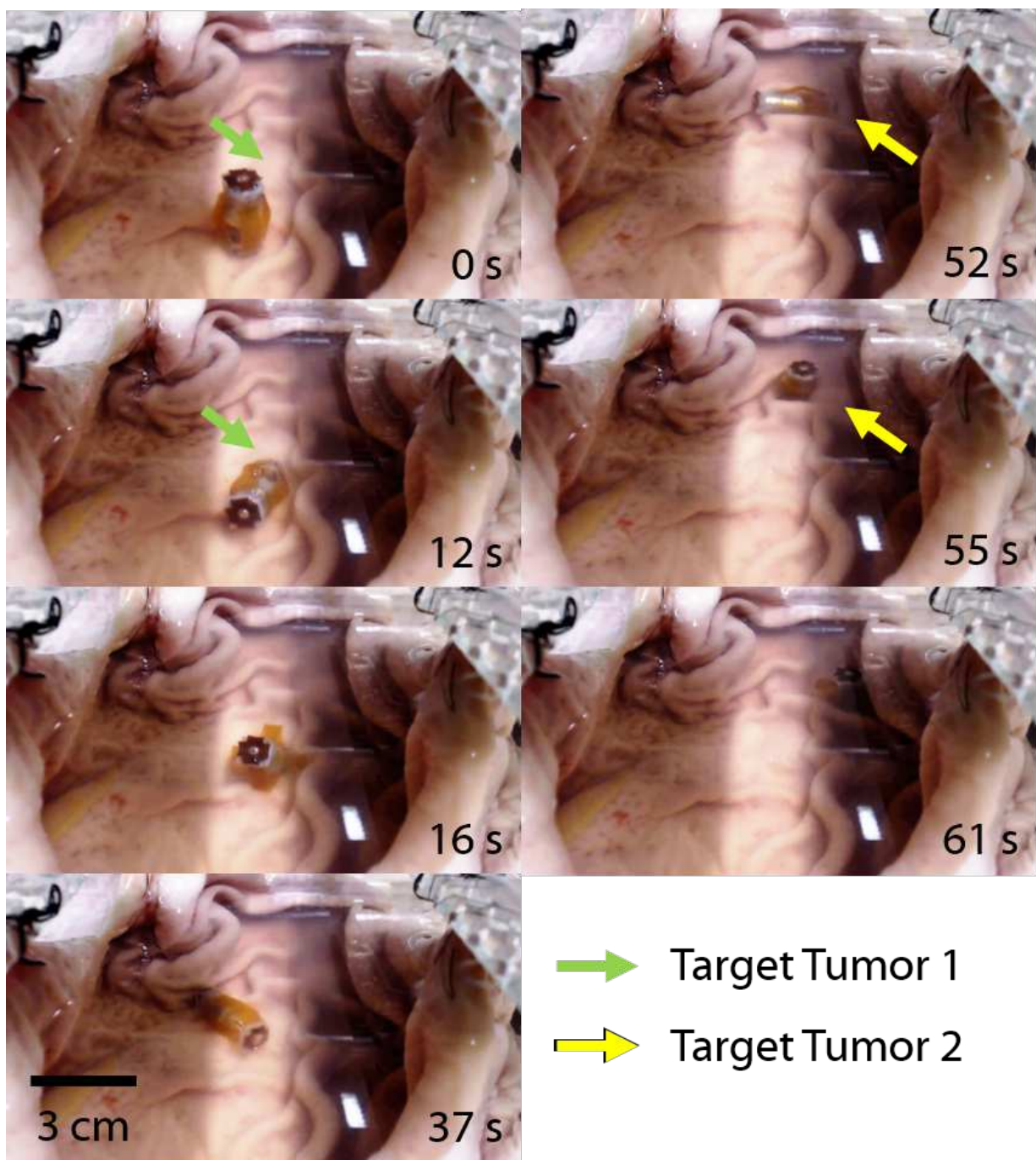


Figure 5.6: *Ex vivo* demonstration of B-MASCE. The robot performed rolling locomotion to approach tumors and performed fine-needle biopsy on each tumor. The stomach was filled with water to emulate a water-filled patient stomach. The video is found in Supplementary Information.

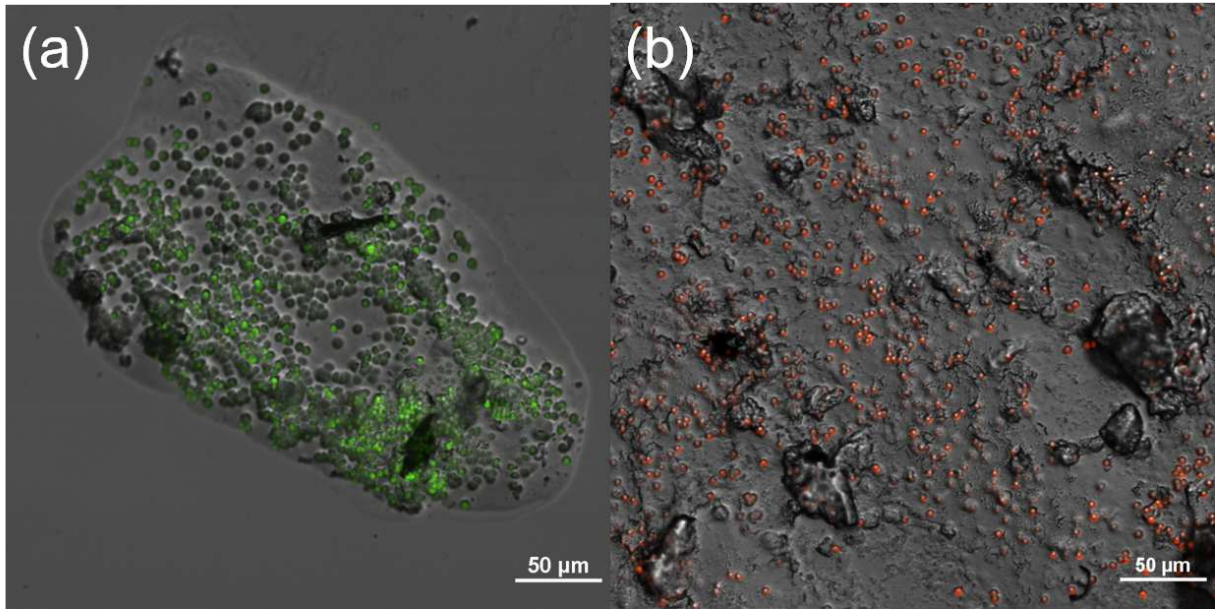


Figure 5.7: Fluorescent microscope images of the extracted biopsy samples. The images show the fluorescent microbeads inside gelatin-agarose mixture from the biopsy samples. The gelatin-agarose phantom tumors, Tumor 1 and Tumor 2 in Fig. 5.6, had green and red micro-beads, respectively, for after-operation characterization. Green (a) and red (b) pseudo-colors were applied to indicate green and red fluorescent micro-beads.

imaging test, the robot performed the same procedure as the *ex vivo* experiment. The robot approached both tumors and performed repetitive collapsing motions. During the procedure, it was found that the image quality of the camera was low, and it was hard to distinguish the tumor from the background solely relying on the on-board camera. Additionally, the view of the camera was occluded by the mucosa from the stomach after the camera contacted the surface of the stomach. The experiment result suggest that the camera needs to be improved and a device to remove mucosa on the camera is needed.

5.5 Discussion

B-MASCE collects biopsy samples from the cores of tumors, which enables the diagnosis of not only mucosal tumors but also submucosal tumors. B-MASCE has a potential to enhance the diagnostic accuracy of the stomach endoscopy and minimize costs for additional biopsy procedures. The simple design of the robot makes the robust biopsy performance. The robot had shown 85% identification rates (averaged rate for the two tumors trials) in the *ex vivo* experiments. Utilizing the multi-functions of each component, the design complexity is minimized. The magnet is used for actuation and tracking, and the Sarrus-linkages are used for the robot body, safety spring, and needle alignment. Minimal design of the robot makes not only the robot to be robust in the practice, but also inexpensive for fabrication, considering disposability of the capsules.

The safety of B-MASCE is one issue to be considered. B-MASCE is naturally safe due to its own safety spring design of the Sarrus linkages with the absence of the magnetic field. The source which gives an unintended collapse is, therefore, the peristalsis of the esophagus and the stomach. First, the esophagus is a narrow tube and constantly gives pressure to the side of the robot when the robot travels through. This helps to align the long axis of the robot with the direction of the esophagus, where the peristalsis does not cause the collapse of the robot. With a little chance, the robot might orient in the other way so that the peristalsis cause the collapse of

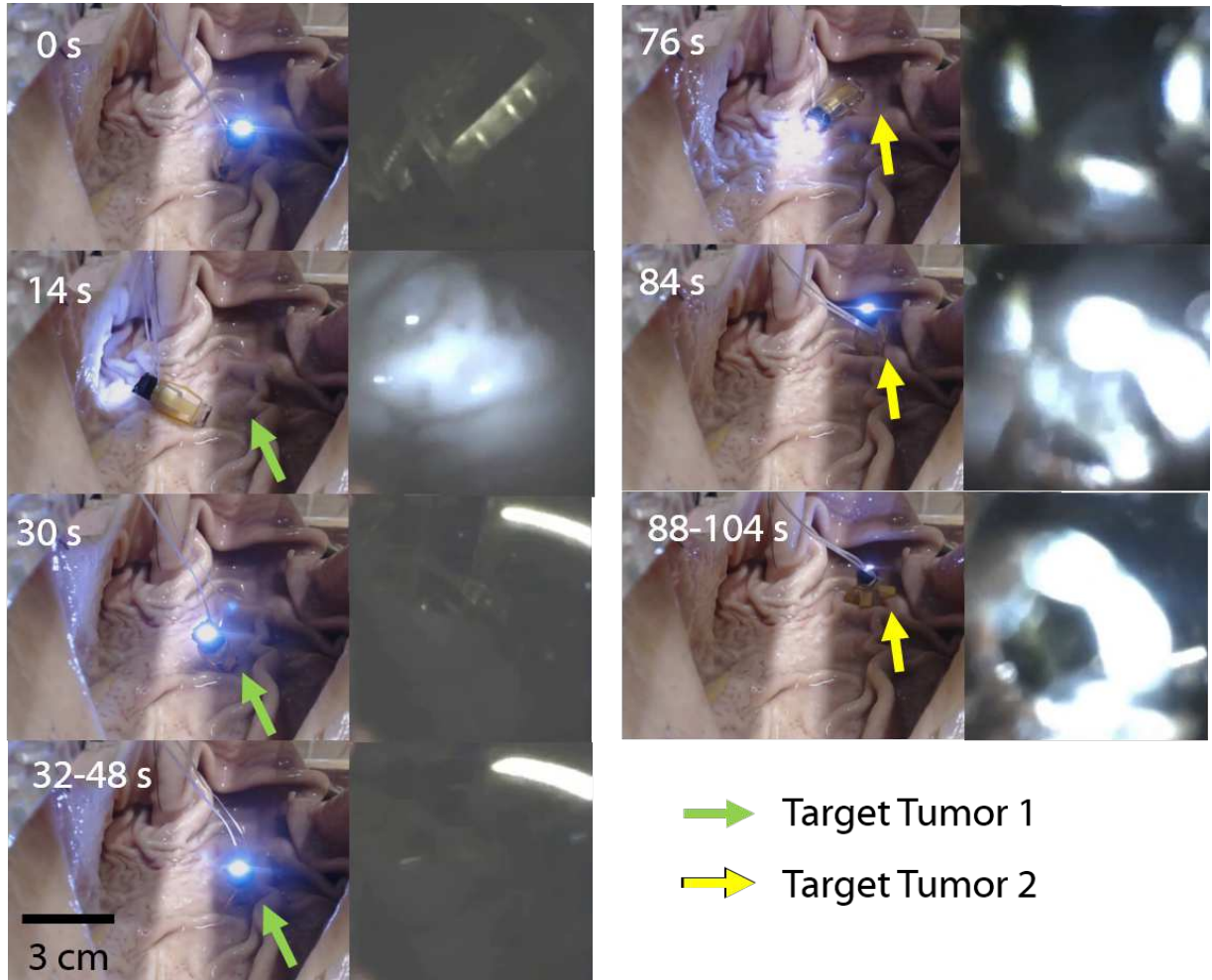


Figure 5.8: Active imaging test of B-MASCE. In each time frame, B-MASCE's motion observed by the external camera is shown (left) and the view from the on-board camera is shown (right). B-MASCE performs biopsies with the on-board camera in the same procedure as the *ex vivo* biopsy experiments in Chapter 5. After 76 seconds, the camera view was occluded by a patch of mucosa attached on the lense of the camera.

the robot. To prevent this case, we suggest to capsule the robot with ice as in the application scenario. After the procedure, the robot is retracted by the tether attached to the top part of the robot. The tether pulls the robot from the top, which induces an auto-alignment of the robot with the esophagus, thus robot does not orient perpendicular to the esophagus, preventing the collapse of the robot.

In the stomach, the robot is safe because the stomach is a large cavity and does not give direct collapsing force to the capsule by the peristalsis. In clinical applications, it is suggested to swallow gas producing drinks to expand the stomach as much as possible [112]. This improves the visual diagnostic accuracy by showing all lesions which could be hidden by the stomach wrinkles. At the same time, the expansion of the stomach prevents the stomach to collapse and B-MASCE is safe to be used.

However, there are some challenges left for future works. The results showed that only for the first tumor had 100% identification, but 70% identification for the second tumor. The second tumor was in a hard condition for the biopsy (see Fig. 5.6 52 s - 61 s), where the tumor was close to the side wall of the stomach. There was a narrow room to place the robot and to collapse it. This challenge led to a relatively hard manipulation of the robot and a couple of misses in the biopsy. This challenge could be addressed when the patient could change his/her orientation, so that the tumor lies on a preferred place of the workspace, and the robot has enough room to move around.

Another challenge is that the current work presents *ex vivo* results, which does not cover all the cases in *in vivo* environments. First, a robust controller which can reject disturbances from peristalsis should be implemented and tested. Although the current version of the controllers are designed in a way to be open-loop stable using the magnetic energy well, the realistic test with the peristalsis might induce a different behavior than expected. Second, the camera vision would be another challenge in the *in vivo* environments. With the current version of the robot, the experiments were done while the user was observing the experiment with an eagle-eyed view from the external camera. In the real environment, the view from the outside camera is not

available, and the user should rely on the camera vision from the capsule. When the robot moves by the rolling locomotion, it would easily cause a coordination problem. Additionally, when the robot performs the biopsy, the robot does not observe the biopsy directly. This is because the camera is on the other side to the needle. Adding a camera nearby the needle would provide an additional view towards a tumor, however, the view is too close to the tumor to confirm whether the robot is aiming the tumor. Ideally, the system should construct an on-line 3D map of the stomach as it moves, and the location and angle of the robot should be registered in the map. This would give a global map where the user easily locates the lesions and the target for the biopsy. In this way, the tumor position is registered in the global map, and the robot is able to perform biopsy with the help of 3-D global positioning. There has been already an effort to adapt Simultaneous Localization And Mapping (SLAM) techniques in surgical environments [113, 114], which could be applied to B-MASCE in the future.

Additionally, the configuration of the actuation system could be optimized. The current design is optimized to give a strong magnetic force towards the general direction of the magnetic cores. This configuration would not be optimal for the other direction for the biopsy. For example, when the robot needs to take the sample in the superior or inferior wall of the stomach, the system might not give an enough magnetic force to collapse the robot. A different design of the actuation system, such as [115], could be considered for the biopsy system, which is capable of taking biopsy in all locations with all directions.

5.6 Conclusion

A magnetically actuated soft capsule endoscope designed for fine-needle capillary biopsy was proposed. The integrated fine-needle at the top part of the robot can penetrate into a lesion and capture samples inside the hollow needle using a technique similar to standard clinical procedure. A permanent magnet inside the robot generates a magnetic force and torque through its interaction with an external magnetic field, and it is simultaneously used as a tracking source

at the same time. The soft material-based Sarrus linkage works as a needle guide, spring, and body for the capsule. This allows the robot to collapse, deploying the needle into the targeted tissue, and also provides the restoration force for the needle retraction when the external magnetic field is removed. A computer controlled electromagnetic system and magnetic sensor array were employed to control the external magnetic field precisely. Rolling locomotion and biopsy were demonstrated *ex vivo* on a porcine stomach model with embedded gelatin-agarose phantom tumors. After the demonstration, it was confirmed that a biopsy sample was successfully captured. The registration and mapping of the stomach, and *in vivo* demonstration of such a capsule robot with a biopsy tool are areas of system development remaining.

Chapter 6

Summary

6.1 Thesis Contributions

In this thesis, we introduced methods on localization, calibration and control of the magnetically actuated soft capsule endoscopes (MASCEs) and its application on the biopsy task. Those methods serve as basic techniques to automate MASCEs. We envision that the final MASCEs would be able to perform a visual endoscopy and therapeutic functions autonomously under the supervision of a doctor. I have described specific contributions below:

- Developed a real-time magnetic 5-D magnetic localization method under magnetic actuation. The method belongs to out-of-sight localization methods, which could be broadly applicable in medical environment.
- Developed an automatic calibration method for a magnetic localization and actuation system. The method allows to calibrate the non-linear magnetic actuation and sensing systems automatically. The method is useful for the system needs to be reconfigured often, or systems which requires frequent parameter updates.
- Designed controllers for MASCE's locomotion and diagnostic/therapeutic tasks. We investigated the usage of the magnetic energy well for controlling a magnetic-robot on a

surface. The controller is applicable to meso-scale magnetic-robot under non-uniform magnetic field actuation.

- Designed a fine-needle biopsy capsule robot and tested in *ex vivo* environment. We integrated the localization, calibration, and control methods shown above, and applied to a modified MASCE platform. The results had shown a promising result.

6.2 Challenges and Future works

6.2.1 Size Minimization

The proposed design in Chapter 5 has 12 mm diameter and 30 mm length, which could be further optimized to make it more comfortable to be swallowed. The overall size comes from the size of the magnet, which could be a challenge to optimize. The size minimization of the magnet minimizes the strength of the magnetic torque and force, and localization signal. This could cause the actuation and localization difficulties. At the current stage, we have already used the best commercially available magnetic materials and sensors/actuators. However, improvements in magnetic sensors and magnetic materials would help to reduce the size of the magnet inside the capsule in future, which would result in a smaller size of a MASCE.

6.2.2 Reconfigurable Actuation System

In Chapter 5, the special configuration of the magnetic actuation was used to exert strong magnetic force. The magnetic force is optimized towards the general direction of the magnetic cores, whereas it compromises the other direction's magnetic force in the workspace. However, in the real application, the required force would not be ideal to the system. Various direction of the biopsy would be required at different positions of tumors. In such a case, the patient may need to reorient or the system needs to be reconfigured.

A reconfigurable actuation system would be useful in such a case, where the system is

optimized dynamically to perform a specific task. This would improve the manipulation of MASCE in general, which might lead to improvement of the diagnosis quality. There has been already a study on a reconfigurable magnetic actuators [42], which could be applied in our application scenario.

6.2.3 Visual Coordination and Registration

The current robot presents a visual coordination difficulty. For example, the view of camera rolls when it performs the rolling locomotion. This would confuse a doctor who is performing the visual endoscopy solely relying on the vision of MASCE. Ideally, the doctor should have his own map of the stomach, and command inputs via the map. This is a visual 3-D mapping problem, where the Simultaneous Localization and Mapping (SLAM) technique could be applied. There have been already studies on SLAM techniques on surgical environments [113, 114], and these techniques could be applied for improving the coordination and registration of MASCE's vision.

6.2.4 Multiple MASCE Control

A multiple MASCE control could be a useful actuation scheme to perform better visual endoscopies and endoscopic operations. Currently, MASCE should perform the endoscopy and therapeutic functions all at once. This is a challenging task due to the size limitation of the capsule. In the current version, all the mechanisms and tools should be embedded into a single body. By dividing tasks and functions into multiple MASCEs, reliable tasks with smaller MASCEs could be performed. Especially, this could greatly help the visual coordination problem discussed in 6.2.3 because a camera carrying MASCE could observe another MASCE performing a therapeutic operation in a steady manner.

The multiple magnetic-robot control has been studied through the last decade in magnetic-robot community. The challenge of the multiple magnetic-robot control is that all magnetic-

robots receive global actuation input from the actuation system. However, the global input to multiple agent problem has been solved using the nonlinearity in the robot dynamics. The multiple magnetic micro-robot are controlled by using specialized surfaces [116], using inhomogeneous frequency responses in 2-D [117, 118], or even in 3-D [119]. Also the hysteresis of the magnetic-robots could be used for controlling multiple magnetic-micro-robots [120]. In meso-scale, multiple magnetic objects could be controlled simultaneously using the nonlinear dynamics of the magnetic objects in a MRI machine [121]. In this method, the magnetic objects should be spherical and mechanically constrained in an apparatus like a gimbal.

Controlling multiple MASCEs is similar to the approach of [121] because of the size of MASCE. However, the difference is that MASCEs are not constrained mechanically like objects in gimbal. Rather, MASCEs are contacting a surface where they are free to move tangent to the surface, but not perpendicular to the surface. This special geometric constraint could be used to derive a control solution similar to [121]. However, this method would require very fast and accurate multi-object localization.

Another approach is to increase the dof of the actuation system. The actuation system in this thesis inherently uses the non-uniform magnetic field. This property provides individual magnetic field and gradient controls in multiple positions, as long as the actuation dof is larger than the total dof of the robots. For example, controlling two MASCEs would require at least 10 magnetic actuators. This approach requires more number of the actuators, however, localization of the robots are not critical as the approach above.

6.2.5 In Vivo Experiments

The final goal of this study is to apply MASCE to a patient in real applications. The value of the *in vivo* study is that it guarantees the overall performance of the robot in real environments before the clinical use. The tests will reveal the dynamic effect from movements of real organs. For MASCE, the major difference between the *in vivo* and *ex vivo* tests would be peristalses of

a human stomach and the limited vision solely relying on the on-board camera. Although the current version of MASCE showed good demonstrations in the *ex vivo* environments, rigorous tests for MASCE should be performed in *in vivo* environments to deal with all cases not have been observed yet.

The *in vivo* test scenario is described as follows. A pig cancer model, which has a tumor inside the stomach, must be prepared. The pig must be under anesthesia to prevent uncontrolled motions from the pig during the endoscopic procedure. The stomach is filled with water and MASCE encapsulated by ice is pushed inside the stomach using an additional tool. After the ice is melt, a doctor controls MASCE using the teleoperation system. A 3-D map of the stomach is created by robot's own mapping algorithm. A doctor examines the 3-D map of the stomach, and select the tumor model as the biopsy target. After the robot performs the biopsy, the robot is retracted by the tether attached to the robot. The needle inside the robot is retrieved and cytology analysis is performed. This procedure is performed more than 10 times to get a proper statistical analysis.

In the current setup shown in Chapter 5, the *in vivo* experiments could be partially performed because of the limited vision. With the current camera attached to MASCE (NanEye 2D, AMS AG.), it is hard to detect a lesion due to the low image quality. Thus, it is required to improve the camera quality significantly, or have an external view from a high quality camera, such as an endoscopic view. In the experiments, a subject should change his or her position and orientation depends on the location of a lesion in case the workspace does not cover the surfaces of the stomach of the subject.

Appendix A

Design, Fabrication, and Calibration of the Omni-directional Electromagnet

The omni-directional electromagnet is designed to actuate a MACE. The design guide-line is found in [41]. The paper suggests an optimal shape of the electromagnet, which minimizes multipole-fields effects leaving the dipole field dominant. The suggested optimal aspect ratio of each coil is applied in this design. The size of the electromagnet is determined to manipulate the MACE appropriately. As our study is relying on the rolling locomotion of the MACE, we have use the minimum torque to actuate the MACE. To roll the MACE-sized magnet ($\phi 1 \text{ cm} \times 2 \text{ cm}$ cylindrical NdFeB magnet with N42 grade), 0.75 mT is required in the workspace. By applying safety factor as 4, we have used 3 mT as the criteria as maximum magnetic field in the workspace when we apply 1 A in the z -directional coil. By applying the size of the magnetic field into the guide line of [41], the final dimension of the electromagnet is determined (Table A.1).

It was designed in computer-aided-design tools, and fabricated using CNC miling machines and manual copper wire wrapping (Fig. A.1). The design specs from Table A.1 are used for the designing the frame of the electromagnet. The iron core is from a fabricated shot-put, whose permeability is not identified, but assures that its relative permeability is over than 500.

Table A.1: Specification of the Omnidirectional Electromagnet

Coil	x -axis	y -axis	z -axis
Inner box dim. (mm ²)	117.1×117.1	155.8×155.8	181.9×181.9
Outer box dim. (mm ²)	135.3×135.3	168.3×168.3	191.0×191.0
Coil wall length (mm)	136.4	169.4	193.3
Resistance of coil (Ω)	8.1	7.7	8.1
Iron core diameter (mm)	113		

The calibration process after the fabrication finds the electromagnet's magnetic property, thus the absence of the specific number for the permeability does not affect the performance of the electromagnet. Material for the frame is Aluminum A6061 (McMaster Co.), which has relative permeability of 1.000022, thus the magnetic effect is almost negligible. Coils are NEMA MW35C (MWS Wire Industries), which are standard motor wires. Total length of the used coils were approximately 2000 m. To avoid short circuits from scratching the wires enamel cover off, we have wrapped manually carefully.

After the fabrication, the Omnimagnet was calibrated. Each coil ran a specific electric current (e.g., 1 Ampere), and the magnetic field was measured in different positions. Using (2.2) and (A.2), we can calculate the diagonal terms of \mathbb{M} . Figure A.2 shows the calibration results. By averaging the data, x -, y -, and z -axes are 29.7 A·m²/A, 26.9 A·m²/A, and 44.4 A·m²/A, respectively. The values construct the orthogonal magnetic moment matrix

$$\mathbb{M} = \begin{bmatrix} 29.7 & 0 & 0 \\ 0 & 26.9 & 0 \\ 0 & 0 & 44.4 \end{bmatrix}. \quad (\text{A.1})$$

The B-field could be controlled using the B-field dipole model (2.2). We can find the required current input by inversing the equation as

$$\mathbf{I}_d = \frac{2\pi}{\mu_0} \|\mathbf{p}\|^3 \mathbb{M}^{-1} (3\hat{\mathbf{p}}\hat{\mathbf{p}}^T - 2\mathbb{I}) \mathbf{B}_d \quad (\text{A.2})$$

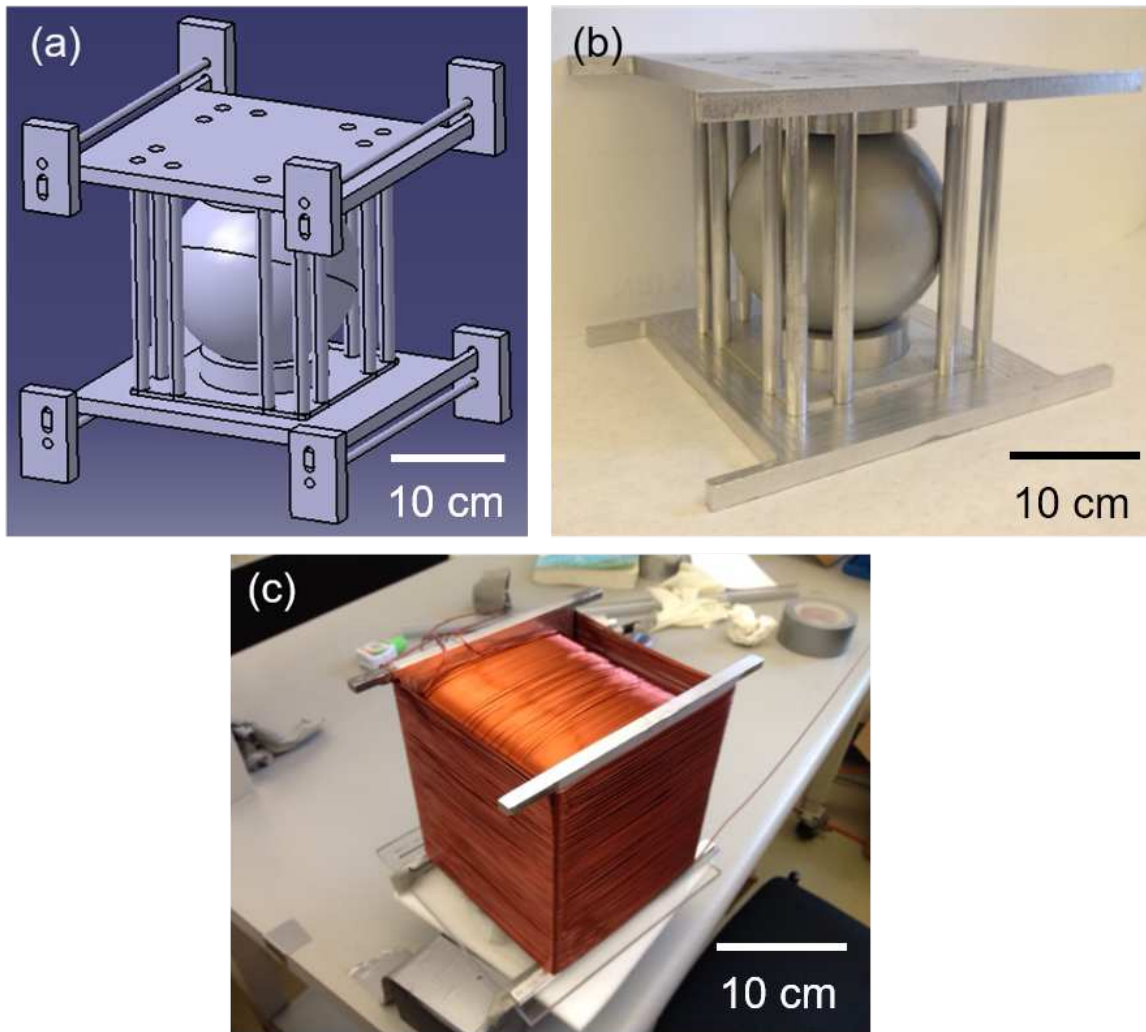


Figure A.1: Omnidirectional eletromagnet fabrication. (a) CAD model of the electromagnet. (b) The fabricated iron core and its frame. Aluminum is used for the frame. (c) Wrapped copper wires. Approximately 660 m of wire is used for each axis.

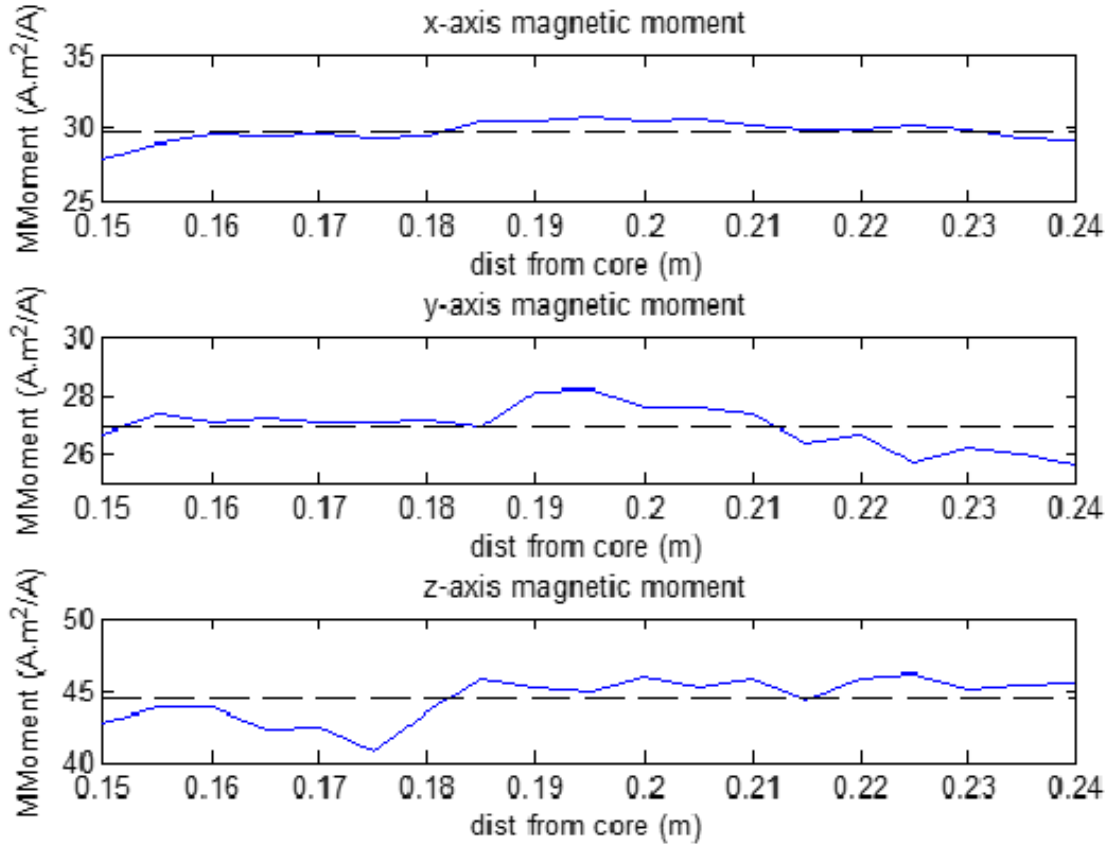


Figure A.2: Omnidirectional eletromagnet calibration. The B-field was measured in 19 different positions for each axis. The calculated magnetic moments were averaged after the measurements.

where \mathbf{I}_d is the current input to generated the desired B-field, \mathbf{B}_d , at point, \mathbf{p} .

Appendix B

Design and Fabrication of the Nine-Coil Actuation System

We changed our actuation system from Omnimanget to nine-coil actuation system (Fig. B.1) during the thesis study. The omnidirectional magnet has a full dof to change the magnetic moment in a fixed point, however, it compromises the strength of the magnetic moment due to a high demagnetization factor. When the task requires a strong magnetic field or gradient, the Omnimagnet requires relatively high electric currents, which might not be ideal for strong field actuation scheme. On the other hand, a magnetic core with a high aspect ratio generates much strong magnetic moment compared to a spherical core. This is due to the effect of the demagnetizing magnetic field, which is a function of the shape of the cores. It is found that the bigger the aspect ratio of the core is, the stronger the magnetic moment is [122]. We designed coils with 1,500 turns to generate strong H-field, and added a high-aspect ratio core to amplify the H-field. The specification of the electromagnet is shown in Table B.1. The measured settling time was 0.1 second.

We determined the configuration of the actuation system. We used the design framework from OctoMag design [73] and modified the framework in our need. Not like OctoMag system, we need very strong magnetic fields, and the actuators should remain in the other side of the

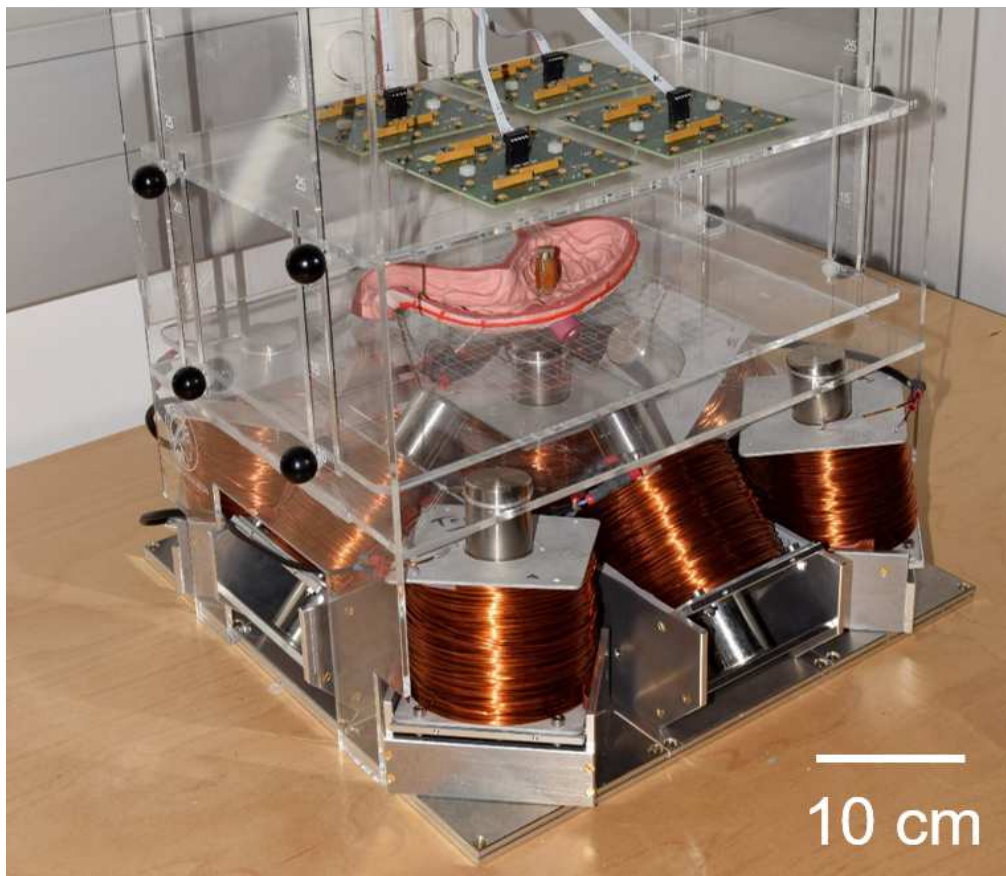
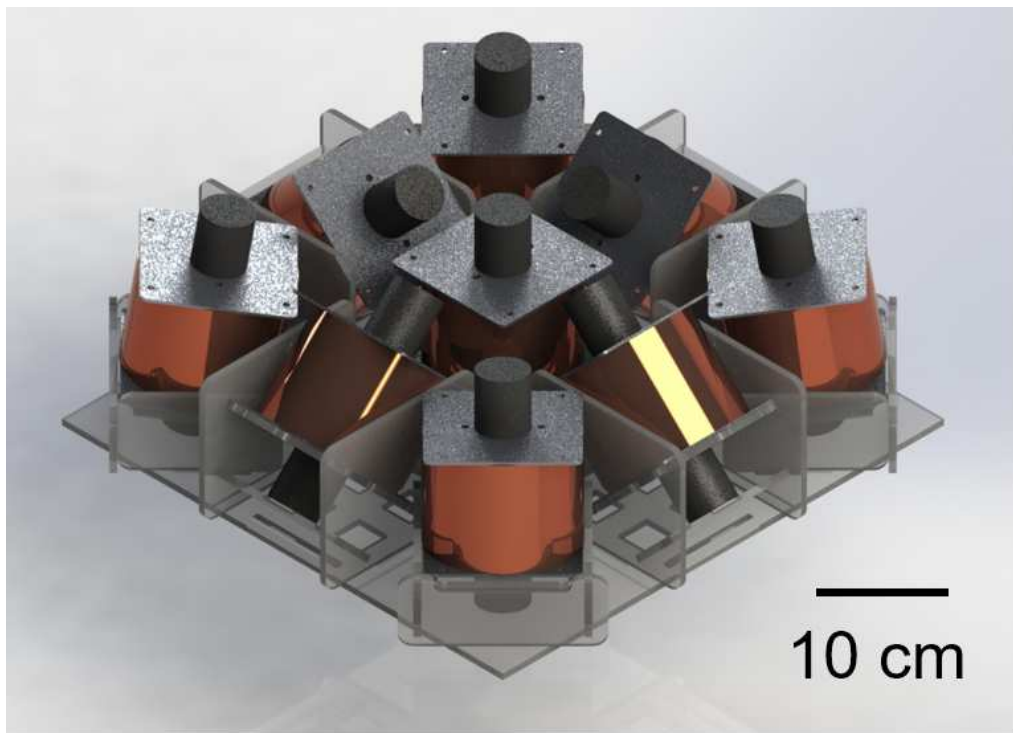


Figure B.1: Nine-coil system. (Above) CAD image of the design. (Below) The fabricated actuation system is with sensor arrays on top and a magnetic capsule on a plastic human stomach model in the workspace.

Table B.1: Specification of the electromagnet

	Value
Soft-iron core	Permenorm 5000 H2, VACUUMSCHMELZE
- Material	Ni-Fe
- Dimension	$\phi 36 \times 160 \text{ mm}^3$
Copper-wire coil	ENOFLEX-180 ($\phi 1.18 \text{ mm}$), HELCA Metal
- Dimension	($\phi 40(\text{in})-100(\text{out})$) $\times 80 \text{ mm}$, 1500 turns

magnetic sensors in the array to prevent the magnetic sensor saturation. Also we need space for the workspace in the middle, and preferably horizontally fully empty so that a patient can lie on the system. These criteria changes the fitness function formulation as well as constraints formulation.

Finally, we choose to increase the vertical directional magnetic field and gradient. This would give strong force with orientation stabilization. For example, in our application in Chapter 5, the system was capable of generating 0.8 N with $0.6 \text{ A}\cdot\text{m}^2$ magnet inside the workspace. In the optimization, the actuators are constrained in a plane separated from the magnetic sensors, but were allowed to change their orientations to optimize the magnetic fields.

To formulated the optimization problem, we consider the magnetic field and force at a permanent magnet inside the system. We consider that the magnet is in an arbitrary position and orientation. We can calculate the magnetic field and force as

$$\begin{bmatrix} \mathbf{b} \\ \mathbf{f} \end{bmatrix} = \mathbb{A}(\mathbf{r}_i, \mathbf{m}_i, \mathbf{r}_j, \mathbf{m}_j) \mathbf{I} \quad (\text{B.1})$$

where $\mathbf{b} \in \mathbb{R}^3$ is the magnetic field, $\mathbf{f} \in \mathbb{R}^3$ is the magnetic force, $\mathbb{A}(\cdot) \in \mathbb{R}^{6 \times 9}$ is the actuation matrix, $\mathbf{r}_i \in \mathbb{R}^3$ is the position of a magnet in the workspace, $\mathbf{m}_i \in \mathbb{R}^3$ is the magnetic moment of the magnet, $\mathbf{r}_j \in \mathbb{R}^{27}$ is the position package of the electromagnets in a long vector form (9 actuators positions), $\mathbf{m}_j \in \mathbb{R}^{27}$ is the package of magnetic moments in a long vector form (9 actuators), and $\mathbf{I} \in \mathbb{R}^9$ is the electric current input. The way to construct the \mathbb{A} matrix is shown in [42].

The actuation matrix could be decomposed using singular value decomposition as

$$\mathbb{A} = \mathbf{U}\mathbf{\Sigma}\mathbf{V}^* \quad (\text{B.2})$$

where \mathbf{U} , \mathbf{V} are unitary matrices, and $\mathbf{\Sigma}$ is the matrix contains singular values. $\mathbf{\Sigma}$ contains the force and torque values, and those values are ordered by the magnitude in orthonormal directions. $\mathbf{\Sigma}$ could be expressed as

$$\mathbf{\Sigma} = \text{diag}(\sigma_1, \sigma_2, \sigma_3, \sigma_4, \sigma_5, \sigma_6). \quad (\text{B.3})$$

Here to increase the force and torque authority, we need to increase σ_3 and σ_6 as they are the weakest force and torque element in a general coordinate. Additionally, we can calculate the electric current to generate a strong magnetic force in the vertical direction as

$$\mathbf{I}_v = \mathbb{A}^{-1}[0, 0, 0, 0, 0, f_z]^\top. \quad (\text{B.4})$$

With these values, we can formulate a fitness function

$$f_i = \alpha\sigma_3 + \beta\sigma_6 + \frac{\gamma}{\|\mathbf{I}_v\|}. \quad (\text{B.5})$$

This fitness function involves maximization of weakest magnetic force and B-field, as well as minimization of electric currents to generate a specific vertical directional force. As this fitness function is calculated in a single point, i , we need to add all values in the workspace. This formulates an optimization problem

$$\begin{aligned} \underset{\mathbf{m}_j}{\text{minimize}} \quad & -\sum_i f_i \\ \text{subject to} \quad & \mathbf{r}_j = \mathbf{r}_{j,\text{given}} \\ & \|\mathbf{m}_j\| = M_j \end{aligned} \quad (\text{B.6})$$

Table B.2: Actuation System Design Parameters

Coil number	Center position (mm)			Magnetic moment (A·m ² /A)		
	x	y	z	m_x	m_y	m_z
1	-130	130	0	6.13	-6.13	56.3
2	0	130	0	0	-40.4	40.2
3	130	130	0	-6.13	-6.13	56.3
4	-130	0	0	40.4	0	40.2
5	0	0	0	0	0	57.0
6	130	0	0	-40.4	0	40.2
7	-130	-130	0	6.13	6.13	56.3
8	0	-130	0	0	40.4	40.2
9	130	-130	0	-6.13	6.13	56.3

where $\mathbf{r}_{j,given}$ is the preset position of the actuators and M_j is the measured magnetic moment of each coil. Table B.2 shows the optimized parameters, which were used as design parameters for the fabrication of the actuation system. We used CAD tools to design the system and fabricated the system using mechanical machining techniques (Fig. B.1).

Appendix C

Design and Fabrication of the Magnetic Sensor Array

The magnetic sensor array is crucial for the localization. The magnetic sensors on the array receive the magnetic field and convert it into values that can be read by a signal processing system. Selection of the magnetic sensors is important because it directly affects the localization quality. Magnetic sensors have different sensing ranges, resolutions, noise levels, and so forth. These values should be chosen carefully to serve the localization task.

A review study on magnetic sensors gives a sensor-selection guideline based on a targeted application [123]. In our case, the magnetic field applied to the magnetic sensors are in the range of $[-2, 2]$ Gauss, and 3-D vector magnetic field measurement is preferred. In this range, the guideline recommends search-coil magnetometer, fluxgate magnetometer, and magnetoresistive magnetometer. The search-coil magnetometer is only useful to AC magnetic field measurements, which are not applicable to our DC magnetic field measurements. The fluxgate magnetometers are not applicable as well. We use multiple magnetic sensors in an array, where the distances between sensors are relatively close to each other. The magnetic fields generated by the fluxgate sensors affect each other in these short distances. This gives magnetic interferences among the sensors, which is very difficult to calibrate. In the end, magnetoresistive

magnetometers are left for our choice.

We used the magnetoresistive sensors in the sensor array (LIS3MDL, STMicroelectronics co.). This sensor gives 17.11 bit/ μ T sensitivity, and 400 nT RMS noise, which was suitable for our localization task. The magnetic field values are read by I2C communication. The distances between nearby sensors were 30 mm. By following the design guideline from the specification sheet of the sensor, a PCB schematic drawing was drawn as in Fig. C.1. In the schematic drawing, a I²C multiplexer was connected to 8 magnetic sensors to manage multiple serial communication signals, and 8 multiplexers were used to connect with 64 magnetic sensors. The capacitors and resistors were chosen based on the guideline as well. Finally, the magnetic sensor arrays were fabricated by a local PCB fabrication vendor (Fig. C.2).

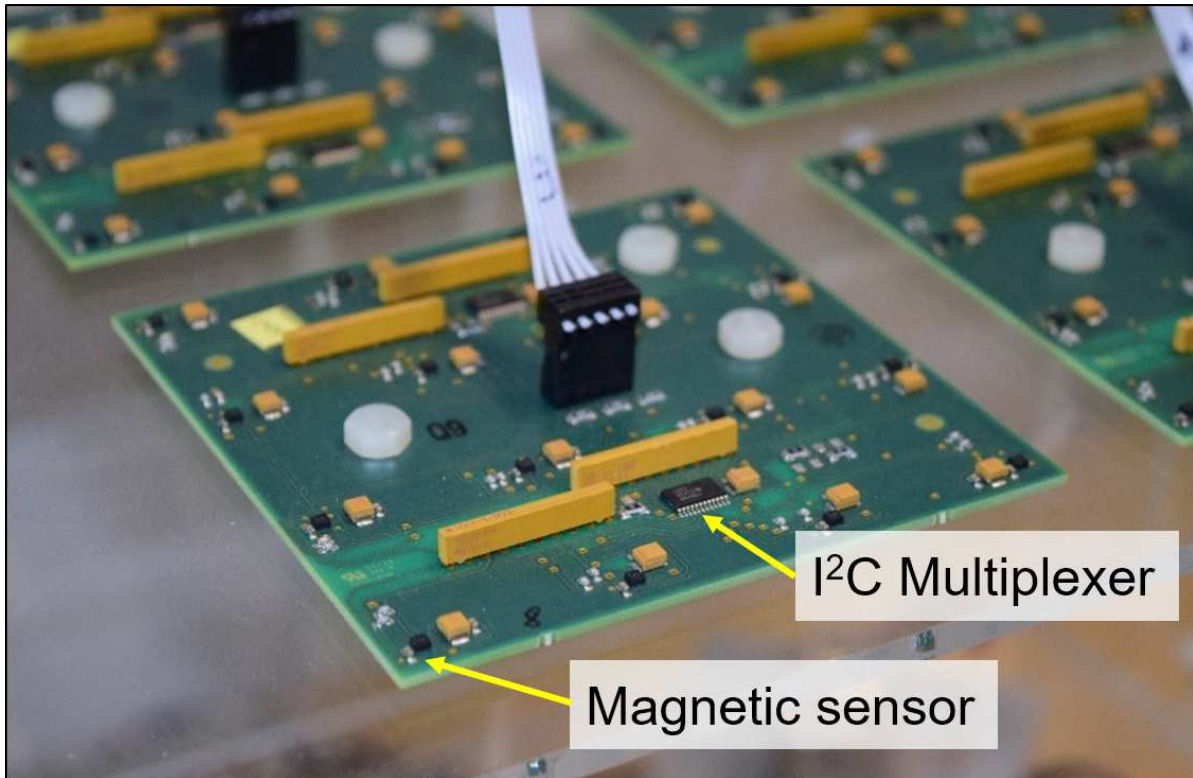


Figure C.2: Fabricated sensor arrays. The magnetic sensors are placed in grids with 30 mm spacings. I²C multiplexers are placed to manage multiple serial-communication signals from the magnetic sensors.

Appendix D

Mechanical Drawing of B-MASCE

This chapter provides the mechanical drawing of B-MASCE. Fig. D.1 shows front, top, ISO, and section views with mechanical dimensions. Function(s) of each part is explained in *Design of B-MASCE* in Chapter 5.

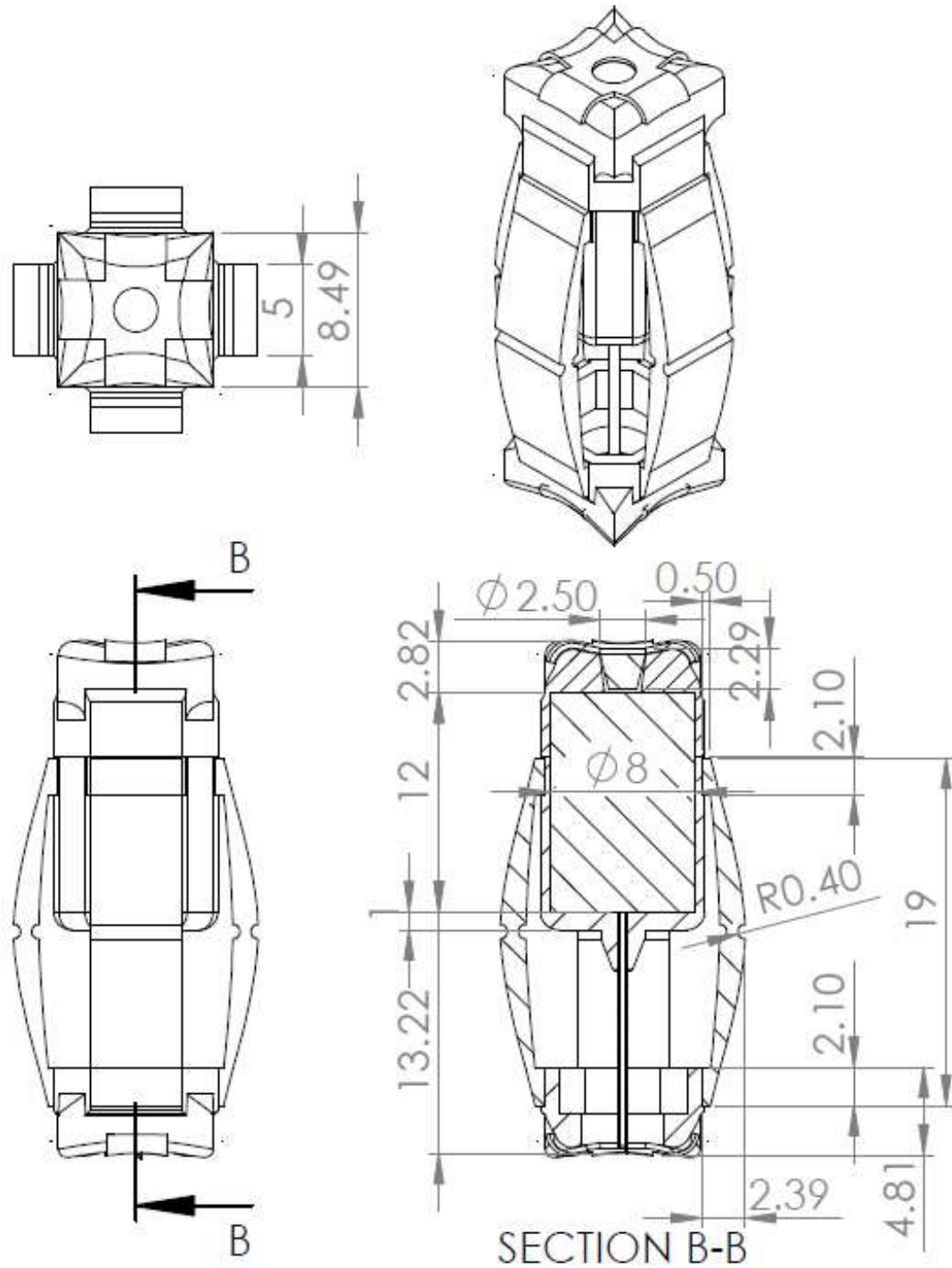


Figure D.1: Mechanical drawing of B-MASCE. Dimensions of B-MASCE are shown in detail. Front, top, ISO view, and the section view are shown.

Appendix E

MatLab Codes for the Localization

Method

This code is to show how the localization method is implemented. This code is designed to run without real measurement data so that a user of this code could test by him/herself. Who wants to use this code in a real application, should replace the "measurement update" part in the code with real measurement data. Comments in the code would help to understand details of the code.

Matlab Code

```
1 function Localization()
2 % System parameters are defined here
3 rj = sensor_positions(); % Details are inside the function
4 ro = zeros(3,1); % Omnimagnet's position
5 M = [30, 0, 0; 0, 30, 0; 0, 0, 30]; % Magnetic moment mapping of
6 % Omnimagnet
7 % Initial conditions
8 m_c = [0;0;1]; % Initial magnetic moment of MASCE
9 r_c = randn(3,1)*0.01; % Initial position of MASCE
10 x_init = [r_c', m_c']; % Initial state vector
11 % x_init = x_init + randn(1,6)*0.01; % Disturb initial position to
    test
12 %the code
13 x_est = x_init; % Make it as a continuously updated variable.
14
15 % Optimizer setting
16 options = optimoptions('lsqnonlin');
```

```

17 options.Algorithm = 'levenberg-marquardt'; % Set to LM algorithm
18
19 % Measurement update
20 Ii = load_electric_currents(); % Current measurements
21 mo = M*Ii; % Omnimagnet's magnetic moment
22 Vc = load_sensor_measurements(rj,r_c,m_c);
23 Vo = load_sensor_measurements(rj,ro,mo);
24 Vj = Vc + Vo;
25 % These two values are estimated measurements
26 % by magnetic field from omnimagnet and the
27 % magnetic capsule. These values should be
28 % replaced by the real measurement in
29 % the desired system.
30
31 % Optimization
32 f = @(x)f_opt(x,rj,Vj,ro,mo); % Create a function handle
33 x_est = lsqnonlin(f,x_est,[],[],options); % Run optimization
34 disp(x_est) % The localization solution.
35 % This should be run in a loop in
36 % real time applications.
37 end
38
39 function f = f_opt(x,rj,Vj,ro,mo)
40 r = x(1:3)'; % position extraction from the state
41 m = x(4:6)'; % magnetic moment extraction from the state
42 H = [0 -1 0; % Laplacian kernel
43      -1 4 -1;
44      0 -1 0];
45
46 V_act_model = [0,0,1]*B_sensor(rj,ro,mo); % B-field by OmniMag
47 V_cap_model = [0,0,1]*B_sensor(rj,r,m); % B-field by MASCE
48
49 V_sub = Vj - V_act_model; % Measured B-field - B-field from OmniMag
50
51 % These two are to change into grid
52 V_sub_grid = reshape(V_sub,8,8);
53 V_cap_model_grid = reshape(V_cap_model,8,8);
54
55 % Laplacian convolution. This calculation is same to Eq. 2.11
56 V_sub_lap = conv2(V_sub_grid, H, 'same');
57 V_cap_lap = conv2(V_cap_model_grid, H, 'same');
58
59 f = norm(V_sub_lap - V_cap_lap,'fro')^2*1e10; % Eq. 2.14.
60 end
61
62

```

```

63 function Bj = B_sensor(rj,ri,m) % Calculated B-field on sensors
64 n = length(rj);
65 Bj = zeros(3,n);
66 for i=1:n
67     r = rj(:,i) - ri;
68     Bj(:,i) = Bmat(r)*m;
69 end
70 end
71
72 % Pseudo code to generate measured B-field
73 function Vj = load_sensor_measurements(rj,ri,m)
74 Vj = [0,0,1]*B_sensor(rj,ri,m);
75 end
76
77 % Pseudo code to generate measured currents
78 function Ii = load_electric_currents()
79 Ii = randn(3,1);
80 end
81
82 % Create sensor position matrix
83 function rj = sensor_positions()
84 dx = 0.01;
85 dy = 0.01;
86 N = 8;
87 z = 0.2;
88 rj = zeros(3,N);
89 i = 0;
90 for y = dy*3.5:-dy:-dy*3.5
91     for x = -dx*3.5:dx:dx*3.5
92         i = i+1;
93         rj(:,i) = [x;y;z];
94     end
95 end
96 end
97
98 % Dipole magnetic mapping matrix which
99 % only deals position. Same as B matrix in eq 3.3
100 function B = Bmat(r)
101 r_size = sqrt(transpose(r)*r);
102 r_hat = r/r_size;
103 B = 3*r_hat*transpose(r_hat)-eye(3);
104 B = 1e-7/r_size^3*B;
105 end

```

Appendix F

MabLAB Codes for the Calibration Method

These codes are to show how the calibration method is implemented. The codes have hierarchical structures. The *main()* function operates all sub-functions, whereas the other functions are employed as sub-functions for the main function or the other sub-functions. The most important codes are *sensor_model(·)* and *BB_Packing(·)*. These construct both sensor and actuation models in Chapter 3. Additionally, *fcn_opt(·)* and *nonlcon(·)* are employed for the nonlinear optimization in *main()*. The details are commented directly to the codes.

Matlab Code

```
1 function main()
2 % Create initial parameters
3 [par, x_init, lb, ub] = init_parame;
4 % Create optimization options
5 options = InitOptim('fmincon');
6 % Run optimization
7 x = fmincon(@(x) fcn_opt(x, par), x_init, [], [], [], [], lb, ub, @(x)
    ) nonlcon(x, par), options);
8 cf = ArrayToConfig(x, par);
9
10 % Save all data
11 save('result.mat');
12 end
13
```

```

14 function options = InitOptim(A) % These set the optimization
    conditions.
15 options = optimoptions(A);
16 options.Display = 'iter';
17 options.MaxFunctionEvaluations= 1e10;
18 options.OptimalityTolerance= (1e-7*1e4)^2;
19 options.StepTolerance = 1e-4;
20 options.MaxIter= 1e3;
21 options.UseParallel = 1;
22 end

1 function f = fcn_opt(x,par) % This is the fitness function.
2 cf = ArrayToConfig(x,par); % Parameter vector to configurations.
3 n_a = size(cf.xj,2);
4
5 % Construct magnetic moment matrix. Eq 3.4, M matrix
6 MM = zeros(3*n_a,n_a);
7 for i=1:n_a
8     MM(3*i-2:3*i,i) = cf.xj(4:6,i);
9 end
10
11 % Recover magnetic fields from sensor measurements
12 % We use Gauss level in the calculations to avoid numerical problems.
13 VV = sensor_model(par.VV,cf.Gi,cf.Hi);
14 BB = BB_Packing(par.ri,cf.rj)*1e-3;
15
16 % Eq. 3.6
17 f = norm(VV-BB*MM*par.II,'fro');
18 end

1 function [c,ceq] = nonlcon(x,par) % This is g() in Eq. 3.6
2 cf = ArrayToConfig(x,par);
3 l = size(par.ri,2);
4 ceq(1) = (norm(cf.Gi,'fro')^2/3/l - 1)^2;
5 c = [];
6 end

1 function [cf,par] = generate_configurations()
2 par.mu0 = 4*pi*1e-7; % Permeability of free space
3 cf.xi = make_true_parameters; % This gives a proper initial
    condition
4 par.ri = cf.xi(1:3,:); % Sensors' position are excluded in the
    parameters to be optimized
5 cf.xi(1:3,:) = [];
6 rj = load('rj.txt'); % Initial positions of actuators
7 mj= load('zj.txt'); % Orientation of the actautors in a vector
    form

```



```

8 cf.xj = [rj;mj*40];      % Put all actuator information in a single
    configuration.

1 function par = generate_system_parameters()
2 % magnetics
3 par.mu0 = 4*pi*1e-7;
4 end

1 function cf = ArrayToConfig(x,par)
2 xi = x(1:par.index_param(1));
3 xj = x(par.index_param(1)+1 : par.index_param(2));
4
5 % reshaping
6 l = size(par.ri,2);
7 cf.xi= reshape(xi,[],l);
8 cf.xj = reshape(xj,[],9);
9
10 cf.Gi = cf.xi(1:9,:);
11 cf.Hi = cf.xi(10:27,:);
12
13 cf.rj = cf.xj(1:3,:);
14 cf.mj = cf.xj(4:6,:);

1 function BB = BB_Packing(ri,rj) % This is the B matrix in Eq. 3.4
2 n_s = size(ri,2);
3 n_a = size(rj,2);
4
5 BB = zeros(3*n_s,3*n_a);
6
7 for i_s=1:n_s      % Row: sensor index
8
9     r_s = ri(:,i_s);
10
11     for i_a = 1:n_a % column : actuator index
12
13         r_a = rj(:,i_a);
14
15         p = r_s-r_a;
16
17         x = p(1);
18         y = p(2);
19         z = p(3);
20
21         r = sqrt(x^2+y^2+z^2);
22         x = x/r;
23         y = y/r;
24         z = z/r;

```

```

25
26     P = [3*x^2 - 1,      3*x*y,      3*x*z;
27           3*x*y, 3*y^2 - 1,      3*y*z;
28           3*x*z,      3*y*z, 3*z^2 - 1];
29
30     P = P/r^3;
31
32     BB(3*i_s-2:3*i_s,3*i_a-2:3*i_a) = P;
33
34
35     end
36 end
37 end

1 function [x,par] = ConfigToArray(cf,par,mode)
2 % These values are to generate box constraints for the optimizer
3 [m,n] = size(cf.xi(1:3,:));
4 xi_norm = sqrt(norm(cf.xi(1:3,:), 'fro')^2/m/n);
5 [m,n] = size(cf.xj);
6 rj_norm = sqrt(norm(cf.xj(1:3,:), 'fro')^2/m/n);
7 mj_norm = 40;
8
9 % Set the tolerance. We used 2% from the initial guess.
10 PE = 0.02;
11
12 if mode == 3 % This generates the upper boundary constraint.
13     cf.xi(1:9,:) = cf.xi(1:9,:) + 0.05;
14     cf.xi(10:27,:) = cf.xi(10:27,:) + 0.05;
15     cf.xj(1:3,:) = cf.xj(1:3,:) + 1;
16     cf.xj(4:6,:) = cf.xj(4:6,:) + 40;
17 elseif mode ==4 % This generates the lower boundary constraint.
18     cf.xi(1:9,:) = cf.xi(1:9,:) - 0.05;
19     cf.xi(10:27,:) = cf.xi(10:27,:) - 0.05;
20     cf.xj(1:3,:) = cf.xj(1:3,:) - 1;
21     cf.xj(4:6,:) = cf.xj(4:6,:) - 40;
22 end
23
24 % This value is used to scale magnetic moments. This is only to avoid
25 % numerical problems.
26 par.s_mj = 40;
27
28 % pack into an array
29 xi = reshape(cf.xi,1,[]);
30 xj = reshape(cf.xj,1,[]);
31
32 x = [xi,xj];
33 lengthV = [length(xi), length(xj)];

```

```

34 par.index_param = cumsum(lengthV); % This value is used to recover
    the configurations from the array shape of parameters.
35 return;

1 function [par, x_init, x_lb, x_ub] = init_parame()
2 [cf,par] = generate_configurations(); % System configurations
3 par = load_measurement_data(par); % Import measurement data
4
5 % This is needed because optimizers only uses a vector. This places
    all
6 % configuration into a single vector
7
8 % This generates initial condition
9 [x_init,par] = ConfigToArray(cf,par,1);
10
11 % These two generate optimization boundaries
12 [x_ub,par] = ConfigToArray(cf,par,3);
13 [x_lb,par] = ConfigToArray(cf,par,4);
14 end

1 function par = load_measurement_data(par)
2 % Import measured data
3 % B-field measurements are imported in a matrix form.
4 % Row: sensor number, Column: number of measurement
5 % In this version we used gauss level in all codes.
6 par.VV = load('Bfield_set.txt');
7
8 % Electric current measurement.
9 % Row: coil number, Column: number of measurement.
10 % In this version, we used Ampere as the unit
11 par.II = load('Current_set.txt');
12
13 [~,n_i] = size(par.II);
14 par.n_i = n_i;
15 end

1 function xi_init = make_true_parameters
2
3 % Below generates sensors' positions
4 i = 0;
5 for y = 10.5:-3:-10.5
6     for x = -10.5:3:10.5
7         z = 25;
8         i = i+1;
9         ri(:,i) = [x;y;z]/100; %convert from cm to m
10     end
11 end

```

```

12
13 % Below generates initial sensor gains as 1s.
14 l = size(ri,2);
15 xi_init = zeros(30,1);
16 for i=1:l
17     Gi = reshape(eye(3), [],1);
18     Hi = zeros(18,1);
19     xi_init(:,i) = [ri(:,i);Gi;Hi];
20 end

1 function VV = sensor_model(VV_measured,Gi,Hi) % This is the sensor
   model in Eq 3.1 & 3.2
2 [n_s,n_i] = size(VV_measured);
3 NN = zeros(n_s);
4 VV_quad = zeros(size(VV_measured));
5
6 for i=1:n_s/3
7     NN(3*i-2:3*i,3*i-2:3*i) = reshape(Gi(:,i),3,[])' ;
8
9     mx = Hi(1:6,i);
10    my = Hi(7:12,i);
11    mz = Hi(13:18,i);
12
13    V_dummy = VV_measured(3*i-2:3*i,:);
14    V_quad_x = zeros(1,n_i);
15    V_quad_y = zeros(1,n_i);
16    V_quad_z = zeros(1,n_i);
17
18    V_vec = zeros(1,6);
19    for j=1:n_i
20        V = V_dummy(:,j);
21        V_vec(1) = V(1)^2;
22        V_vec(2) = V(2)^2;
23        V_vec(3) = V(3)^2;
24        V_vec(4) = V(1)*V(2);
25        V_vec(5) = V(1)*V(3);
26        V_vec(6) = V(2)*V(3);
27        V_quad_x(j) = V_vec(1)*mx(1) + V_vec(2)*mx(2) + V_vec(3)*mx
           (3) + V_vec(4)*mx(4)+ V_vec(5)*mx(5)+ V_vec(6)*mx(6);
28        V_quad_y(j) = V_vec(1)*my(1) + V_vec(2)*my(2) + V_vec(3)*my
           (3) + V_vec(4)*my(4)+ V_vec(5)*my(5)+ V_vec(6)*my(6);
29        V_quad_z(j) = V_vec(1)*mz(1) + V_vec(2)*mz(2) + V_vec(3)*mz
           (3) + V_vec(4)*mz(4)+ V_vec(5)*mz(5)+ V_vec(6)*mz(6);
30    end
31
32    VV_quad(3*i-2:3*i,:) = [V_quad_x;V_quad_y;V_quad_z];
33

```

```
34 end
35 VV = NN * VV_measured + VV_quad;
```

Appendix G

MabLAB Codes for the Control Methods

These codes show how the control methods are implemented. The codes use the calibration matrices from the calibration method. There are three different controllers, and their codes are built separately. These codes should be embedded in a real-time environment, where the parameters from the system are passed through these codes. Those parameters are the localization data of the master and slave MASCEs, and basic system constraints, such as sensor saturation limits. These codes should run individually, and when the robot changes its control mode, then the code should be also shifted from one to another.

Matlab Code for Orientation Controller

```
1 function II = rolling_controller(x_m,x_s,og,BB,GG,e_pid,rj,MM,  
    magnetic_moment,options,BM_sat)  
2 % x_m: master's state  
3 % x_s: slave's state  
4 % og: orientation gain: usually 3 mT  
5 % BB, MM: B-field actuation matrices  
6 % e_pid: error in PI gain form  
7 % rj: position of the coils  
8 % magnetic_moment: magnetic moment of the magnetic robots  
9 % options: optimization options  
10 % BM_sat: sensor saturation limits  
11  
12  
13 % Define current state
```

```

14 rt = transpose(x_s(1:3));
15 mt = transpose(x_s(4:6));
16 nt = mt/norm(mt);
17
18 % Desired state
19 m_des = transpose(x_m(4:6));
20 n_des = m_des/norm(m_des);
21 m_des = n_des * magnetic_moment;
22
23 % Local coordinate of at the desired angle
24 if norm(e_pid)<0.001
25     R_pid = eye(3);
26 else
27     n_e_pid = e_pid/norm(e_pid);
28     theta = norm(e_pid);
29     R_pid = Rmat(n_e_pid*theta);    %Maps {G} --> {L}
30 end
31
32 % Gravity compensation field
33 if n_des(3)>0
34     B_comp = 1.5*[0;0;1];
35 else
36     B_comp = [0;0;0];
37 end
38
39 n_des = n_des*og + B_comp;
40 n_des = n_des/norm(n_des);
41
42 n_des = R_pid*n_des;
43 z_L = n_des/norm(n_des);
44 z_G = [0;0;1];
45
46 ksi = cross(z_L,z_G);
47 if norm(ksi)<0.001
48     R = eye(3);
49 else
50     ksi = ksi/norm(ksi);
51     theta = acos(n_des'*z_G);
52     R = Rmat(ksi*theta);    %Maps {G} --> {L}
53 end
54
55 % Mappings
56 BM_G = BB*MM*1e-4;    % BM matrix in the global coordi. in mT
57 GM = GG*MM*1e-4;    % Gradient matrix
58 BM = R*BM_G;    % BM matrix in the local coordi.
59 HM = HH_Packing_unit_amp(nt,rt,rj,MM)*1e3;    % unit in mT

```

```

60
61 preF = [m_des(1), 0,0,m_des(2), m_des(3),0;      % Prefix for force
        matrix
62     0, m_des(2),0,m_des(1),0, m_des(3);
63     0, 0, m_des(3), 0, m_des(1), m_des(2)];
64
65 FM = preF*GM;
66 BM_sat = BM_sat/10; % in mT
67
68 % Constraints
69 % Equality constraints
70 Aeq = [BM(1:2,:);FM(1:2,:)];
71 beq = zeros(4,1);
72
73 % Inequality constraints
74 B_sat = ones(192,1)*1.58;
75 g_max = 10*ones(6,1);
76
77 A = [-BM(3,:);
78     GM;
79     -GM;
80     BM_sat
81     -BM_sat];
82 b = [-og;
83     g_max;
84     g_max;
85     B_sat
86     B_sat];
87
88 % Boundary constraint
89 lb = -ones(1,9)*1.8;
90 ub = +ones(1,9)*1.8;
91
92 % Initial guess value
93 II = transpose(pinv([BM;FM(1:2,:)])*[0;0;2;0;0]);
94
95 % Run optimizer
96 II = fminimax(@(II) fcn_opt_rolling(II,HM),II,A,b,Aeq,beq,lb,ub,@(II)
    nonlcon(II,HM),options);
97 end

1 function out = fcn_opt_rolling(II,HM)
2 hV = HM*transpose(II);
3 hM = reshape(hV,5,5);
4 [~,v,~] = svd(hM);
5 hessian_curv2 = max(max(v));
6 % out = hessian_curv2 ;

```



```

7 out = norm(II)*2 + hessian_curv2/500 ;
8 end

1 function [c,ceq] = nonlcon(II,HM)
2 ceq = [];
3 hV = HM*transpose(II);
4 hM = reshape(hV,5,5);
5 eigV = eig(hM);
6 eigV(eigV.^2 < 1e-8) = [];
7 hessian_curv1 = min(eigV)/.5;
8 c = -hessian_curv1;
9 end

```

Matlab Code for Tumor Anchoring Controller

```

1 function II = tumor_anchoring_controller(x_m,x_s,og,BB,GG,e_pid,rj,
    MM,magnetic_moment,options)
2 % Input parameters are same as orientation/rolling controller
3
4 % desired state
5 r_des = transpose(x_m(1:3));
6 m_des = transpose(x_m(4:6));
7 n_des = m_des/norm(m_des);
8 m_des = n_des * magnetic_moment;
9
10 % local coordinate of at the desired angle
11 n_des = Rmat(e_pid)*n_des;
12 z_L = n_des/norm(n_des);
13 z_G = [0;0;1];
14
15 ksi = cross(z_L,z_G);
16 if norm(ksi)<0.001
17     R = eye(3);
18 else
19     ksi = ksi/norm(ksi);
20     theta = acos(n_des'*z_G);
21     R = Rmat(ksi*theta); %Maps {G} --> {L}
22 end
23
24 % Mappings
25 BM_G = BB*MM*1e-4; % BM matrix in the global coordi. in mT
26 GM = GG*MM*1e-4; % gradient matrix
27 BM = R*BM_G; % BM matrix in the local coordi.
28 HM = HH_Packing_unit_amp(m_des,r_des,rj,MM)*1e3; % unit in mT
29
30 preF = [m_des(1), 0,0,m_des(2), m_des(3),0; % prefix for force
    matrix

```

```

31     0, m_des(2), 0, m_des(1), 0, m_des(3);
32     0, 0, m_des(3), 0, m_des(1), m_des(2)];
33
34 FM = preF*GM;
35
36 % constraints
37 % equality constraints
38 Aeq = [BM(1:2,:);FM(1:2,:)];
39 beq = zeros(4,1);
40
41 % inequality constraints
42 g_max = 250*ones(6,1)*abs(n_des(3));
43
44 A = [-BM(3,:);
45      GM
46      -GM];
47 b = [-og;
48      g_max;
49      g_max;];
50
51
52
53 % boundary constraint
54 lb = -ones(1,9)*3;
55 ub = -lb;
56
57 % initial guess value
58
59 II = transpose(pinv([BM;FM(1:2,:)])*[0;0;2;0;0]);
60
61 % run optimizer
62 II = fminimax(@ (II) fcn_opt_climb(II,HM), II,A,b,Aeq,beq,lb,ub,[],
63              options);
64
65 end

```

```

1 function out = fcn_opt_anchor(II,HM)
2
3 hV = HM*transpose(II);
4 hM = reshape(hV,5,5);
5
6 eigV = eig(hM);
7 eigV(eigV.^2 < 1e-8) = [];
8 hessian_curv1 = min(eigV)/.5;
9
10 out = -hessian_curv1 ;

```

```

11 end

1 function HH = HH_Packing_unit_amp(mt,rt,rj,MM)
2 % reshape the actuation matrix
3 n_a = size(rj,2);
4 n_coil = size(MM,2);
5 n_dipole = n_a/n_coil;
6 mj = zeros(9,n_coil);
7
8 %
9 HH = zeros(25,n_coil);
10
11 for i=1:n_coil
12     mj(:,i) = MM(3*(i-1)*n_dipole + 1 : 3*(i-1)*n_dipole + 9, i );
13 end
14
15 for i_c = 1:n_coil % column : actuator index, n-th coil is running
16
17     hV_i_c = zeros(25,1);
18     for i_d = 1:n_dipole
19         idx = n_dipole*(i_c-1) + i_d;
20         r_a = rj(:,idx);
21         m_a = mj(3*i_d-2:3*i_d,i_c);
22         r = rt - r_a;
23         [~,hV] = E_hessian(mt,r,m_a);
24         hV_i_c = hV_i_c + hV;
25     end
26
27     HH(:, i_c) = hV_i_c;
28 end

1 function [H_E,H_V] = E_hessian(nt,rt,ma)
2 % nt is unit vector. The value can be multiplied by magnetic moment,
   but we
3 % negelect here because we only check the sign of eigen values.
4 % all inputs are in a column vector format.
5
6 Bg = B_gradient(rt,ma);
7 dBdx = Bg(:,1);
8 dBdy = Bg(:,2);
9
10 Bh = B_hessian(rt,ma);
11 dBdxx = Bh(:,1);
12 dBdyy = Bh(:,2);
13 dBdxy = Bh(:,3);
14
15 B = Bmat(rt)*ma;

```

```

16
17 H11 = (transpose(nt)*B)*eye(3) - nt*transpose(B);
18 H12 = -cross(nt,dBdx);
19 H13 = -cross(nt,dBdy);
20 H22 = -transpose(nt)*dBdxx;
21 H33 = -transpose(nt)*dBdyy;
22 H23 = -transpose(nt)*dBdxy;
23
24 H_E = [H11, H12, H13;
25        H12', H22, H23;
26        H13', H23', H33];
27
28 H_V = reshape(H_E,[],1);
29
30 % The output values are hessian over parameter sets (nt, x, y). nt is
    the
31 % unit vector directing to the desired orientation of the robot.
32
33
34 end

```

Matlab Code for Collapsing Controller

```

1 function [II,f_exp,b_exp,flag] = main_force(x_s,MM,rj)
2 % magnetic moment calculation
3 % V = pi * (8e-3/2)^2 * 12e-3;
4 % magnetic_moment = 1.43*V/(4*pi*1e-7);
5 % weight calculation
6 % density = 7.5*1e-3/1e-6;
7 % mass = V*density;
8 magnetic_moment = 0.6864;
9
10 %% states
11 nt_des = [0;0;1];
12 rt_m = transpose(x_s(1:3));
13 nt = transpose(x_s(4:6));
14 nt = nt/norm(nt);
15 rt = rt_m - nt_des * 0.01;
16 mt_des = magnetic_moment * nt_des;
17
18 %% Local coordi
19 z = [0;0;1];
20 screw = cross(z,nt);
21 n_screw = norm(screw);
22 if n_screw<0.01
23     R = eye(3);

```

```

24 else
25     screw = screw/norm(screw);
26     th = acos(transpose(nt)*z);
27     so3 = skew(screw*th);
28     R = expm(so3);
29 end
30
31 % calculate BM,FM based on the collapse center
32 BM = R' * BB_Packing(rt,rj)*MM*1e3; % mT * Am2
33 FM = R' * FF_Packing(rt,mt_des,rj)*MM*1e3; % mN
34 HM = HH_Packing(mt_des,rt,rj)*MM*1e3; % mN/m
35
36 BM_xy = BM(1:2,:);
37 FM_xy = FM(1:2,:);
38 %% Conditions
39 Aeq = [BM_xy;FM_xy];
40 beq = [[0;0];[0;0]];
41 % Minimu force and B-field condition
42 A = [FM(3,:); -FM(3,:); -BM(3,:)];
43 b = [-500; 800; -30];
44
45 % Initial condition
46 f_norm = 600; % mN
47 f_des = -nt_des*f_norm;
48 B_des = 40*nt_des; % 3 mT
49 II = pinv([BM;FM]) * [B_des;f_des];
50
51 % System constraints
52 ub(1) = 5.8;
53 ub(3) = 5.8;
54 ub(7) = 5.8;
55 ub(9) = 5.8;
56 ub(2) = 10;
57 ub(4) = 10;
58 ub(6) = 10;
59 ub(8) = 10;
60 ub(5) = 10;
61
62 lb = -ub;
63
64 options = optimoptions('fmincon');
65 options.MaxFunctionEvaluations = 200000;
66 options.ConstraintTolerance = 1;
67 options.MaxIterations = 500;
68
69 [II,~,flag] = fmincon(@(II) fcn_opt_force(II,FM,nt,HM,BM),transpose(II

```

```

        ),A,b,Aeq,beq,lb,ub,[],options);
70 II = transpose(II);
71 f_exp = FM*II;
72 b_exp = BM*II;
73
74 end

1 function out = fcn_opt_force(X,FM,HM,BM)
2 II = transpose(X(1:9));
3
4 f = FM(3,:)*II;
5 b = BM(3,:)*II;
6
7 hV = HM*II;
8 HM = [hV(1), hV(2), hV(3), hV(4);
9       hV(2), hV(5), hV(6), hV(7);
10      hV(3), hV(6), hV(8), hV(9);
11      hV(4), hV(7), hV(9), hV(10)];
12
13 out = -min(eig(HM(3:4,3:4)))/4e3 - min(eig(HM(1:2,1:2)))/1 + f/40 -b
      /0.1 ;
14 end

1 function FF = FF_Packing(rt,mt,rj)
2 rt = reshape(rt,[],1);
3 mt = reshape(mt,[],1);
4
5
6 n_a = size(rj,2);
7 FF = zeros(3,3*n_a);
8 % mu = 4*pi*1e-7;
9 for i_a = 1:n_a % column : actuator index
10
11     r_a = rj(:,i_a);
12
13     p = rt-r_a;
14
15     FF(:,3*i_a-2:3*i_a) = Fmat(mt,p);
16 end
17 end

1 function HH = HH_Packing(mt,rt,rj)
2
3 n_a = size(rj,2);
4
5 HH = zeros(10,3*n_a);
6

```

```

7  for i_a = 1:n_a % column : actuator index
8
9      r_a = rj(:,i_a);
10
11     r = rt - r_a;
12
13     H = hessian_En(mt,r);
14
15     HH(:, 3*i_a-2:3*i_a) = H;
16
17
18 end

1  function F = Fmat(mt,p)
2  p_size = sqrt(transpose(p)*p);
3  p_hat = p/p_size; % mi is target magnetic moment, mj is
   actuation magnetic moment
4  p_hat_t = transpose(p_hat);
5
6  F = mt*p_hat_t + p_hat*transpose(mt) + (p_hat_t*mt)*(eye(3) - 5*(
   p_hat*p_hat_t) );
7  F = F/p_size^4;
8  end

```

Bibliography

- [1] G. Berci and K. A. Forde, “History of endoscopy: What lessons have we learned from the past?,” *Surgical Endoscopy*, vol. 14, no. 1, pp. 5–15, 2000. 1.1
- [2] W. C. Leung, D. C. Foo, T. Chan, M. Chiang, A. H. Lam, H. H. Chan, and C. C. Cheung, “Alternatives to colonoscopy for population-wide colorectal cancer screening,” *Hong Kong Medical Journal*, vol. 22, no. 1, pp. 70–77, 2016. 1.1
- [3] P. Iddan, Gavriel and Meron, Gavriel and Glukhovsky, Arkady and Swain, “Wireless capsule endoscopy,” *Nature*, vol. 405, no. May, pp. 417–418, 2000. 1.1
- [4] M. F. Hale, R. Sidhu, M. E. Mcalindon, M. F. Hale, R. Sidhu, M. E. Mcalindon, R. H. Hospital, and S. Sheffield, “Capsule endoscopy: Current practice and future directions,” *World journal of gastroenterology*, vol. 20, no. 24, pp. 7752–7759, 2014. 1.1
- [5] A. Koulaouzidis, D. K. Iakovidis, A. Karargyris, and E. Rondonotti, “Wireless endoscopy in 2020: Will it still be a capsule?,” *World Journal of Gastroenterology*, vol. 21, no. 17, pp. 5119–5130, 2015. 1.1
- [6] C. Gheorghe, R. Iacob, and I. Bancila, “Olympus capsule endoscopy for small bowel examination,” *Journal of Gastrointestinal and Liver Diseases*, vol. 16, no. 3, pp. 309–313, 2007. 1.2.1
- [7] B. F. Mustafa, “Small bowel video capsule endoscopy : an overview,” *Expert review of gastroenterology & hepatology*, vol. 7, no. 4, pp. 323–329, 2013. 1.2.1
- [8] M. Rahman, S. Akerman, B. DeVito, L. Miller, M. Akerman, and K. Sultan, “Comparison of the diagnostic yield and outcomes between standard 8 h capsule endoscopy and the new 12 h capsule endoscopy for investigating small bowel pathology,” *World Journal of Gastroenterology: WJG*, vol. 21, no. 18, p. 5542, 2015. 1.2.1
- [9] D. K. Iakovidis, S. Tsevas, and A. Polydorou, “Reduction of capsule endoscopy reading times by unsupervised image mining,” *Computerized Medical Imaging and Graphics*, vol. 34, no. 6, pp. 471–478, 2010. 1.2.1
- [10] D. M. Sears, A. Avots-Avotins, K. Culp, and M. W. Gavin, “Frequency and clinical outcome of capsule retention during capsule endoscopy for gi bleeding of obscure origin,” *Gastrointestinal endoscopy*, vol. 60, no. 5, pp. 822–827, 2004. 1.2.1
- [11] A.-M. Singeap, “Capsule endoscopy: The road ahead,” *World Journal of Gastroenterology*, vol. 22, no. 1, p. 369, 2016. 1.2.1
- [12] B. Kim, S. Lee, J. H. Park, and J.-O. Park, “Design and fabrication of a locomotive mech-

- anism for capsule-type endoscopes using shape memory alloys (smas),” *Mechatronics, IEEE/ASME Transactions on*, vol. 10, no. 1, pp. 77–86, 2005. 1.2, 1.2.2
- [13] M. Quirini, R. J. Webster III, A. Menciassi, and P. Dario, “Design of a pill-sized 12-legged endoscopic capsule robot,” in *Robotics and Automation, 2007 IEEE International Conference on*, pp. 1856–1862, IEEE, 2007. 1.2, 1.2.2
 - [14] M. Quirini, A. Menciassi, S. Scapellato, C. Stefanini, and P. Dario, “Design and fabrication of a motor legged capsule for the active exploration of the gastrointestinal tract,” *IEEE/ASME transactions on mechatronics*, vol. 13, no. 2, pp. 169–179, 2008. 1.2.2
 - [15] P. Valdastri, R. J. Webster III, C. Quaglia, M. Quirini, A. Menciassi, and P. Dario, “A new mechanism for mesoscale legged locomotion in compliant tubular environments,” *IEEE Transactions on Robotics*, vol. 25, no. 5, pp. 1047–1057, 2009. 1.2.2
 - [16] H. Park, S. Park, E. Yoon, B. Kim, J. Park, and S. Park, “Paddling based microrobot for capsule endoscopes,” in *Robotics and Automation, 2007 IEEE International Conference on*, pp. 3377–3382, IEEE, 2007. 1.2, 1.2.2
 - [17] K. Wang, G. Yan, G. Ma, and D. Ye, “An earthworm-like robotic endoscope system for human intestine: design, analysis, and experiment,” *Annals of Biomedical Engineering*, vol. 37, no. 1, pp. 210–221, 2009. 1.2.2
 - [18] L. Phee, D. Accoto, A. Menciassi, C. Stefanini, M. C. Carrozza, and P. Dario, “Analysis and development of locomotion devices for the gastrointestinal tract,” *Biomedical Engineering, IEEE Transactions on*, vol. 49, no. 6, pp. 613–616, 2002. 1.2.2
 - [19] P. Dario and C. Mosse, “Review of locomotion techniques for robotic colonoscopy,” in *Robotics and Automation, 2003. Proceedings. ICRA’03. IEEE International Conference on*, vol. 1, pp. 1086–1091, IEEE, 2003. 1.2.2
 - [20] I. De Falco, G. Tortora, P. Dario, and A. Menciassi, “An integrated system for wireless capsule endoscopy in a liquid-distended stomach,” *IEEE transactions on bio-medical engineering*, vol. 61, pp. 794–804, Mar. 2014. 1.2, 1.2.2
 - [21] G. Tortora, P. Valdastri, E. Susilo, A. Menciassi, P. Dario, F. Rieber, and M. O. Schurr, “Propeller-based wireless device for active capsular endoscopy in the gastric district,” *Minimally Invasive Therapy & Allied Technologies*, vol. 18, no. 5, pp. 280–290, 2009. 1.2.2
 - [22] M. Sendoh, K. Ishiyama, and K.-I. Arai, “Fabrication of magnetic actuator for use in a capsule endoscope,” *IEEE Transactions on Magnetics*, vol. 39, pp. 3232–3234, Sept. 2003. 1.2.3
 - [23] G. Ciuti, P. Valdastri, A. Menciassi, and P. Dario, “Robotic magnetic steering and locomotion of capsule endoscope for diagnostic and surgical endoluminal procedures,” *Robotica*, vol. 28, pp. 199–207, Oct. 2009. 1.2.3
 - [24] B. J. Nelson, I. K. Kaliakatsos, and J. J. Abbott, “Microrobots for minimally invasive medicine,” *Annual Review of Biomedical Engineering*, vol. 12, pp. 55–85, Aug. 2010. 1.2.3
 - [25] J. L. Toennies, G. Tortora, M. Simi, P. Valdastri, and R. J. Webster, “Swallowable medical

- devices for diagnosis and surgery: the state of the art,” *Proceedings of the Institution of Mechanical Engineers, Part C: Journal of Mechanical Engineering Science*, vol. 224, pp. 1397–1414, Jan. 2010. 1.2.3
- [26] A. W. Mahoney and J. J. Abbott, “Five-degree-of-freedom manipulation of an untethered magnetic device in fluid using a single permanent magnet with application in stomach capsule endoscopy,” *The International Journal of Robotics Research*, vol. 35, no. 1–3, pp. 129–147, 2016. 1.2.3, 1.3
- [27] T. D. Than, G. Alici, H. Zhou, and W. Li, “A review of localization systems for robotic endoscopic capsules,” *IEEE Transactions on Bio-medical Engineering*, vol. 59, pp. 2387–99, Sept. 2012. 1.2.3, 2.1
- [28] M. Sitti, H. Ceylan, W. Hu, J. Giltinan, M. Turan, S. Yim, and E. Diller, “Biomedical applications of untethered mobile milli/microrobots,” *Proceedings of the IEEE*, vol. 103, no. 2, pp. 205–224, 2015. 1.2.3
- [29] A. J. Petruska, A. W. Mahoney, and J. J. Abbott, “Remote Manipulation With a Stationary Computer-Controlled Magnetic Dipole Source,” *IEEE Transactions on Robotics*, vol. 30, no. 5, pp. 1222–1227, 2014. 1.2.3
- [30] J.-S. Lee, B. Kim, and Y.-S. Hong, “A flexible chain-based screw propeller for capsule endoscopes,” *International Journal of Precision Engineering and Manufacturing*, vol. 10, pp. 27–34, Oct. 2009. 1.2.3
- [31] F. Carpi, N. Kastelein, M. Talcott, and C. Pappone, “Magnetically controllable gastrointestinal steering of video capsules,” *IEEE Transactions on Bio-medical Engineering*, vol. 58, pp. 231–4, Feb. 2011. 1.2.3, 1.3
- [32] M. Simi, P. Valdastrì, C. Quaglia, a. Menciassi, and P. Dario, “Design, Fabrication, and Testing of a Capsule With Hybrid Locomotion for Gastrointestinal Tract Exploration,” *IEEE/ASME Transactions on Mechatronics*, vol. 15, pp. 170–180, Apr. 2010. 1.2.3, 1.3
- [33] S. Yim and M. Sitti, “Design and rolling locomotion of a magnetically actuated soft capsule endoscope,” *IEEE Transactions on Robotics*, vol. 28, no. 1, pp. 183–194, 2012. 1.2.3, 1.3, 1.3, 5.2.2, 5.3.2, 5.3.3
- [34] S. Yim, E. Gultepe, D. Gracias, and M. Sitti, “Biopsy using a magnetic capsule endoscope carrying, releasing and retrieving untethered micro-grippers,” *IEEE Transactions on Biomedical Engineering*, vol. 61, no. 2, pp. 513–521, 2014. 1.2.3, 1.3
- [35] S. Yim and M. Sitti, “Shape-programmable soft capsule robots for semi-implantable drug delivery,” *IEEE Transactions on Robotics*, vol. 28, pp. 1198–1202, Oct. 2012. 1.2.3, 1.3, 5.3.2
- [36] S. Yim, K. Goyal, and M. Sitti, “Magnetically actuated soft capsule with the multimodal drug release function,” *IEEE transactions on Mechatronics*, vol. 18, no. 4, pp. 1413–1418, 2013. 1.2.3, 1.3, 5.3.2
- [37] G. Ciuti, R. Donlin, P. Valdastrì, A. Arezzo, A. Menciassi, M. Morino, and P. Dario, “Robotic versus manual control in magnetic steering of an endoscopic capsule,” *Endoscopy*, vol. 42, no. 02, pp. 148–152, 2010. 1.2.3

- [38] G. Ciuti, P. Valdastri, A. Menciassi, and P. Dario, "Robotic magnetic steering and locomotion of capsule endoscope for diagnostic and surgical endoluminal procedures," *Robotica*, vol. 28, no. 2, pp. 199–207, 2010. 1.2.3
- [39] A. Arezzo, A. Menciassi, P. Valdastri, G. Ciuti, G. Lucarini, M. Salerno, C. Di Natali, M. Verra, P. Dario, and M. Morino, "Experimental assessment of a novel robotically-driven endoscopic capsule compared to traditional colonoscopy," *Digestive and Liver Disease*, vol. 45, no. 8, pp. 657–662, 2013. 1.2.3
- [40] J.-F. Rey, H. Ogata, N. Hosoe, K. Ohtsuka, N. Ogata, K. Ikeda, H. Aihara, I. Pangtay, T. Hibi, S.-E. Kudo, *et al.*, "Blinded nonrandomized comparative study of gastric examination with a magnetically guided capsule endoscope and standard videoendoscope," *Gastrointestinal endoscopy*, vol. 75, no. 2, pp. 373–381, 2012. 1.2.3, 1.3
- [41] A. J. Petruska and J. J. Abbott, "Omnimagnet: an omnidirectional electromagnet for controlled dipole-field generation," *IEEE Transactions on Magnetism*, vol. 50, pp. 1–10, July 2014. 1.2.3, 1.4, 2.1, 2.2.1, A
- [42] A. J. Petruska, J. B. Brink, and J. J. Abbott, "First Demonstration of a Modular and Reconfigurable Magnetic-Manipulation System," in *Robotics and Automation (ICRA), 2015 IEEE International Conference on*, (Seattle, WA), pp. 149 – 155, 2015. 1.2.3, 1.3, 6.2.2, B
- [43] P. Swain, A. Toor, F. Volke, J. Keller, J. Gerber, E. Rabinovitz, and R. I. Rothstein, "Remote magnetic manipulation of a wireless capsule endoscope in the esophagus and stomach of humans," *Gastrointestinal Endoscopy*, vol. 71, pp. 1290–3, June 2010. 1.3
- [44] A. W. Mahoney and J. J. Abbott, "Managing magnetic force applied to a magnetic device by a rotating dipole field," *Applied Physics Letters*, vol. 99, no. 13, pp. 134–103, 2011. 1.3, 1.4
- [45] S. Yim, E. Gultepe, D. Gracias, and M. Sitti, "Biopsy using a magnetic capsule endoscope carrying, releasing and retrieving untethered micro-grippers," *IEEE Transactions on Biomedical Engineering*, vol. 61, no. 2, pp. 513–521, 2014. 1.3, 5.1
- [46] A. Plotkin and E. Paperno, "3-D magnetic tracking of a single subminiature coil with a large 2-D array of uniaxial transmitters," *IEEE Transactions on Magnetism*, vol. 39, pp. 3295–3297, Sept. 2003. 2.1
- [47] C. Hu and M. Meng, "3-Axis magnetic sensor array system for tracking magnet's position and orientation," in *Intelligent Control and Automation*, vol. 2, pp. 5304–5308, 2006. 2.1
- [48] M.-H. Meng and M. Mandal, "A Linear algorithm for tracing magnet position and orientation by using three-axis magnetic sensors," *IEEE Transactions on Magnetism*, vol. 43, pp. 4096–4101, Dec. 2007. 2.1
- [49] B. Li, S. Song, M. Q.-H. Meng, W. Qiao, C. Hu, H. Ren, H. Yu, Q. Zhang, and G. Xu, "6-D localization and orientation for wireless capsule endoscope using annular magnet," *IEEE Transactions on Magnetism*, vol. 50, no. 9, 2014. 2.1
- [50] I. Aoki, A. Uchiyama, and K. Arai, "Detecting system of position and posture of capsule medical device," July 2010. 2.1

- [51] S. Hashi, S. Yabukami, H. Kanetaka, K. Ishiyama, and K. Arai, "Numerical study on the improvement of detection accuracy for a wireless motion capture system," *IEEE Transactions on Magnetics*, vol. 45, pp. 2736–2739, June 2009. 2.1
- [52] S. Hashi, S. Yabukami, H. Kanetaka, K. Ishiyama, and K. I. Arai, "Wireless magnetic position-sensing system using optimized pickup coils for higher accuracy," *IEEE Transactions on Magnetics*, vol. 47, pp. 3542–3545, Oct. 2011. 2.1
- [53] M.-G. Kim, Y.-S. Hong, and E.-J. Lim, "Position and orientation detection of capsule endoscopes in spiral motion," *International Journal of Precision Engineering and Manufacturing*, vol. 11, pp. 31–37, Apr. 2010. 2.1
- [54] K. Popek, A. Mahoney, and J. Abbott, "Localization method for a magnetic capsule endoscope propelled by a rotating magnetic dipole field," in *IEEE International Conference on Robotics and Automation (ICRA)*, pp. 5328–5333, 2013. 2.1, 2.3
- [55] C. Di Natali, M. Beccani, and P. Valdastrì, "Real-Time pose detection for magnetic medical devices," *IEEE Transactions on Magnetics*, vol. 49, pp. 3524–3527, July 2013. 2.1, 2.3
- [56] S. Yim and M. Sitti, "3-D localization method for a magnetically actuated soft capsule endoscope and its applications," *IEEE Transactions on Robotics*, vol. 29, no. 5, pp. 1139–1151, 2013. 2.1, 2.3, 5.3.2
- [57] O. Felfoul, A. T. Becker, G. Fagogenis, and P. E. Dupont, "Simultaneous steering and imaging of magnetic particles using MRI toward delivery of therapeutics," *Scientific Reports*, vol. 6, no. September, pp. 1–10, 2016. 2.1
- [58] A. J. Petruska and J. J. Abbott, "Optimal permanent-magnet geometries for dipole field approximation," *IEEE Transactions on Magnetics*, vol. 49, pp. 811–819, Feb. 2013. 2.2.2
- [59] V. Schlagerter, P. Besse, R. S. Popovic, and P. Kucera, "Tracking system with five degrees of freedom using a 2D-array of Hall sensors and a permanent magnet," *Sensors and Actuators A: Physical*, vol. 92, no. 1-3, pp. 37–42, 2001. 2.2.3
- [60] C. Hu, M. Q.-H. Meng, and M. Mandal, "Efficient magnetic localization and orientation technique for capsule endoscopy," *International Journal of Information Acquisition*, vol. 02, pp. 23–36, Mar. 2005. 2.2.3
- [61] T. L. Hedrick, "Software techniques for two- and three-dimensional kinematic measurements of biological and biomimetic systems," *Bioinspiration & biomimetics*, vol. 3, Sept. 2008. 2.3
- [62] T. D. Than, G. Alici, S. Harvey, H. Zhou, and W. Li, "Concept and simulation study of a novel localization method for robotic endoscopic capsules using multiple positron emission markers," *Medical Physics*, vol. 41, p. 072501, July 2014. 2.3
- [63] T. D. Than, G. Alici, S. Harvey, G. O'Keefe, H. Zhou, W. Li, T. Cook, and S. Alam-Fotias, "An Effective Localization Method for Robotic Endoscopic Capsules Using Multiple Positron Emission Markers," *IEEE Transactions on Robotics*, vol. 30, no. 5, pp. 1174 – 1186, 2014. 2.3
- [64] S. Trout, "Use of helmholtz coils for magnetic measurements," *IEEE Transactions on*

- Magnetics*, vol. 24, no. 4, pp. 2108–2111, 1988. 3.1, 3.5.4
- [65] D. Son, M. D. Dogan, and M. Sitti, “Magnetically actuated soft capsule endoscope for fine-needle aspiration biopsy,” *2017 IEEE International Conference on Robotics and Automation (ICRA)*, vol. v, no. 1, pp. 1132–1139, 2017. 3.1, 3.2.1
 - [66] D. Son, S. Yim, and M. Sitti, “A 5-D Localization Method for a Magnetically Manipulated Untethered Robot Using a 2-D Array of Hall-Effect Sensors,” *IEEE/ASME Transactions on Mechatronics*, vol. 21, no. 2, pp. 708–716, 2016. 3.1, 3.2.1
 - [67] H. Pang, D. Chen, M. Pan, S. Luo, Q. Zhang, J. Li, and F. Luo, “A new calibration method of three axis magnetometer with nonlinearity suppression,” *IEEE Transactions on Magnetics*, vol. 49, no. 9, pp. 5011–5015, 2013. 3.1, 3.2.3
 - [68] C. Hu, M. Meng, and M. Mandal, “The Calibration of 3-Axis Magnetic Sensor Array System for Tracking Wireless Capsule Endoscope,” *2006 IEEE/RSJ International Conference on Intelligent Robots and Systems*, pp. 162–167, Oct. 2006. 3.1
 - [69] A. Plotkin, V. Kucher, Y. Horen, and E. Paperno, “A New Calibration Procedure for Magnetic Tracking Systems,” *IEEE Transactions on Magnetics*, vol. 44, pp. 4525–4528, Nov. 2008. 3.1, 3.4.2, 3.4
 - [70] M. Li, S. Song, C. Hu, W. Yang, L. Wang, and M. Q.-H. Meng, “A new calibration method for magnetic sensor array for tracking capsule endoscope,” *2009 IEEE International Conference on Robotics and Biomimetics (ROBIO)*, pp. 1561–1566, 2009. 3.1
 - [71] A. J. Petruska, J. Edelmann, and B. J. Nelson, “Model-based calibration for magnetic manipulation,” *IEEE Transactions on Magnetics*, vol. 53, no. 7, 2017. 3.1, 3.2.4, 3.3, 3.4, 3.4.3, 3.5.1, 3.5.4
 - [72] B. Triggs, P. F. McLauchlan, R. I. Hartley, and A. W. Fitzgibbon, “Bundle adjustment - a modern synthesis,” in *International workshop on vision algorithms*, pp. 298–372, Springer, 1999. 3.1, 3.2.2, 3.2.3
 - [73] M. P. Kummer, J. J. Abbott, B. E. Kratochvil, R. Borer, A. Sengul, and B. J. Nelson, “OctoMag: An Electromagnetic System for 5-DOF Wireless Micromanipulation,” *IEEE Transactions on Robotics*, vol. 26, pp. 1006–1017, dec 2010. 3.1, 3.2.1, 3.2.4, 3.3, B
 - [74] B. E. Kratochvil, M. P. Kummer, S. Erni, R. Borer, D. R. Frutiger, S. Schürle, and B. J. Nelson, “Minimag: a hemispherical electromagnetic system for 5-dof wireless micromanipulation,” in *Experimental Robotics*, pp. 317–329, Springer, 2014. 3.2.1
 - [75] H. Strasdat, J. M. Montiel, and A. J. Davison, “Visual slam: why filter?,” *Image and Vision Computing*, vol. 30, no. 2, pp. 65–77, 2012. 3.2.2
 - [76] S. Agarwal, Y. Furukawa, N. Snavely, I. Simon, B. Curless, S. M. Seitz, and R. Szeliski, “Building rome in a day,” *Communications of the ACM*, vol. 54, no. 10, pp. 105–112, 2011. 3.2.2
 - [77] K. Hemanth, V. Talasila, and S. Rao, “Calibration of 3-axis magnetometers,” *IFAC Proceedings Volumes*, vol. 45, no. 1, pp. 175–178, 2012. 3.2.3
 - [78] P. Brauer, J. Merayo, O. Nielsen, F. Primdahl, and J. Petersen, “Transverse field effect in fluxgate sensors,” *Sensors and Actuators A: Physical*, vol. 59, no. 1-3, pp. 70–74, 1997.

3.2.3

- [79] P. Brauer, T. Risbo, J. Merayo, and O. Nielsen, “Fluxgate sensor for the vector magnetometer onboard the ‘Astrid-2’ satellite,” *Sensors and Actuators A: Physical*, vol. 81, no. 1-3, pp. 184–188, 2000. 3.2.3
- [80] A. Forsgren, P. E. Gill, and M. H. Wright, “Interior methods for nonlinear optimization,” *SIAM review*, vol. 44, no. 4, pp. 525–597, 2002. 3.2.6
- [81] D. Gebre-Egziabher, G. H. Elkaim, J. David Powell, and B. W. Parkinson, “Calibration of strapdown magnetometers in magnetic field domain,” *Journal of Aerospace Engineering*, vol. 19, no. 2, pp. 87–102, 2006. 3.5.3
- [82] T. Bergeman, G. Erez, and H. J. Metcalf, “Magnetostatic trapping fields for neutral atoms,” *Physical Review A*, vol. 35, no. 4, pp. 1535–1546, 1987. 4.1
- [83] G. Ciuti, R. Calì, D. Camboni, L. Neri, F. Bianchi, A. Arezzo, A. Koulaouzidis, S. Schostek, D. Stoyanov, C. M. Oddo, B. Magnani, A. Menciassi, M. Morino, M. O. Schurr, and P. Dario, “Frontiers of robotic endoscopic capsules: a review,” *Journal of Micro-Bio Robotics*, 2016. 5.1
- [84] J. Driller and G. Neumann, “An Electromagnetic Biopsy Device,” *IEEE Transactions on Biomedical Engineering*, vol. 14, no. 1, pp. 52–53, 1967. 5.1
- [85] K.-C. Kong, J. Cha, D. Jeon, and D.-I. D. Cho, “A rotational micro biopsy device for the capsule endoscope,” *2005 IEEE/RSJ International Conference on Intelligent Robots and Systems*, 2005. 5.1
- [86] K. Kong, S. Yim, S. Choi, and D. Jeon, “A robotic biopsy device for capsule endoscopy,” *J. Med. Devices Journal of Medical Devices*, vol. 6, no. 3, p. 031004, 2012. 5.1
- [87] C. P. Swain, “Method, System and Device for In-vivo Biopsy,” 2008. 5.1
- [88] S. Park, K.-i. Koo, S. M. Bang, J. Y. Park, S. Y. Song, and D. D. Cho, “A novel microactuator for microbiopsy in capsular endoscopes,” *Journal of Micromechanics and Microengineering*, vol. 18, no. 2, 2008. 5.1
- [89] W. Chen, G. Yan, S. He, Q. Ke, Z. Wang, H. Liu, and P. Jiang, “Wireless powered capsule endoscopy for colon diagnosis and treatment.,” *Physiological measurement*, vol. 34, no. 11, pp. 1545–61, 2013. 5.1
- [90] M. Simi, G. Gerboni, A. Menciassi, and P. Valdastrì, “Magnetic torsion spring mechanism for a wireless biopsy capsule,” *J. Med. Devices Journal of Medical Devices*, vol. 7, no. 4, p. 041009, 2013. 5.1
- [91] S. A. Zargar, M. S. Khuroo, R. Mahajan, G. M. Jan, K. Dewani, and V. Koul, “Endoscopic fine needle aspiration cytology in the diagnosis of gastro-oesophageal and colorectal malignancies,” *Gut*, vol. 32, no. 7, pp. 745–748, 1991. 5.1, 5.2.1
- [92] D. C. Allen and S. T. Irwin, “Fine needle aspiration cytology of gastric carcinoma,” *The Ulster medical journal*, vol. 66, no. 2, pp. 111–114, 1997. 5.1
- [93] H. Ito, H. Inoue, S. Ryozaawa, H. Ikeda, N. Odaka, N. Eleftheriadis, R. Maselli, N. Sando, S. Kimura, and S. E. Kudo, “Fine-needle aspiration biopsy and endoscopic ultrasound

- for pretreatment pathological diagnosis of gastric gastrointestinal stromal tumors,” *Gastroenterology Research and Practice*, vol. 2012, 2012. 5.2.1
- [94] H. A. Domanski, *Atlas of fine needle aspiration cytology*. Springer, 2013. 5.2.1
- [95] G. Kocjan, *Fine needle aspiration cytology: diagnostic principles and dilemmas*. Springer, 2006. 5.2.1
- [96] P. Vilman and A. Saftoiu, “Endoscopic ultrasound-guided fine needle aspiration biopsy: equipment and technique,” *J Gastroenterol Hepatol*, vol. 21, no. 11, pp. 1646–1655, 2006. 5.2.1
- [97] M. E. Tublin, J. a. Martin, L. J. Rollin, K. Pealer, M. Kurs-lasky, and N. P. Ohori, “Ultrasound-Guided Fine-Needle Aspiration Versus Fine-Needle Capillary Sampling Biopsy of Thyroid Nodules: Does technique Matter?,” *J Ultrasound Med*, vol. 26, no. 12, pp. 1697–1701, 2007. 5.2.1
- [98] V. Arantes, R. Logrono, S. Faruqi, I. Ahmed, I. Waxman, and M. S. Bhutani, “Endoscopic sonographically guided fine-needle aspiration yield in submucosal tumors of the gastrointestinal tract,” *J Ultrasound Med*, vol. 23, no. 9, pp. 1141–1150, 2004. 5.2.1
- [99] T. Kojima, H. Takahashi, A. Parra-Blanco, K. Kohsen, and R. Fujita, “Diagnosis of submucosal tumor of the upper GI tract by endoscopic resection,” *Gastrointestinal Endoscopy*, vol. 50, no. 4, pp. 516–522, 1999. 5.2.1
- [100] N. Ando, H. Goto, Y. Niwa, Y. Hirooka, N. Ohmiya, T. Nagasaka, and T. Hayakawa, “The diagnosis of GI stromal tumors with EUS-guided fine needle aspiration with immunohistochemical analysis,” *Gastrointestinal Endoscopy*, vol. 55, no. 1, pp. 37–43, 2002. 5.2.1
- [101] S. Miyashita, S. Guitron, K. Yoshida, S. Li, D. D. Damian, and D. Rus, “Ingestible, controllable, and degradable origami robot for patching stomach wounds,” in *Proceedings-IEEE International Conference on Robotics and Automation*, vol. 2016, pp. 909–916, Sheffield, 2016. 5.2.2
- [102] K. Hara, N. Mizuno, S. Hijioka, H. Imaoka, M. Tajika, T. Tanaka, M. Ishihara, Y. Niwa, and K. Yamao, “What is the best method for endoscopic ultrasound-guided fine needle aspiration? needle types and aspiration techniques,” *Gastrointestinal Intervention*, vol. 3, no. 2, p. 104–109, 2014. 5.3.2
- [103] K. Webb and J. H. Hwang, “Endoscopic ultrasound-fine needle aspiration versus core biopsy for the diagnosis of subepithelial tumors,” *Clinical Endoscopy Clin Endosc*, vol. 46, no. 5, p. 441, 2013. 5.3.2
- [104] G. L. Rapaccini, A. Aliotta, M. Pompili, A. Grattagliano, M. Anti, B. Merlino, and G. Gambassi, “Gastric Wall Thickness in Normal and Neoplastic Subjects: A Prospective Study Performed by Abdominal Ultrasound,” *Gastrointest Radiol*, vol. 13, no. June 1987, pp. 197–199, 1988. 5.3.2
- [105] L. I.-R., C. C.-N., L. M.-T., and L. P.-H., “Surgical treatment of gastric gastrointestinal stromal tumors: analysis of 92 operated patients,” *Digestive surgery*, vol. 25, no. 3, pp. 208–212., 2008. 5.3.2
- [106] A. M. Okamura, C. Simone, and M. D. O’Leary, “Force modeling for needle inser-

- tion into soft tissue,” *IEEE Transactions on Biomedical Engineering*, vol. 51, no. 10, pp. 1707–1716, 2004. 5.3.2, 5.3.2
- [107] Y. Tian, B. Shirinzadeh, D. Zhang, and Y. Zhong, “Three flexure hinges for compliant mechanism designs based on dimensionless graph analysis,” *Precision Engineering*, vol. 34, no. 1, pp. 92–100, 2010. 5.3.2, 5.3.2
 - [108] E. Diller, J. Zhuang, G. Zhan Lum, M. R. Edwards, and M. Sitti, “Continuously distributed magnetization profile for millimeter-scale elastomeric undulatory swimming,” *Applied Physics Letters*, vol. 104, no. 17, 2014. 5.3.2
 - [109] G. Z. Lum, Z. Ye, X. Dong, H. Marvi, O. Erin, W. Hu, and M. Sitti, “Shape-programmable magnetic soft matter,” *Proceedings of the National Academy of Sciences of the United States of America*, vol. 113, no. 41, pp. E6007–E6015, 2016. 5.3.2
 - [110] E. L. Madsen, M. A. Hobson, H. Shi, T. Varghese, and G. R. Frank, “Tissue-mimicking agar/gelatin materials for use in heterogeneous elastography phantoms,” *Physics in medicine and biology*, vol. 50, no. 23, pp. 5597–618, 2005. 5.4, 5.4
 - [111] A. Lègner, M. Diana, P. Halvax, Y. Y. Liu, S.-H. Kong, H. J. Lee, R. V. Soares, L. L. Swannstrom, and J. Marescaux, “Creation of a Realistic Biocompatible Phantom Tumor for Advanced Minimally Invasive Procedures on a Gastrointestinal Tract in Animal Model,” *Gastrointestinal Endoscopy*, vol. 81, no. 5, p. AB334, 2015. 5.4
 - [112] H.-L. Ching, M. F. Hale, and M. E. McAlindon, “Current and future role of magnetically assisted gastric capsule endoscopy in the upper gastrointestinal tract,” *Therapeutic Advances in Gastroenterology*, vol. 9, no. 3, pp. 313–321, 2016. 5.5
 - [113] S. T. Tully, *BodySLAM: localization and mapping for surgical guidance*. PhD thesis, Carnegie Mellon University, 2012. 5.5, 6.2.3
 - [114] M. Turan, Y. Almalioglu, H. Araujo, E. Konukoglu, and M. Sitti, “A Non-Rigid Map Fusion-Based RGB-Depth SLAM Method for Endoscopic Capsule Robots,” *International Journal of Intelligent Robotics and Applications*, vol. 1, no. 4, pp. 399–409, 2017. 5.5, 6.2.3
 - [115] F. Munoz, G. Alici, W. Li, and M. Sitti, “Size Optimization of a Magnetic System for Drug Delivery with Capsule Robots,” *IEEE Transactions on Magnetics*, vol. 52, no. 5, 2016. 5.5
 - [116] R. Pelrine, A. Wong-Foy, B. McCoy, D. Holeman, R. Mahoney, G. Myers, J. Herson, and T. Low, “Diamagnetically levitated robots: An approach to massively parallel robotic systems with unusual motion properties,” *Proceedings - IEEE International Conference on Robotics and Automation*, pp. 739–744, 2012. 6.2.4
 - [117] S. Floyd, E. Diller, C. Pawashe, and M. Sitti, “Control methodologies for a heterogeneous group of untethered magnetic micro-robots,” *International Journal of Robotics Research*, vol. 30, no. 13, pp. 1553–1565, 2011. 6.2.4
 - [118] E. Diller, S. Floyd, C. Pawashe, and M. Sitti, “Control of multiple heterogeneous magnetic microrobots in two dimensions on nonspecialized surfaces,” *IEEE Transactions on Robotics*, vol. 28, no. 1, pp. 172–182, 2012. 6.2.4

- [119] E. Diller, J. Giltinan, and M. Sitti, “Independent control of multiple magnetic microrobots in three dimensions,” *The International Journal of Robotics Research*, vol. 32, pp. 614–631, may 2013. 6.2.4
- [120] E. Diller, S. Miyashita, and M. Sitti, “Remotely addressable magnetic composite micropumps,” *RSC Advances*, vol. 2, no. 9, pp. 3850–3856, 2012. 6.2.4
- [121] A. Becker, O. Felfoul, and P. E. Dupont, “Simultaneously Powering and Controlling Many Actuators with a Clinical MRI Scanner,” in *Intelligent Robots and Systems (IROS 2014)*, pp. 2017–2023, 2014. 6.2.4
- [122] D. X. Chen, J. A. Brug, and R. B. Goldfarb, “Demagnetizing factors for cylinders,” *IEEE Transactions on Magnetics*, vol. 27, no. 4, pp. 3601–3619, 1991. B
- [123] J. Lenz and A. S. Edelstein, “Magnetic Sensors and Their Applications,” *IEEE Sensors*, vol. 6, no. 3, pp. 631–649, 2006. C